ABSTRACT

EVENTS RECONSTRUCTION IN 3-D POSITION SENSITIVE CdZnTe GAMMA-RAY SPECTROMETERS

by

Feng Zhang

Chair: Zhong He

The wide band gap semiconductor material CdZnTe has long been of interest for gamma-ray spectroscopy at room temperature. Despite the resolution improvement using single-polarity charge sensing techniques, the variations in detector response, such as the peripheral asymmetry in coplanar grids and the material non-uniformity can still degrade the energy resolution of large volume CdZnTe detectors.

A 3-D CdZnTe spectrometer employs a pixellated anode and a conventional planar cathode. The pixel position provides the interaction's lateral coordinates, while the interaction depths for single-pixel events are derived from the cathode to anode signal ratio. For multiple-pixel events, individual electron drift times are recorded to obtain the depth for each interaction. The 3-D position sensitivity enables corrections of non-uniform detector response down to the limit of the position resolution over the whole detector volume. This work is the first successful demonstration of 3-D position sensing for multiple-pixel events, together with single-pixel events, all done through application specific integrated circuits (ASIC). Significant improvements in energy resolutions for both single-pixel and multiple-pixel events have been achieved.

Various calibrations are carried out in order to reconstruct single-pixel and multiple-pixel events. Variations in the readout electronics must be corrected first, such

as the channel-to-channel gain variation, the baseline offset, the non-linearity, the baseline drift and the gain drift in each channel. The position-dependent charge collection due to the variations in detector response can be corrected using the 3-D position sensing. For multiple-pixel events, additional calibrations are needed, such as the correlation between the electron drift time and the interaction depth, the timing-amplitude-walk, and the weighting potential cross-talk between pixels.

Two 2.25 cm^3 volume 3-D position-sensitive CdZnTe gamma-ray spectrometers employing VAS/TAT ASIC readouts were developed. Both detectors produced excellent energy resolution. One detector achieved 0.78% FWHM and 1.24% FWHM resolution at 662 keV for single-pixel events and two-pixel events, respectively. Possible reasons for energy resolution degradation of multiple-pixel events are discussed. Spectroscopy for multiple gamma-ray energies and high-energy (> 2 MeV) source is demonstrated. The electron mobility-lifetime products of both detectors were measured and compared. Possible factors affecting the detector response are also analyzed.

EVENTS RECONSTRUCTION IN 3-D POSITION SENSITIVE CdZnTe GAMMA RAY SPECTROMETERS

by

Feng Zhang

A dissertation submitted in partial fulfillment
of the requirements for the degree of
Doctor of Philosophy
(Nuclear Engineering and Radiological Sciences)
in The University of Michigan
2005

Doctoral Committee:

        Associate Professor Zhong He, Chairperson
        Professor Glenn F. Knoll
        Associate Professor David K. Wehe
        Associate Professor Thomas H. Zurbuchen

ACKNOWLEDGMENTS

First and foremost I would like to thank my advisor, Professor Zhong He, for his inspiring and encouraging guidance and support. The conversations with him helped me greatly. Because of the confidence he has shown in my ability, my past four years have been a time of growth and challenge.

I would also like to express my thanks to other committee members (Professor Glenn Knoll, Professor David Wehe and Professor Thomas Zurbuchen) for their support and guidance during my work related to this dissertation.

I would like to acknowledge the help from Mr. James Berry. In addition, I am grateful to a number of graduated and fellow students for their encourage and assistance to this work, including Dr. Wen Li, Dr. Yanfeng Du, Dr. Clair Sullivan, Dr. James Baciak, Dr. Carolyn Lehner, Dan Xu, Ben Sturm and Scott Kiff. I would like to express my sincere gratitude and appreciation to all department staff and especially Ms. Pat Moore for their assistance related to this work.

Finally, I would like to extend my greatest appreciation to my parents and my wife, for their understanding and support, which made this dissertation possible.

TABLE OF CONTENTS

LIST OF FIGURES

x

xii

LIST OF TABLES

CHAPTER 1

INTRODUCTION

For gamma ray detection, an ideal detector material would have high Z for high stopping power, would be in a solid-state form for high stopping power, would have a wide band gap for room temperature applications and have good energy resolution. Scintillators, such as NaI(Tl), have high Z and high density and have been used for decades as gamma ray detectors operating at room temperature. However, the energy resolution is poor, generally ~7% FWHM at 662 keV. Semiconductor detectors, such as Germanium and Silicon can have very good energy resolution. High purity germanium detectors have excellent energy resolution and the volume of the detector can be as large as 800 cm^3 [1]. However, the band gap of germanium is only 0.7 eV and the leakage current is too high for room temperature applications. For it to be operated in a manner to achieve good resolution, it has to be cooled with liquid nitrogen, reducing its advantages in many applications. Silicon detectors can be operated at room temperature, but the Z value of silicon is only 14 and the commercially available silicon detectors are at most a few millimeters thick, limiting their application only for x-ray and charged particle detection.

1.1 Development of Room Temperature Semiconductor Detectors

The first semiconductor detector was introduced in 1945 when a AgCl crystal was used to detect alpha particles and gamma rays [2]. However, there had been skepticism for a long time because of the polarization and charge carrier trapping problems in

semiconductor materials. With the great advances in semiconductor crystal growth and processing technology, high purity germanium and silicon with reasonable volume and good charge carrier transport properties have been produced and achieved great successes as radiation detectors [3]. Despite the significant issues such as charge carrier trapping, space charge accumulation and polarization, the unique material properties of several compound semiconductor materials make them attractive in radiation detection applications when Ge and Si are deemed unsuitable. Room temperature operation, for instance, requires the semiconductors to have wide band gap to reduce the thermally generated leakage current. For gamma ray spectroscopy, photoelectric interactions are preferable. Therefore, compound semiconductors for efficient gamma ray spectroscopy should be composed of high Z materials. Furthermore, high detection efficiency demands that high quality crystals be available in large volume. Room temperature operational semiconductors generally have band gap energies between 1.35 and 2.55 eV. Presently, Mercuric iodide (HgI_2), cadmium telluride (CdTe), and cadmium zinc telluride ($Cd_{1-x}Zn_xTe$) are the only commercially available wide band gap semiconductors and have received extensive exploration.

HgI_2 has been investigated as a room temperature x-ray and gamma ray detector since the early 1970s [4-7]. HgI_2 has high stopping power due to atomic numbers of 80 and 53 and a density of $6.4g/cm^3$. The large bandgap energy (2.13 eV [8]) of HgI_2 permits operation at room temperature while producing only very small thermally generated leakage current. However, the poor charge mobility-lifetime products of $\sim10^{-5}$ cm^2/V for holes and $\sim10^{-4}$ cm^2/V for electrons limit its application to thin detectors. Therefore, the efficiency of early detectors was relatively low because the detectors were too thin. Additionally, the buildup of trapped charges can cause a polarization effect, in

which the electric field is distorted and the efficient charge collection is further disturbed [9].

CdTe grown by the traveling heater method (THM) has been regarded as a promising room temperature semiconductor gamma ray detector since the mid-1960s [10-13]. It has a bandgap energy of 1.52 eV [8] and hence a high resistivity (10^8-10^9 Ω·cm) allowing room temperature operation. It has atomic numbers of 48 and 52 with a density of 6.06 g/cm^3, suitable for gamma ray detection. However, the poor hole mobility-lifetime product (~5×10^{-5} cm^2/V) results in low collection efficiency of holes and hence a degraded energy resolution for large devices due to a position-dependent charge collection. Similar to HgI$_2$, CdTe also has a polarization phenomenon, which under certain conditions of operation leads to a time-dependent decrease in the counting rate and charge collection efficiency [14, 15].

In the 1990s, the emergence of Cd$_{1-x}$Zn$_x$Te, where x is the blending fraction of ZnTe in CdTe, has dramatically changed the situation of high-resolution room-temperature semiconductor detectors [16, 17]. The inclusion of Zn elements in the CdTe increases the bandgap energy to the range of 1.53-1.64 eV [8], resulting in higher resisitivity (~10^{11} Ω·cm) [18] than CdTe. Large CdZnTe single crystals have been grown [17, 19] by using the high pressure Bridgman method (HPB). The electron mobility-lifetime product is ~10^{-3} cm^2/V while the hole mobility-lifetime product is ~3×10^{-5} cm^2/V. Although charge trapping is still a problem for thick detectors, the polarization effect is no longer observed in CdZnTe, which gives CdZnTe a great advantage over HgI$_2$ and CdTe.

Severe hole trapping problems have long hindered the application of room-temperature semiconductor detectors. By applying a high bias across a thin (a few millimeters) detector so that holes can be efficiently collected, good energy resolution

3

can be achieved for x-rays and low energy gamma rays. In order to achieve good detection efficiency at higher gamma ray energies, thicker detectors are desired. However, for thick room-temperature semiconductor detectors with conventional planar electrodes, the energy resolution is significantly degraded due to severe hole trapping. Efforts have been devoted to address this problem through pulse processing techniques for HgI_2 and CdTe [20-23]. In this approach, the pulses with a slow rise time are corrected or discriminated by means of specially designed electronics. Despite some improvement in energy resolution for thick detectors, this method can lead to significant loss of detection efficiency, because it cannot solve the fundamental problem of charge trapping which causes degradation in signal-to-noise ratio.

Another approach, called single polarity charge sensing, employs special detector and electrode structures such that the induced charge is only sensitive to the drift of electrons rather than holes. This configuration is similar to the Frisch grid, invented sixty years ago for gas detectors [24]. The first attempt of single polarity charge sensing in large volume CdZnTe detectors was proposed by P.N. Luke in 1994 [25, 26]. This method, called coplanar grid, employs an anode consisting of a pair of interleaved parallel strip electrodes on a surface of the detector. A different bias is applied to each set of electrodes. This potential difference is small compared to the overall potential across the detector. The electrode with higher potential serves as the collecting electrode for electrons, the other electrode forms the non-collecting electrode. When electrons and holes move within the bulk material of the detector, they induce equal signals on both grid electrodes. When the electrons come close to the anode plane and drift toward the electrode with higher potential, the signal of the collecting electrode rises steeply. A net signal, which is obtained by subtracting the signals from the two electrodes, is sensitive primarily to the electrons arriving at the anode and is independent of the motion of holes

for most of the interaction depths. Since the depth dependent signal due to the movement of holes is subtracted, the energy resolution degradation due to severe hole trapping is avoided.

It has long been recognized that reducing the size of the electrode used to collect the higher $\mu\tau$ carriers can potentially eliminate the low-energy tail by effectively achieving single polarity charge collection through the "near-field effect". In 1995, H.H. Barret et al. showed that if the pixel size is small in comparison with the detector thickness and the pixel electrode is biased to collect electrons, the incomplete charge collection due to severe hole trapping can be dramatically improved, because the induced charge on each pixel anode is dominated by the number of electrons collected by the anode [27]. This "small pixel effect" has been applied to large volume CdZnTe detectors and showed significant improvement in energy resolution despite poor collection of holes [28-30]. Several other single polarity charge sensing techniques have been proposed, such as hemispherical detectors [31], parallel strip Frisch grid detectors [32-34], the design of a small area anode surrounded by a "control electrode" [35] and capacitive Frisch grid detectors [36]. Despite the significant improvement in spectroscopic performance over conventional planar detectors, these designs are inherently limited by the nonuniform electric field and charge induction efficiency over the entire detector volume when compared with coplanar grid and pixellated anode detectors [37].

Although single polarity charge sensing techniques have solved the severe hole trapping problem in wide bandgap semiconductor detectors, the loss of electrons can still broaden the photopeak due to different electron drift lengths when gamma rays interact inside the detector at random depths. Several methods have been introduced to compensate the signal loss due to electron trapping at different interaction depths. For coplanar grid CdZnTe detectors, P.N. Luke used a relative gain method [25], in which an

adjustable gain is applied to each of the collecting and non-collecting anode signals before the subtraction. At a proper relative gain, the depth-dependent signal loss due to electron trapping is compensated and the subtraction signal is independent of the interaction depth. Another approach utilizing the depth dependence of the weighting potential in a beneficial way was proposed, in which the electron trapping can be compensated by properly choosing the size of the electrodes and the bias voltage applied on the cathode [38]. However, there is only one fixed bias voltage under which the electron trapping is optimally compensated by the weighting potential. Therefore, this technique is not as flexible as a general coplanar grid detector in achieving the best spectroscopic performance. Another more general approach is to determine the interaction depth from the signal ratio of the conventional planar cathode and the single carrier sensing anode for each event and use the depth information to correct the signal loss due to electron trapping [39]. This method has been successfully employed in both large volume coplanar grid and pixellated CdZnTe detectors and greatly improved the energy resolution to better than 2% FWHM at 662 keV [40, 41].

1.2 Challenges from Other Gamma-Ray Spectrometers

With the help of single polarity charge sensing techniques and methods to compensate electron trapping, the energy resolutions of large volume CdZnTe gamma ray spectrometers have been significantly improved. However, several factors are hindering the development and application of large volume CdZnTe detectors. First, the size of commercially available CdZnTe single crystals is limited to a few cubic centimeters, limiting the detection efficiency for gamma rays, and single crystals with this size normally cost more than $2,000/cm^3. Employing an array of many small volume detectors can achieve high active volume, but also with increased system complexity.

6

Second, even if larger single crystals were available, it would be challenging to implement the coplanar grid design on a large anode surface without significantly increasing the electronic noise due to the increased capacitance between the two coplanar grid electrodes. Third, due to material non-uniformity, charge induction non-uniformity from the electrode design, and the added noise caused by surface leakage current and increased capacitance of coplanar grids, the energy resolution for 1-2 cm^3 volume coplanar grid CdZnTe detectors has been limited to ~2-3% FWHM at 662 keV for several years. While there is still a long way to go for CdZnTe to challenge the role of Ge in gamma ray detection, other competitors from conventional scintillation detectors and gas detectors are starting to challenge coplanar-grid CdZnTe detectors in terms of cost and even performance.

On one hand, in recent years, several scintillators have been discovered to exhibit extremely promising properties, including $LaBr_3$:Ce [42, 43], $LaCl_3$:Ce [44] and $RbGd_2Br_7$:Ce [45]. Although having relatively low density and atomic number, these materials have not only high light yield and good proportionality for excellent energy resolution, and also fast decay time for good timing resolution and high counting rates. Of these, $LaBr_3$:Ce is considered the most promising material. It has a light output of 61,000 photons/MeV and has achieved an energy resolution of 2.9% FWHM for 662 keV gamma rays [42, 46, 47], which is a great improvement comparing to NaI:Tl which typically achieves 6% FWHM at 662 keV. This resolution is already comparable to coplanar grid CdZnTe detectors with comparable volume (~0.5 cm^3). On the other hand, high pressure Xenon detectors with Frisch grid [48] and pulse rise time compensation [49] have achieved an energy resolution of 2.2% FWHM at 662 keV. These detectors can be cost-effectively produced with very large sensitive volumes, and can be operated at room temperature with simple electronics, yet with comparable performance as CdZnTe.

They can be strong competitors for CdZnTe. Therefore, it is urgent to improve the energy resolution of CdZnTe with a goal of better than 1% FWHM at 662 keV.

1.3 Three-Dimensional Position Sensitive CdZnTe Spectrometers

With the high demands in nuclear non-proliferation, home land security and space sciences, wide band gap semiconductor materials, such as CdTe, CdZnTe and HgI_2, have gained more and more interest for the convenience of room temperature operation, high efficiency for gamma-ray detection and potential for good energy resolution. Among them, CdZnTe has gained particular interest. Single polarity charge sensing techniques, such as coplanar grids or pixellated anodes, had overcome the severe hole trapping problem and greatly improved the energy resolution of large volume CdZnTe detectors. However, even with single polarity charge sensing techniques and methods to compensate for electron trapping, such as relative gain and depth sensing, the variations in electron trapping and material non-uniformity can still degrade the energy resolution.

Following the introduction of the depth sensing technique in coplanar detectors, we developed 3-D position sensitive CdZnTe spectrometers. The goal of a 3-D CdZnTe spectrometer is to detect gamma rays ranging from a few tens of keV up to 1-2 MeV. The system should be able to record individual interactions with both good energy resolution (~6 keV) and good 3-D position resolution (~1 mm). The ability to identify and record multiple interactions can greatly increase the sensitivity of the system. 3-D position sensitive CdZnTe spectrometers can have wide application in nuclear nonproliferation, homeland security, medical imaging and space sciences.

A 3-D CdZnTe spectrometer employs a pixellated anode and a conventional planar cathode. The pixel location provides the 2-D interaction coordinates, while the interaction depths for single-pixel events are derived from the cathode to anode signal

ratio. For multiple-pixel events, individual electron drift times are recorded to obtain the depth for each interaction [50-52].

3-D CdZnTe spectrometers have several unique advantages. Due to the small size of each anode pixel and the small pixel effect, the severe hole trapping problems is overcome resulting in good energy resolution. The 3-D position sensitivity enables corrections of the material non-uniformity and the variations in electron trapping and weighting potential down to the limit of the position resolution over the whole detector volume [53]. Furthermore, the leakage current and the detector capacitance are shared among all pixels, resulting in minimum electronic noise in each pixel. Since the energy and 3-D coordinates of each interaction can be obtained, interactions can be reconstructed and discriminated event by event to increase the system sensitivity by greatly suppressing the background [54], and at the same time Compton imaging can be accomplished [55-58].

The challenge in 3-D CZT spectrometers is to read out a large number of independent channels. Only application specific integrated circuitry (ASIC) can attain this goal. Other 3-D position sensing techniques aimed to reduce the number of readout channels have been proposed, such as the orthogonal coplanar anode strip detector [59-61] and the 3-D position-sensitive coplanar grid detector [62]. However, these devices depend on transient signals on the non-collecting electrodes for position sensing, which have intrinsically poorer signal-to-noise ratio than that of the collecting electrode signals. For multiple-interactions events, it will be even more challenging to identify individual interaction position and energy from the total signal from the collecting anode. Furthermore, higher leakage current in each collecting electrode makes the intrinsic electronic noise higher than that of a pixellated anode.

1.4 Previous Work on 3-D CdZnTe Spectrometers

Wen Li focused his Ph.D work on the 1st-generation and the 2nd-generation 3-D CdZnTe detectors [52]. In 1998, the first fully functional 3-D CdZnTe spectrometer was developed [63]. The 3-D position sensitivity of this CZT spectrometer using VA1 ASIC chips enabled the correction for material non-uniformity and varying electron trapping in three dimensions. An energy resolution of 1.7% FWHM at 662 keV was achieved for single-pixel events from the whole bulk of a 1 cm^3 3-D CZT detector. However, the 1st-generation 3-D CdZnTe spectrometers could only obtain the energy and 3-D position information for single-pixel events.

The 2nd-generation 3-D CdZnTe systems were then developed aiming for the ability to reconstruct multiple-pixel events. It was partially successful before Wen Li graduated in July 2001. The ability of depth sensing for multiple-pixel events using electron drift time was successfully demonstrated. However, the special channels used to read out the cathode signal did not work properly. Instead, Li used external discrete circuits and NIM modules to read out the cathode signal. Furthermore, half pixels of the detector did not have a signal. The energy resolution was only 6.8% FWHM at 662 keV for two-pixel events, significantly worse than that of single-pixel events (1.5% FWHM at 662 keV).

1.5 Tasks Accomplished during This Thesis Study

This study has three major goals. The first goal is to achieve 3-D position sensing for multiple-pixel events using only the ASIC readout system. The second goal is to develop the 3rd-generation electronic readout system to reduce the electronic noise to around 3 keV FWHM, which is about a factor of two smaller than that of the 2nd-generation system, aiming to achieve better energy resolution and lower thresholds. The

third goal is to establish and optimize the calibration and event reconstruction procedures, to investigate the factors limiting the energy resolution and to improve the energy resolution for single-pixel events and multiple-pixel events.

Chapter 2 presents the theoretical background employed in the development of the 3-D position sensitive CdZnTe detectors. First, the Shockley-Ramo theorem is introduced as the basis for detectors utilizing charge induction as a means of signal generation. Second, the severe hole trapping problem is discussed and the single polarity charge sensing methods which can overcome the hole trapping problem are introduced. Third, the methods of compensating electron trapping are discussed and the depth sensing techniques using the C/A ratio and the electron drift time are presented. Fourth, two methods of estimating the electron mobility-lifetime product in 3-D CdZnTe detectors are discussed. The final part of Chapter 2 introduces the correlation matrix method of detecting common mode noise among channels.

Chapter 3 presents the three different aspects of the modeling of 3-D CdZnTe detectors. The first part is an introduction to the Monte Carlo simulations performed using Geant4 [64]. The objective of the simulation is to understand how the finite electron cloud size and the diffusion during drifting affect the fraction of multiple-pixel events, its potential effect on the reconstruction and the effects of triggering thresholds. The simulation results show that the finite electron cloud size and the diffusion is a strong factor in the collected signal and may be an important source of performance degradation for multiple-pixel events, and low triggering thresholds are required to properly identify the multiple-pixel events. The second part of Chapter 3 covers the simulation results for the weighting potential using Maxwell [65]. The weighting potential of an anode pixel and the cathode are shown, and the weighting potential cross-talk is also simulated and discussed. The third part of Chapter 3 presents the modeling results for timing-amplitude-

walk and timing resolution of the anode signal and the cathode signal using the Simulink toolbox of Matlab [66]. It is shown that the timing-amplitude-walk is an important factor that needs to be corrected in electron drift time depth sensing for multiple-pixel events. Furthermore, the timing resolution is worse at lower energy and is worse for the cathode signal whose pulse rising time is much slower than that of the anode signal, which may be the limitations in the energy resolution for multiple-pixel events.

Chapter 4 describes the development of three iterations of the readout electronics for the two generations of 3-D CdZnTe systems. Each 3-D CdZnTe detector has a conventional planar cathode and an 11×11 pixel-grid anode pattern glued and connected to a ceramic substrate using plate-through-via. The VAS2/TAT2 ASIC is introduced in detail for a better understanding of the working principle of the readout electronics. The problems in the VAS2/TAT2 implementation are discussed. The improvements and new problems in the VAS3/TAT3 are then introduced. Finally, the development of the VAS3.1/TAT3 is presented. The software developed for data acquisition and data processing are introduced at the end of Chapter 4.

Chapter 5 focuses on the calibration and event reconstruction procedures developed for the 3-D CdZnTe detectors. First, the calibrations for single-pixel events are discussed. Second, additional calibrations necessary for multiple-pixel events are discussed. Due to the improvements in the new readout electronics and some new problems as well, some calibrations are needed in the VAS2/TAT2 systems while others are needed in the VAS3.1/TAT3 systems. Flow charts summarizing all calibration and events reconstruction procedures are presented at the end of this chapter.

Chapter 6 presents the experimental results from the VAS2/TAT2 systems and the VAS3.1/TAT3 systems. The energy resolution for single-pixel events and multiple-pixel events are reported. The electronic noise is estimated and compared. The spectra for

multiple gamma ray sources and a sample of uranium ore are presented. Possible factors degrading the energy resolution for multiple-pixel events are discussed. Finally, the electron mobility-lifetime products are measured and compared for two detectors.

Chapter 7 introduces the factors affecting the detector response. Several typical cases of electron trapping, variation in ionization energy, possible defects, and non-uniform weighting potential, along with their effects on detector response, such as the C/A ratio, the photopeak centroids, and the photopeak counts are discussed.

Chapter 8 summarizes the major results of this dissertation work. It also includes recommendations for future work.

CHAPTER 2

THEORY

When a gamma ray interacts inside a semiconductor detector, a large number of electron hole pairs proportional to the deposited energy are created. The electrons and holes drift towards the anode and the cathode, respectively, under the applied electric field. In order to calculate induced charge on electrodes due to the motion of the electron-hole pairs, the Shockley-Ramo theorem [67, 68] and the concepts of the weighting field and weighting potential need to be introduced first. Single-polarity charge sensing electrode designs, which are only sensitive to electron motion, are used in room-temperature semiconductor detectors to overcome the severe hole trapping problem. However, electron trapping is still a problem degrading the energy resolution. Several techniques aiming to reduce the impact of the electron trapping on the energy resolution are briefly discussed. Methods of measuring the electron mobility-lifetime products are presented. Finally, the correlation matrix method of detecting common mode noise among channels is discussed.

2.1 The Shockley-Ramo Theorem

Prior to the Shockley-Ramo theorem, in order to calculate the induced charge on an electrode by a moving charge, people had to first solve the Poisson equation:

$$\nabla^2 \varphi = \frac{\rho}{\varepsilon} \tag{2.1}$$

where φ is the electric potential, ρ is the space charge density, and ε is the dielectric constant of the detector medium, to get the electric potential. The equation:

$$\vec{E} = -\nabla \varphi \tag{2.2}$$

was then used to get the instantaneous electric field $\vec{E}$ at each point along the track of the moving charge. The induced charge Q was calculated by integrating the normal component of $\vec{E}$ over the electrode surface S :

$$Q = \oiint_S \varepsilon \vec{E} \cdot d\vec{S} \tag{2.3}$$

This approach demands a heavy calculation load to get enough precision, since the calculations need to be repeated for each different point along the moving charge trajectory. In the late 1930s, Shockley [68] and Ramo [67] independently introduced a simple method to calculate the induced charge on any electrode when there is no space charge in the medium.

The Shockley-Ramo theorem states: the instantaneous charge Q and current i on a given electrode induced by a moving point charge q are given by:

$$Q = -q\varphi_0 \tag{2.4}$$

$$i = q\vec{v} \cdot \vec{E}_0 \tag{2.5}$$

where $\vec{v}$ is the velocity of charge q. φ_0 and $\vec{E}_0$ are the weighting potential and the weighting field at charge q's instantaneous position, respectively. φ_0 has no unit and $\vec{E}_0$ has a unit of $\dfrac{1}{meter}$. They can be calculated by solving the Laplace equation

$$\nabla^2 \varphi = 0 \tag{2.6}$$

for the geometry of the detector with some artificial boundary conditions:

1. The electrode for which the induced charge is to be calculated is set at unit potential.

2. All other electrodes are set at zero potential.

3. All space charges are ignored.

Since the weighting potential is determined by only the geometry of electrodes and is independent of the actual bias applied on the electrodes, only one calculation is needed. Although the drifting path of the moving charge q is still determined by the actual operating electric field inside the medium, the induced charge Q can be easily calculated using Equation 2.4.

The Shockley-Ramo theorem was originally introduced for vacuum tubes where there was no space charge. Later, the generalization of the Shockley-Ramo theorem to cases with stationary space charge [69, 70] led to wider application of the theorem in predicting output signals from many types of charge sensing devices. The induced charge on any electrode produced by q depends only on the location of the moving charge and the configuration of the device, and is independent of the actual bias voltages and space charge distribution.

2.2 Hole Trapping and Single-Polarity Charge Sensing

The hardest problem hindering the application of room temperature semiconductor detectors is the severe hole trapping. For CdZnTe, the mobility-lifetime product of holes is two orders of magnitude lower than that of electrons. Applying a very high potential across a thin (1-2 mm) detector can help collect holes. However, thick detectors are desired for high detection efficiency for high energy gamma rays, especially when single crystals up to 1 cm thick are commercially available today. The effect of severe hole trapping was reduced to a large extent in the early 1990s by the implementation of coplanar grid electrodes in large volume CdZnTe detectors [26] and the discovery of the small pixel effect [27] in pixellated detectors. Both techniques are basically only sensitive to electron motion inside the detector, and thus are referred to as single-polarity charge sensing.

2.2.1 Coplanar grid detector

The underlying idea in the coplanar grid electrode design is not new and can be traced back to the Frisch grid design [24] in gas chambers developed half a century ago. A typical coplanar grid detector is shown in Figure 2.1(a)-(b). It consists of two symmetric interleaving strip electrodes - one collecting anode and one non-collecting anode. Because of this symmetry, when electrons are far away from the anode the induced charges on both electrodes are the same. Only when the electrons drift in a distance comparable to the strip pitch will they "see" the asymmetry in these two electrodes and induce different amount of signals on the two electrodes. By applying a lower bias on the non-collecting electrode, the electrons will drift towards, and be collected by, the collecting electrode. Figure 2.1(c) shows the weighting potential of the two electrodes. By subtracting the weighting potential of the non-collecting electrode from that of the collecting electrode, we get a net weighting potential that remains zero for most of the detector thickness and rises rapidly to one in one pitch region near the anode. Thus, for interactions occurring in most of the detector thickness, the subtracted signal from the two electrodes is only proportional to the amount of electrons created by the energy deposition. Therefore, the subtraction of the two coplanar grid electrodes cancels the contribution from the motion of holes and works just like the Frisch grid in a gas chamber that shields the anode from sensing the motion of the ions.

This simple single-polarity charge sensing technique greatly improved the energy resolution of thick CdZnTe detectors.

2.2.2 Pixellated detector

Another approach to single polarity charge sensing is by employing a large number of small pixels on the anode. When electrons are far away from the anode

surface, the induced charges are shared by many pixels and thus each pixel only has a small signal. When the electrons drift towards the anode, fewer and fewer pixels share larger and larger percentages of the total induced charge. The signals on these pixels gradually rise and the signals on the other pixels gradually fall, until the electrons finally arrive at and are collected by one pixel will the signal on this collecting pixel reaches the maximum and the signals on the other pixels fall to the minimum. This can be well understood from the weighting potential of one pixel shown in Figure 2.2(b).
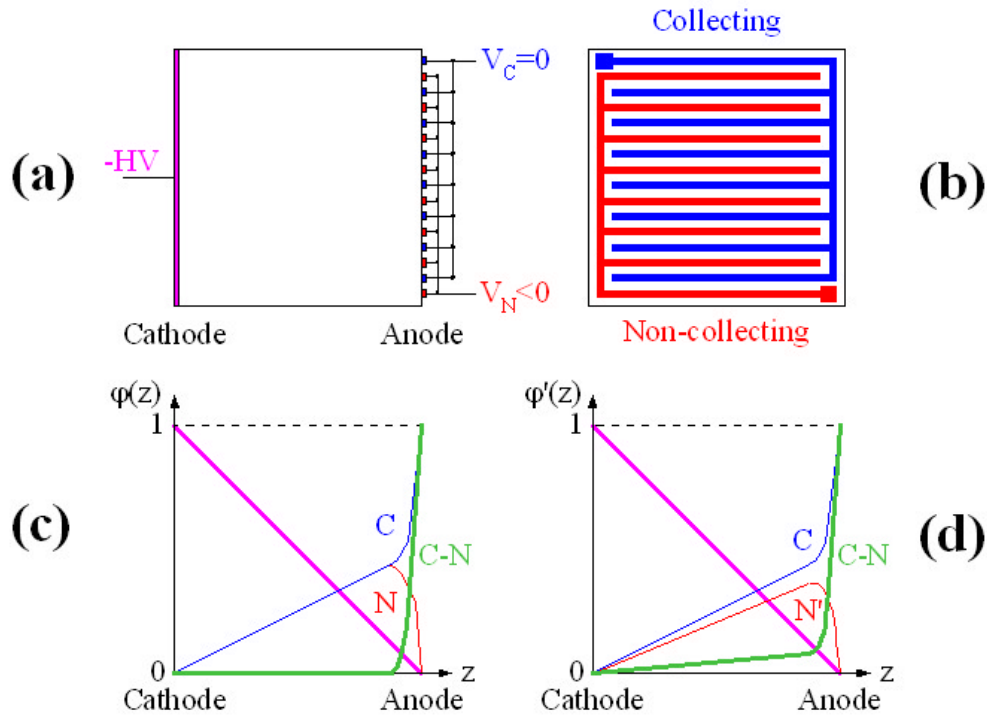
Figure 2.1. Illustration of a coplanar grid detector. (a). Cross-sectional view and bias conditions. (b). Coplanar grid anode pattern. (c). Weighting potential of both anode electrodes and the cathode, illustrating the depth dependence of the cathode signal and the depth independence of the subtraction anode signal. (d). Depth dependence of the subtraction anode signal caused by non-equal gain.

Besides single polarity charge sensing, a pixellated detector has additional advantage that the leakage current and the detector capacitance are shared by all pixels. Therefore, the electronic noise should be greatly reduced for each pixel. Furthermore, the 2-D position of the pixel can provide 2-D coordinates of the interactions.
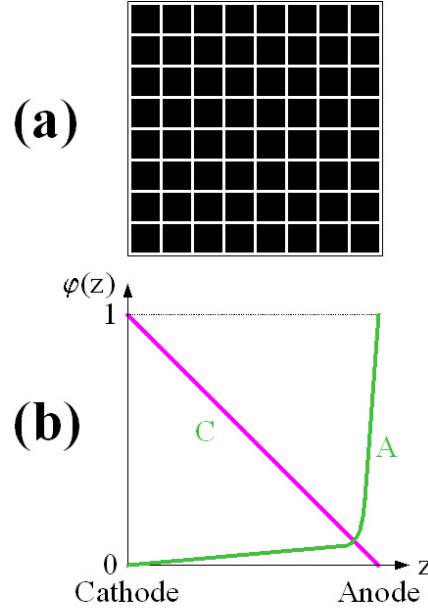
Figure 2.2. Illustration of a pixellated detector. (a). Pixellated anode pattern. (b). Weighting potential of one anode pixel and the cathode, illustrating the linear depth dependence of the cathode signal and the weak depth dependence of the anode pixel signal.

2.3 Electron Trapping and Methods to Compensate Electron Trapping

Although the poor detector performance due to severe hole trapping has been greatly improved by employing single polarity charge sensing, the electron trapping in room temperature semiconductor detectors can still degrade the energy resolution.

Several techniques aiming to mitigate the impact of electron trapping on the energy resolution have been developed.

2.3.1 Coplanar grid and relative gain method

Although coplanar grid CdZnTe detectors are no longer vulnerable to hole trapping problem, the subtraction signal of the two electrodes is still dependent on the interaction depth because the longer the distance that electrons travel the fewer electrons can be collected by the collecting electrode due to electron trapping. This depth dependence due to electron trapping will broaden the photopeak if not corrected. Along with the implementation of the coplanar grid anode design, Luke [25] used a relative gain method for electron trapping compensation. By applying non-equal gains to the signals on the two electrodes, the subtracted weighting potential of the two electrodes can be artificially made depth-dependent with a trend compensating the electron trapping, as illustrated in Figure 2.1 (d). This way, the subtraction signal can be made independent of the interaction depth.

2.3.2 Pixellated detector and weighting potential compensation method

For pixellated detectors, the induced signal on the pixel has two different depth dependences. On one hand, the weighting potential of the pixel is depth dependent and results in larger signal from interactions near the cathode side due to larger weighting potential difference, which can be approximated as:

$$Q_w(z) \cong 1 - az \tag{2.7}$$

On the other hand, just as in the discussion in the coplanar grid detectors, the electrons collected by the pixel will be fewer if the interactions occur further away from the anode surface due to electron trapping:

20

$$Q_e(z) = e^{-b(1-z)} \cong 1 - b(1-z) \qquad (2.8)$$

However, the amount of electron trapping can be changed in a certain range by adjusting the operating potential applied on the detector. Therefore, by properly choosing the pixel pitch and the operating potential, the electron trapping effect can be roughly compensated by the weighting potential, which results in an induced signal on the pixel independent of the interaction depth (with $a = b$):

$$Q(z) = Q_w(z) \cdot Q_e(z) \cong (1 - az) \cdot (1 - b(1-z)) \cong 1 - b - (a-b)z \qquad (2.9)$$
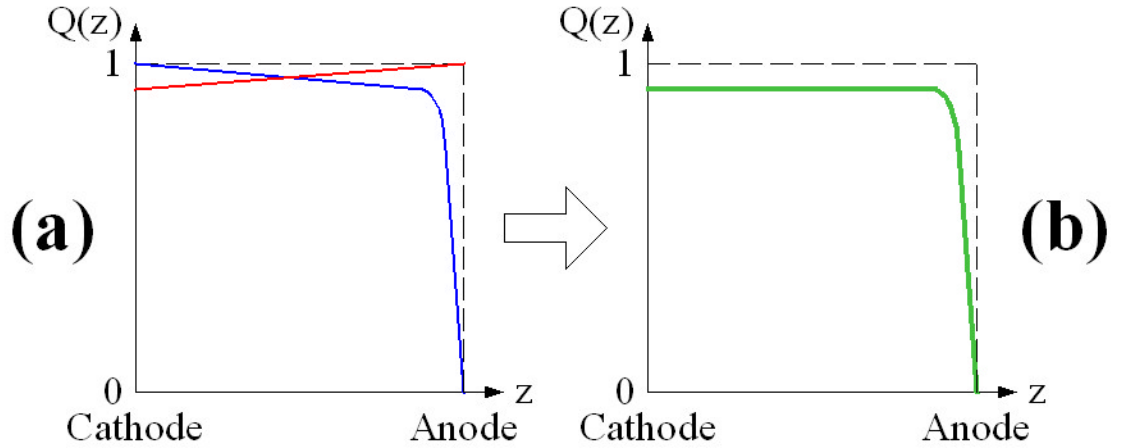
Figure 2.3. Illustration of the weighting potential compensation for the electron trapping in a pixellated detector. (a). Depth dependence due to weighting potential (blue) and electron trapping (red). (b). The compensated signal is independent of the interaction depth over most of the detector thickness.

Although this compensation method has the advantage of simplicity in data processing, the disadvantages are also obvious. The detector material needs to be very uniform in the lateral direction, otherwise the material properties variation under each pixel will make it difficult to find a proper pixel configuration for best compensation effect. Prior to the electrode fabrication, the electron mobility-lifetime product has to be

estimated because the pixel size and the proper operating potential need to be estimated accordingly. This will be an obstacle for mass production. That there is only one optimum operating potential also reduces the flexibility of such a device.

2.3.3 Depth sensing methods

Since the electron trapping is a monotonic function of the interaction depth, if the interaction depth can be derived from the signals available from the detector, the photopeak centroid as a function of the interaction depth can then be calibrated and used to correct for electron trapping.

2.3.3.1 C/A ratio

He et al. [39] proposed a method of using the ratio of the cathode signal to the anode signal to obtain the interaction depth for coplanar grid detectors. As already shown in Figure 2.1(c), the weighting potential of the cathode has a linear relation with the interaction depth, while the weighting potential of the subtraction signal of the two anodes is independent of the interaction depth for most of the detector thickness. Therefore, these two signals can be approximately expressed as

$$S_c = ne(1-z) \tag{2.10}$$

$$S_a = ne \tag{2.11}$$

where n is the number of electrons created by the energy deposition and $(1-z)$ is the interaction depth. The interaction depth can be derived from the ratio of the above two signals as

$$R = \frac{S_a}{S_c} = 1 - z \tag{2.12}$$

Then, by conceptually dividing the whole detector thickness into several tens of depth bins and sorting all events into subspectra of different interaction depths, the photopeak centroid of each subspectrum is measured and a gain factor can be derived and applied to

align the photopeaks of all subspectra to the same position to form a much narrower photopeak than the uncorrected one. Besides good energy resolution, position sensitive capability is added to the device.

The C/A ratio depth sensing can also be used in a pixellated detector for single-interaction events, since the cathode signal is linear with the interaction depth and the anode signal is only slightly depth dependent. Some systematic shift may be present in the relation between the C/A ratio and the true interaction depth [71]. However, the C/A ratio information is already enough to do depth correction for the depth dependency of the anode signal, due to both weighting potential and electron trapping. The depth resolution from C/A ratio can be derived from Equation 2.12 as

$$FWHM_{dR} = \sqrt{\left(\frac{FWHM_c}{S_c}\right)^2 + \left(\frac{FWHM_a}{S_a}\right)^2} \times \frac{S_c}{S_a} \qquad (2.13)$$

where S_c and S_a are the cathode and anode pixel signals, and $FWHM_c$ and $FWHM_a$ are the fluctuations in the cathode and anode pixel signals.

For multiple-interaction events in pixellated detectors, the C/A ratio can no longer be used to get the individual interaction depth, since the cathode signal is now a sum of the two interactions. It can only provide the energy weighted centroid depth of the multiple interactions.

2.3.3.2 Electron drift time

A more complicated but unavoidable way to do depth sensing for multiple-interaction events in pixellated detectors is electron drift time sensing. Because of the weighting potential, the cathode will be triggered shortly after the electrons created by the energy depositions start to move, while the pixel will be triggered when the electrons drift to its vicinity. The electrons normally drift at a constant velocity under a fixed electric field. Therefore, the individual electron drift time and consequently the

interaction depth can be derived by measuring the time difference between the cathode trigger and each anode pixel trigger.

Because the electron drift time is determined by the time difference between the cathode trigger and the anode trigger, the depth resolution derived from the electron drift time can be expressed as:

$$FWHM_{dT} = \frac{\sqrt{FWHM_{cT}^2 + FWHM_{aT}^2}}{T} \times D \qquad (2.13)$$

where $FWHM_{cT}$ and $FWHM_{aT}$ are the timing resolution for the cathode trigger and anode trigger respectively, and T is the maximum electron drift time where the electron drift across the whole detector thickness D.

2.4 Methods to Estimate the Electron Mobility-Lifetime Products

In the presence of electron trapping, the remaining electrons $Q(z)$ after the original electrons Q_0 have drifted a distance z can be described by the equation below:

$$Q(z) = Q_0 e^{-\frac{zD}{(\mathrm{mt})_e V}} \qquad (2.14)$$

where D is the detector thickness, $(\mathrm{mt})_e$ is the electron mobility-lifetime product and V is the cathode bias.

A traditional method to measure the $(\mathrm{mt})_e$ is to irradiate the conventional planar cathode with low energy gamma ray sources, such as [241]Am (59.5 keV). The low energy photons should all be stopped in a thin layer near the cathode. The induced signal on electrodes should all be due to the drifting of the electrons and the changes in the weighting potential and the electron trapping for all interactions in this thin layer should be very small. Therefore, the cathode spectrum should have a fairly sharp photopeak. The photopeak centroid N_c in the cathode spectrum as a function of V and $(\mathrm{mt})_e$ obeys the Hecht relation [72]:

$$N_c = K(\mathrm{mt})_e V (1 - e^{-\frac{D^2}{(\mathrm{mt})_e V}}) \qquad (2.15)$$

where K is a constant. By measuring the variation of the photopeak centroid as a function of V, the $(\mu t)_e$ can be estimated via a curve fitting procedure using Equation 2.15. This method can be used in both single polarity charge sensing detectors and conventional planar detectors, and can be used to measure the $(\mu t)_h$ with reversed biasing. However, several factors may affect the precision of this method, such as the ballistic deficit due to the finite shaping time and varying pulse rise time under different cathode biases, possible material defects near the cathode surface, and the uncertainty in the curve fitting procedure.

He et al. [73] proposed several alternative methods of estimating the $(\mu t)_e$ for coplanar detectors using single-polarity charge sensing and depth sensing techniques. Similar methods can also be applied in pixellated detectors.

The induced signal on the pixel anode by the electrons generated in low energy gamma ray interactions occurring near the cathode surface can be used to estimate the $(\mu t)_e$. With the assumption of perfect small pixel effect in which the weighting potential remains zero inside the detector and rises to unity at the anode pixel, only the electrons collected by the anode pixel contribute to the signal. The photopeak centroid of the anode spectrum can be derived from Equation 2.14:

$$N_a = A e^{-\frac{D^2}{(\mu t)_e V}} \qquad (2.16)$$

where A is a constant. In reality, the weighting potential is close to but not equal to zero in the detector bulk. Equation 2.16 underestimates the true anode signal since those trapped electrons can still contribute to the induced signal before they are trapped. Consequently, the $(\mu t)_e$ will be slightly overestimated using Equation 2.16. More accurately, if the slow change in the weighting potential in the detector bulk is considered and the mean free path of electrons is much larger than the detector thickness

$\left((mt)_e \dfrac{V}{D} ? D\right)$, a better approximation of the induced signal on the anode pixel can be

derived as follows:

$$dq = Q(z)d\jmath(z) = Q_0 e^{-\frac{zD}{(mt)_e V}} d\jmath(z) \tag{2.17}$$

$$\begin{cases} \jmath(0) = 1 \\ \jmath(D) = 0 \end{cases} \tag{2.18}$$

$$Q = \int_D^0 Q_0 e^{-\frac{(D-z)D}{(mt)_e V}} d\jmath(z)$$

$$= Q_0 e^{-\frac{D^2}{(mt)_e V}} \left(e^{\frac{zD}{(mt)_e V}} \jmath(z) \Big|_D^0 - \int_D^0 \jmath(z) de^{\frac{zD}{(mt)_e V}} \right)$$

$$= Q_0 e^{-\frac{D^2}{(mt)_e V}} \left(1 + \frac{D}{(mt)_e V} \int_0^D \jmath(z) e^{\frac{zD}{(mt)_e V}} dz \right) \tag{2.19}$$

$$\cong Q_0 e^{-\frac{D^2}{(mt)_e V}} \left(1 + \frac{D}{(mt)_e V} \int_0^D \jmath(z)(1 + \frac{zD}{(mt)_e V}) dz \right)$$

$$= Q_0 e^{-\frac{D^2}{(mt)_e V}} \left(1 + \frac{D}{(mt)_e V} \int_0^D \jmath(z) dz + \frac{D^2}{(mt)_e^2 V^2} \int_0^D \jmath(z) z dz \right)$$

where $\jmath(z)$ is the weighting potential. Since the third term in the parentheses in Equation

2.19 is much smaller than the second term, Equation 2.19 can be approximated as

$$Q \cong Q_0 e^{-\frac{D^2}{(mt)_e V}} e^{\frac{D \int_0^D \jmath(z) dz}{(mt)_e V}}$$

$$= Q_0 e^{-\frac{D\left(D - \int_0^D \jmath(z) dz\right)}{(mt)_e V}} \tag{2.20}$$

Therefore, Equation 2.16 becomes:

$$N_a = A e^{-\frac{D\left(D - \int_0^D \jmath(z) dz\right)}{(mt)_e V}} \tag{2.21}$$

By measuring the photopeak centroids N_{a1} and N_{a2} under two different cathode

biases V_1 and V_2, the $(mt)_e$ can be calculated as:

$$(mt)_e = \frac{D\left(D - \int_0^D \jmath(z) dz\right)}{\ln(N_{a1}/N_{a2})} \left(\frac{1}{V_2} - \frac{1}{V_1}\right) \tag{2.22}$$

If high energy gamma ray sources are used, the above equation can still be used to measure the $(\mu t)_e$ by taking N_{a1} and N_{a2} as the photopeak centroid for events occurring in the depth layer near the cathode surface.

2.5 Common Mode Noise

In an integrated analog signal readout system with a large number of channels, coherent variation in groups of channels, which is normally referred to as common mode noise, may exist in addition to the normal random noise. This common mode noise can be caused by pick-up of digital signals, noise in the power line, etc. It increases the overall system noise but can sometimes be detected and corrected.

In order to detect common mode noise, the correlation between the noises from different channels needs to be calculated. If we consider the net signal (raw signal subtract the baseline) of two channels x and y, for a large number of events in which neither channel has true signal (net signal exceeding a certain threshold), the net signals x and y are simply noises and the correlation between them is

$$cor_{xy} = \frac{\overline{x \cdot y} - \overline{x} \cdot \overline{y}}{\mathsf{S}_x \cdot \mathsf{S}_y} \qquad (2.23)$$

where the standard deviation is

$$\mathsf{S}_x = \sqrt{\overline{x^2} - \overline{x}^2} \qquad (2.24)$$

If no common mode noise exists, the correlation cor_{xy} of two channels should be zero since the normal random noise will be canceled if the number of events is sufficiently large. If there is common mode noise, the correlation should most likely be a positive value. The full noise correlation matrix for all channels can be established by calculating this quantity for all pairs of channels. One great benefit of correlation matrix is its ability to reveal the range of coherence in a visible way and may help to diagnose the source of the common mode noise. For example, square regions of non-zero

correlation in a correlation matrix represent local common mode effects among channels in the same group but not across different groups. Figure 2.4(a) illustrates a typical correlation matrix of common mode noise for groups of 4 channels. It is also straightforward that band structure around the diagonal of the correlation matrix suggests the existence of common mode noise due to cross-talk between neighboring channels, as can be seen in Figure 2.4(b).
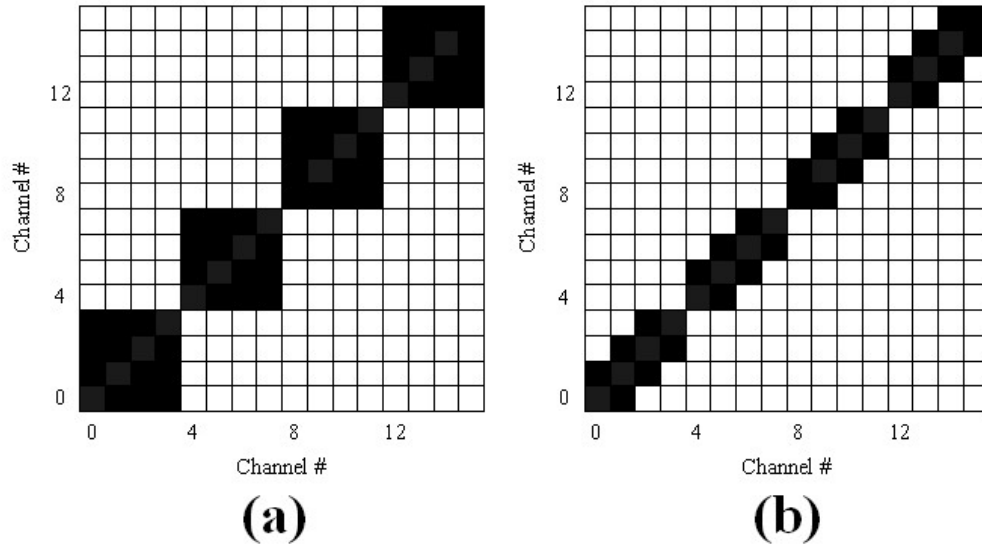
Figure 2.4. Illustrations of channel-noise correlation matrix due to different common mode noise. Assuming four channels per chip and four chips. Black represents correlation of 1.0 and white is 0. (a). All four channels on one chip have common mode noise. (b). Neighboring channels have common mode noise due to cross-talk.

When common mode noise is detected, the correction of common mode noise can be carried out on an event-by-event basis. For a group of correlated channels, the net signals are first obtained by subtracting the baselines from the raw signals and those channels with true signals (net signal exceeding a certain noise threshold) are excluded. Then, add or subtract the net signals of all remaining channels according to the sign of

the correlation and calculate the average value, which should be a good approximation to the common mode noise. The common mode noise can then be corrected by subtracting this average value from the signals.

CHAPTER 3

MODELING

3.1 Energy Deposition Simulation

In order to better understand the factors affecting the performance of the 3-D CdZnTe gamma ray spectrometers, it is necessary to simulate how the gamma ray interacts and deposits energy inside the detector. The electron cloud size needs to be estimated and compared with the pixel pitch. The charge sharing among the neighboring pixels needs to be investigated to determine its effect on the fraction and energy resolution of the multiple-pixel events. It is also important to find out the proper triggering threshold to minimize the reduction in detection efficiency.

Geant4 [74], a free Monte-Carlo simulation software package developed by CERN, has been used for this study. With the help of its support of many physics models and its transparent object-oriented framework, the gamma-ray interactions inside CdZnTe and the ionization processes of the energetic electrons created in the interactions can be easily and accurately simulated.

3.1.1 Simulation setup

The CdZnTe crystal has a dimension of 15 mm × 15 mm × 10 mm. On one 15 mm × 15 mm surface is a pattern of 11 × 11 pixel-grid anodes, as shown in Figure 3.1. The pixel pitch is 1.27 mm, the grid has a width of 100 µm and there is a 200 µm gap

between the pixel and the grid. Due to the limitation in the electrode fabrication process, the outermost boundary of the grid is wider (~0.5 mm).

To simplify the simulation, the grid and the gap were ignored and it was assumed that the electrons created within one pixel pitch (including the pixel area, the gap area and the corresponding grid area) were collected by that pixel. The detector was irradiated by a ^{137}Cs flood source from the cathode side.
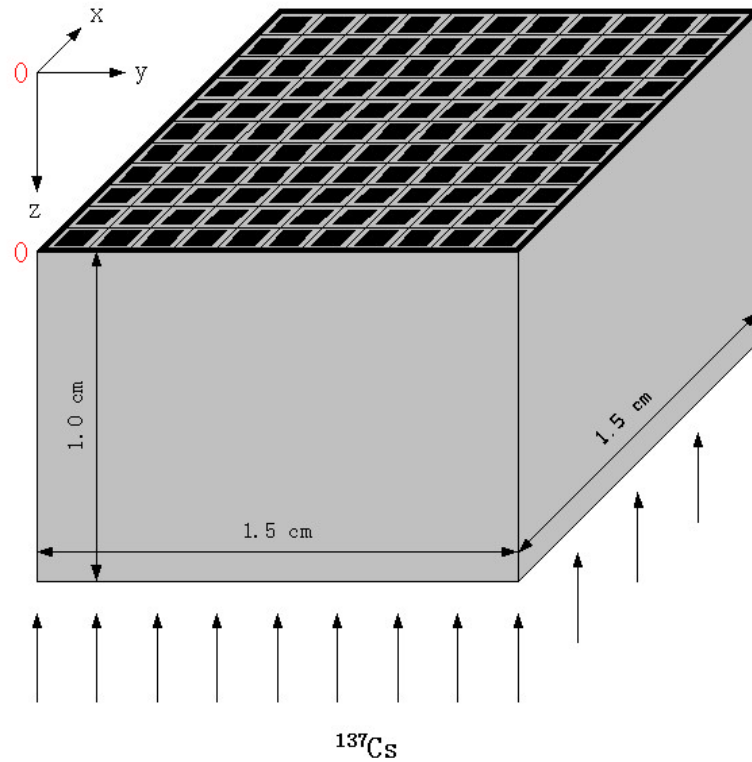
Figure 3.1. Simulation geometry setup.

3.1.2 Electron cloud size

The first step in the simulation is to get a feeling of the size of the electron cloud created by the gamma ray interaction. Surely the electron cloud size increases as the energy deposited by the interaction increases. Larger electron cloud size results in higher possibility of charge sharing - the electrons created by one interaction are collected by

31

more than one pixel, which causes complication in the event reconstruction and performance degradation due to charge loss.
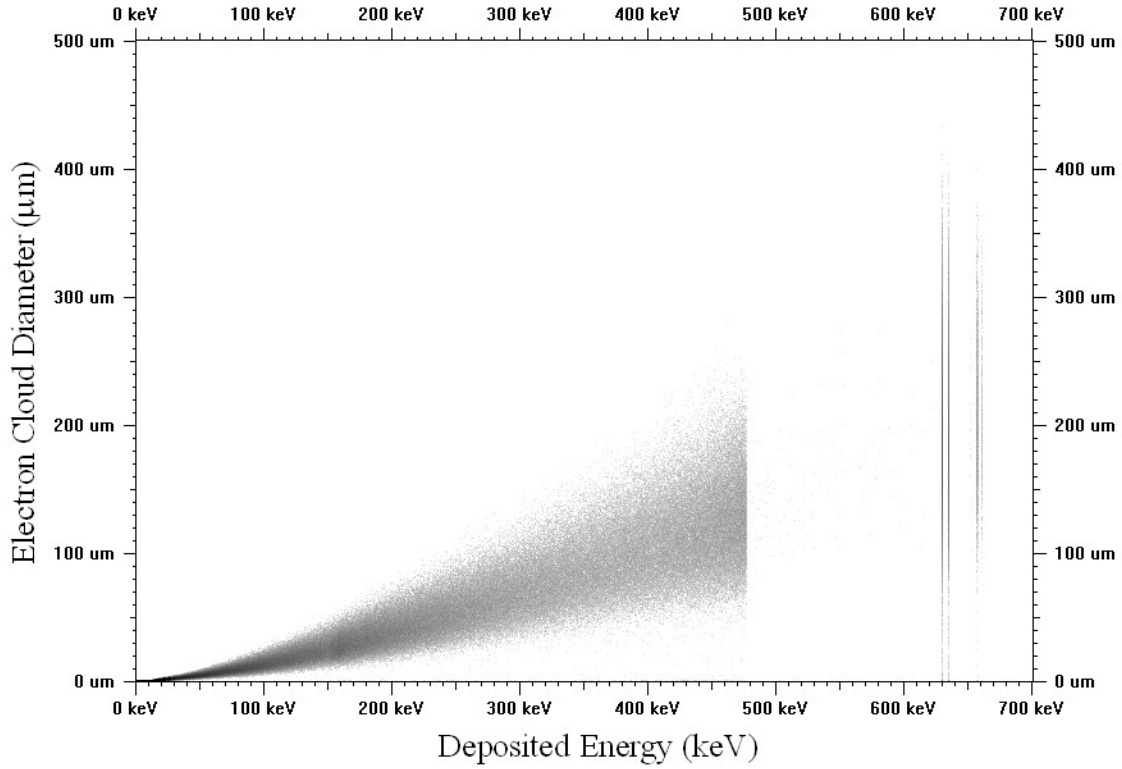
Figure 3.2. Simulation results of the electron cloud diameter for 662 keV incident gamma-ray interactions with different deposited energies. The horizontal axis is the deposited energy in keV and the vertical axis is the electron cloud diameter in μm.

The sizes of the electron clouds can be estimated by tracking the ionization process and recording the coordinates of energy depositions by secondary electrons. This was first done for 662 keV gamma rays. The electron cloud diameter vs. the deposited energy is shown in Figure 3.2. The increase in electron cloud size with the increase in deposited energy is very obvious. The mean electron cloud diameter for 662 keV energy depositions is estimated to be around 220 μm, relatively small but still comparable to the 1.27 mm pixel pitch.

For higher energy depositions, the electron cloud diameter can increase dramatically. Figure 3.3 shows the comparison of the electron cloud diameter for 662 keV, 1.3 MeV and 2.6 MeV energy depositions. Although the mean electron cloud diameter at 2.6 MeV is ~1.3 mm, larger than the 1.27 mm pixel pitch, the possibility of depositing 2.6 MeV in one interaction is very low. However, the mean electron cloud diameter of ~0.5 mm at 1.3 MeV is already comparable with the pixel pitch. Therefore, a large fraction of 1.3 MeV energy depositions are shared by multiple pixels. It is important to minimize the charge loss in the gap, reduce the low-energy threshold of the anode pixels and find out a way to properly reconstruct the charge sharing events.

3.1.3 Fractions of multiple-pixel events

While drifting towards the anode under the electric field, the electrons also diffuse away from their point of origin due to random thermal motion. Therefore, in addition to the original electron cloud size, the diffusion of the electrons should also be taken into account in the simulation. The spread in the electron collecting point due to this diffusion can be approximated by a Gaussian distribution with an standard deviation of [8]:

$$\mathrm{s} = \sqrt{\frac{2kTd}{eE}} \tag{3.1}$$

where k is the Boltzmann constant, T is the absolute temperature, d is the drift distance, e is the unit charge and E is the electric field. At $20°C$ (293K), the numerical value of $\frac{kT}{e}$ is 0.0253 V.
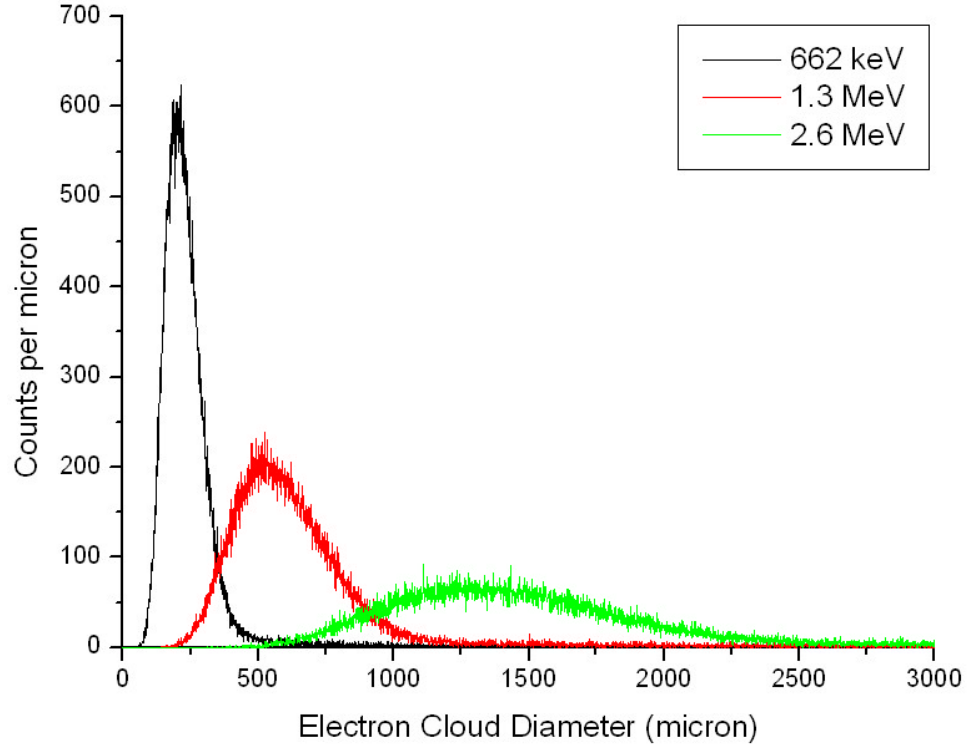
Figure 3.3. Simulation results of the electron cloud size for three different energies of photoelectron.

The electric field E can be expressed as

$$E = \frac{V}{D} \qquad (3.2)$$

where V is the cathode bias in volts and D is the detector thickness. Thus, the FWHM of the diffused distribution is

$$FWHM(d,V) = 2.35\sqrt{\frac{2kTdD}{eV}} = 2.35\sqrt{2 \times 0.0253 \times \frac{dD}{V}} = 0.529\sqrt{\frac{dD}{V}} \qquad (3.3)$$

The detector used in this study has a thickness of 10 mm. The maximum diffusion FWHM (interactions on the cathode side) for three different cathode biases are calculated and compared in Table 3.1. It can be clearly seen that even at -2000 V cathode bias, the electron cloud still has an additional spread of 118 μm due to the diffusion.

Table 3.1. Maximum electron diffusion FWHM for different cathode biases.

Cathode Bias (V)	-1000	-1400	-2000
Diffusion FWHM (μm)	167	141	118

In the simulation, the cut value for the electron is set to 1 μm so that each discrete energy deposition by the ionization process is localized within the 1 μm spot. The energy deposition is assumed to evenly distribute within a circular area with a diameter of the calculated diffusion FWHM calculated from the depth of the energy deposition via Equation 3.3. All pixels intersecting this circular area will share the deposited energy according to the intersected area.

Figure 3.4 shows the fractions of the 662 keV single-pixel and multiple-pixel photopeak events under different simulation conditions. It can be clearly seen that by considering the electron cloud size and the electron diffusion, the fraction of single-pixel photopeak events decreases while the fraction of multiple-pixel photopeak events increases due to more and more charge sharing. At -2000 V cathode bias, only ~30% of 662 keV photopeak events are single-pixel events, nearly 40% are two-pixel events, and ~20% are three-pixel events.

Figure 3.5 shows the fractions of single-pixel and multiple-pixel photopeak events for three different gamma-ray energies at -2000 V cathode bias. The fractions of multiple-pixel photopeak events increase as the gamma-ray energy increases. Therefore, proper reconstruction of multiple-pixel events is essential for high detection efficiency, especially for high-energy gamma rays.

Table 3.2 shows the simulation results of pixel sharing (multiple interactions under the same pixel) and charge sharing for three different gamma-ray energies and two different detector sizes and pixel pitches. Higher cathode bias is applied to thicker detector to ensure the same electric field magnitude (200 V/mm) for both detectors. It is

not surprising to see that the pixel sharing increases with the gamma-ray energy and the pixel pitch, while the charge sharing decreases with larger pixel pitch and increases with higher gamma ray energy. Once again it confirms that charge sharing will be a dominant factor in the high-energy gamma-ray detection.
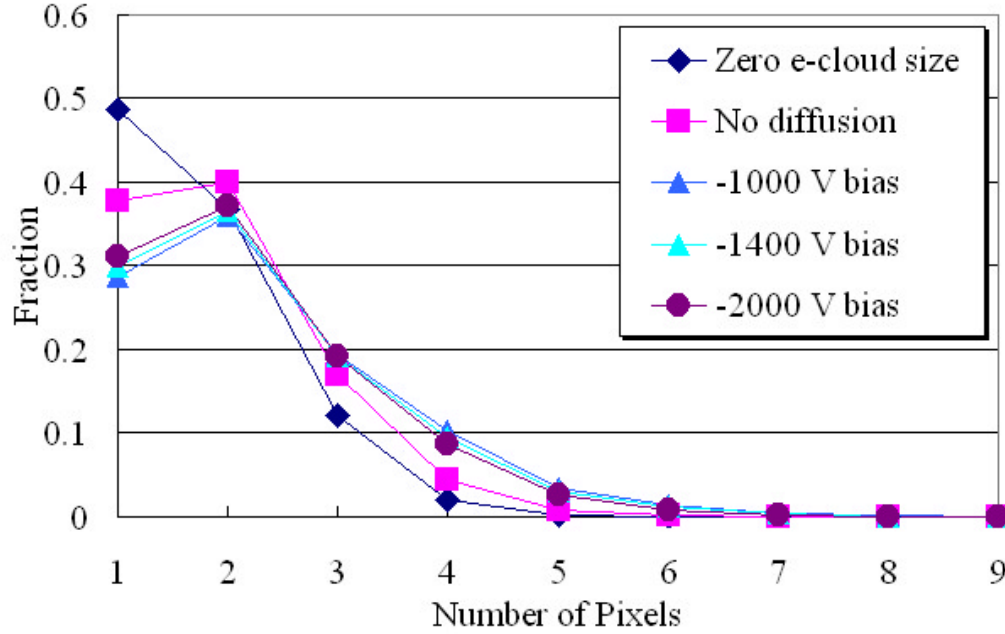
Figure 3.4. Fractions of the 662 keV single-pixel and multiple-pixel photopeak events under different simulation conditions.
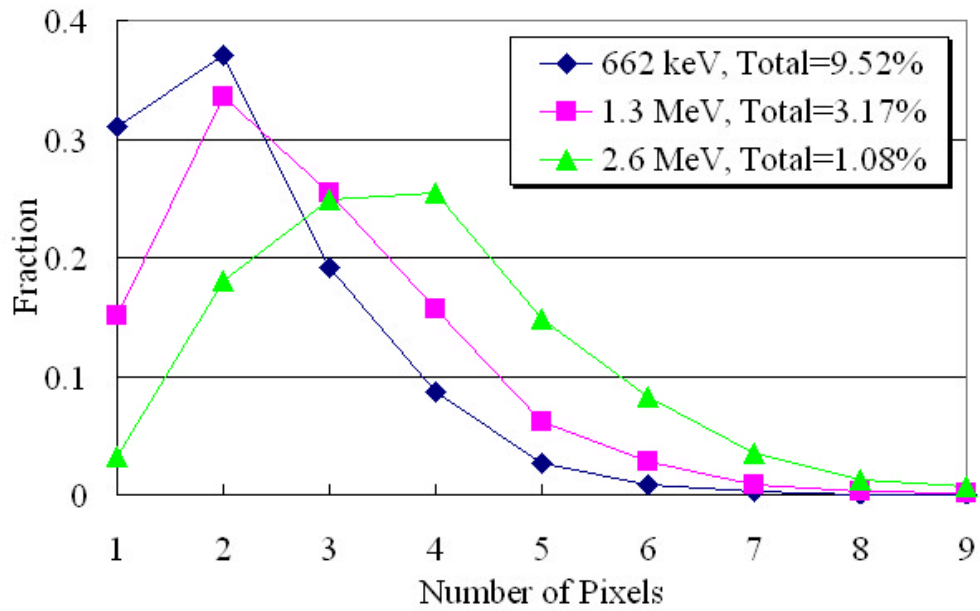
Figure 3.5. Fraction of single-pixel and multiple-pixel events for three different gamma ray energies. The total intrinsic photopeak efficiencies for the whole detector are also shown in the legends. The cathode bias is set to -2000 V.
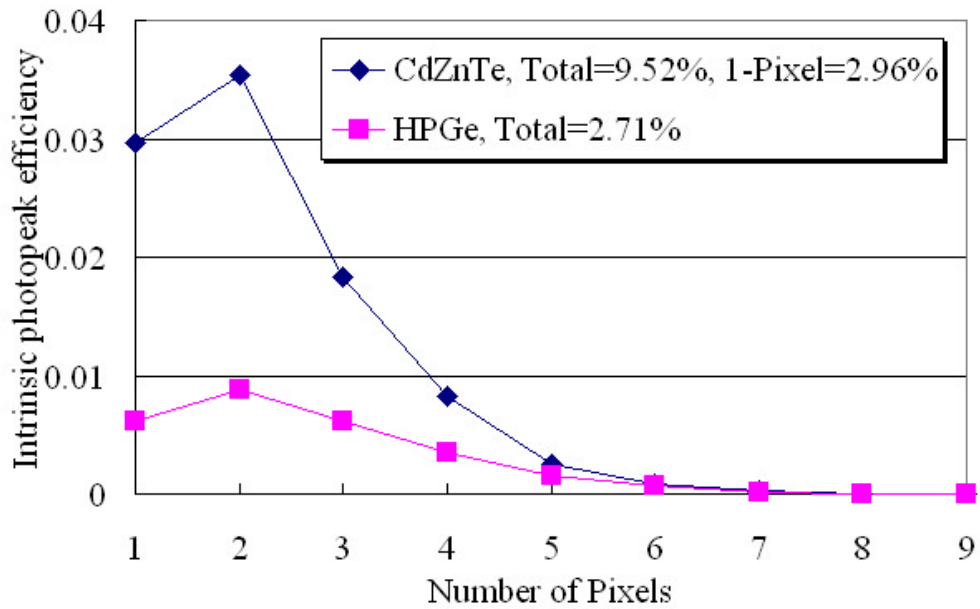
Figure 3.6. Intrinsic photopeak efficiency of single-pixel and multiple-pixel events at 662 keV for a CdZnTe and a HPGe detector of the same size (1.5 cm × 1.5 cm × 1.0 cm). The cathode bias is set to -2000 V.

Table 3.2. Simulated intrinsic photopeak efficiency, fraction of events having multiple interactions under the same pixel and fraction of charge-sharing events for three different gamma-ray energies and two different detector configurations.

Energy	Detector configuration and cathode bias	Intrinsic photopeak efficiency	Full energy deposit – multiple interactions under the same pixel	Full energy deposit - charge sharing events
662 keV	15×15×10 mm 1.27 mm pitch -2000 V	9.52%	21%	31.9%
	20×20×15 mm 1.82 mm pitch -3000 V	15.8%	25.7%	28.4%
1.3 MeV	15×15×10 mm 1.27 mm pitch -2000 V	3.17%	25.3%	45%
	20×20×15 mm 1.82 mm pitch -3000 V	6.02%	30.8%	39.2%
2.6 MeV	15×15×10 mm 1.27 mm pitch -2000 V	1.08%	28%	62.2%
	20×20×15 mm 1.82 mm pitch -3000 V	2.32%	32.9%	52.8%

A simulation was also done to compare the intrinsic photopeak efficiency at 662 keV of a CdZnTe and a HPGe detector of the size (1.5 cm × 1.5 cm × 1.0 cm) and the same pixellated electrodes. The high atomic number of CdZnTe helps it to achieve much higher photopeak efficiency than HPGe, as can be seen in Figure 3.6. Even the number of single-pixel events in CdZnTe is higher than the number of all photopeak events in HPGe. If the energy resolution for single-pixel events can be improved to approach that of HPGe and detector arrays are used to increase the sensitive volume, 3-D CdZnTe spectrometers could be very attractive due to their room temperature operation and the

imaging capability. If multiple-pixel events can be correctly reconstructed to approach the energy resolution of single-pixel events, significant efficiency advantage could be achieved over HPGe gamma-ray spectrometers.

3.1.4 Effects of triggering threshold

Figure 3.7 shows the comparison of event rate for "valid" 662 keV photopeak events with different thresholds. A "valid" photopeak event refers to an event that all the pixels that have a signal higher than the event-selection threshold (~10 keV) also have the signal higher than the anode triggering threshold.
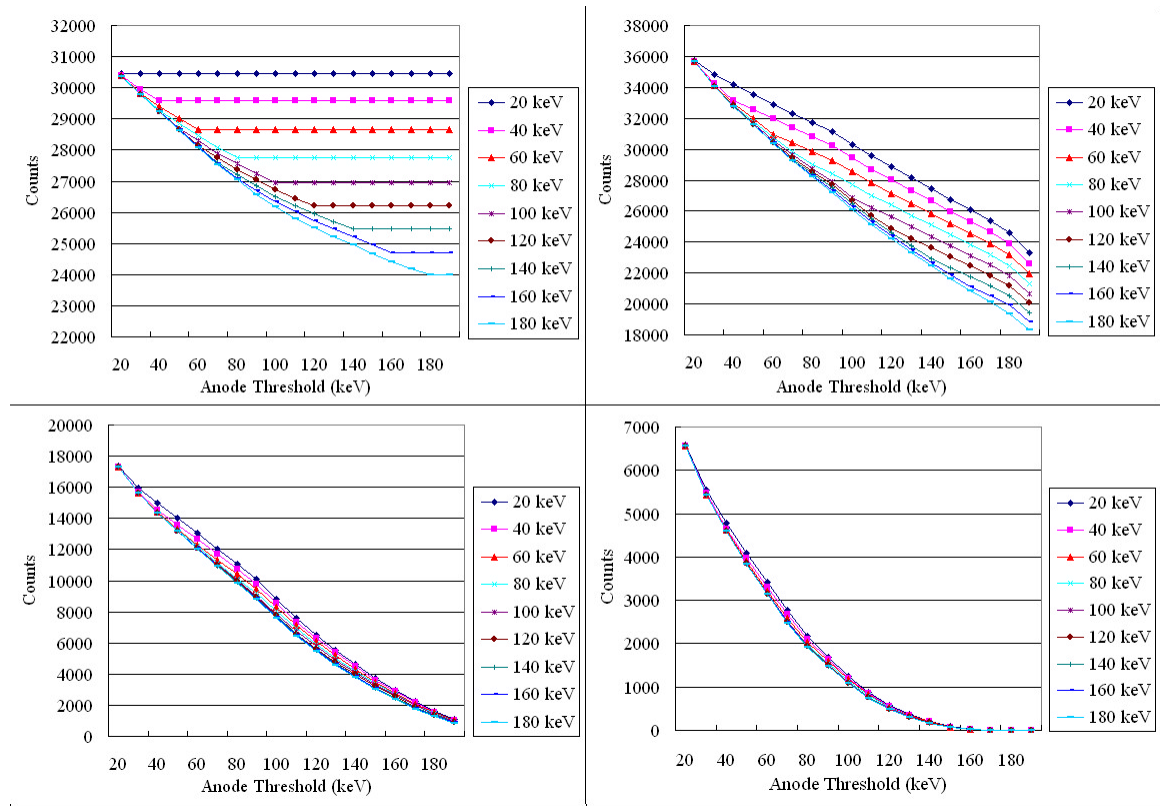
Figure 3.7. Valid 662 keV photopeak events count vs. anode threshold (keV). Data of different color are for different cathode thresholds. (a). Single-pixel events. (b). Two-pixel events. (c). Three-pixel events. (d). Four-pixel events.

Figure 3.7 clearly shows that lower anode triggering threshold results in less loss in the photopeak efficiency. An anode triggering threshold of 20-30 keV is needed to capture 90% of multiple pixel photopeak events. On the other hand, although unlikely, if for some reason the anode triggering threshold is fairly high, a low cathode triggering threshold is necessary for single-pixel events and two-pixel events, but not very influential for three-pixel and four-pixel events.

3.2 Weighting Potential Simulation

According to Shockley-Ramo theorem, if all electrodes of a detector are biased at constant potentials, the induced charge on an electrode due to a point space charge in the detector can be determined from the weighting potential produced by that electrode. The weighting potential can be calculated by solving the Laplace equation with proper boundary conditions. However, it is difficult to find an analytical solution of the weighting potential for a complex electrode configuration. Alternatively, finite element analysis software Maxwell-3D [65] was used in this study to calculate the weighting potential. Using Maxwell-3D's Electrostatic Field Solver, the electric field strength and electric-flux density fields due to space charges and applied potentials can be calculated and used to derive other quantities such as force, torque, energy, and capacitance.

3.2.1 Weighting potential of one pixel and the cathode

By setting the potential of the interested electrode to 1 and the potential of all other electrodes to 0, the weighting potential can be calculated via Maxwell-3D. Figure 3.8 shows the calculated weighting potential of one anode pixel and the cathode as a function of the depth. The weighting potential of the anode pixel starts from 0 at the cathode surface, remains low and slowly increases towards the anode side, and rises

rapidly to 1 in a region of approximately one pixel pitch away from the anode surface. On the contrary, the weighting potential of the cathode increases linearly as the depth increases.

As discussed in Chapter 2, assuming the holes don't move at all, the induced signal on the electrode is the weighting potential difference between the location where the charges are created and the location where the charges are collected. Therefore, the signal induced on the anode pixel by the drifting electrons will only have very weak dependence on the interaction depth for most of the detector thickness except the region very close to the anode surface, while the signal induced on the cathode will be linearly dependent on the interaction depth. Thus, the interaction depth can be derived from the cathode to anode signal ratio (C/A ratio), as shown in Figure 3.9. It can be clearly seen that the C/A ratio has a linear relation with the depth except in the region one pixel pitch away from the anode surface.
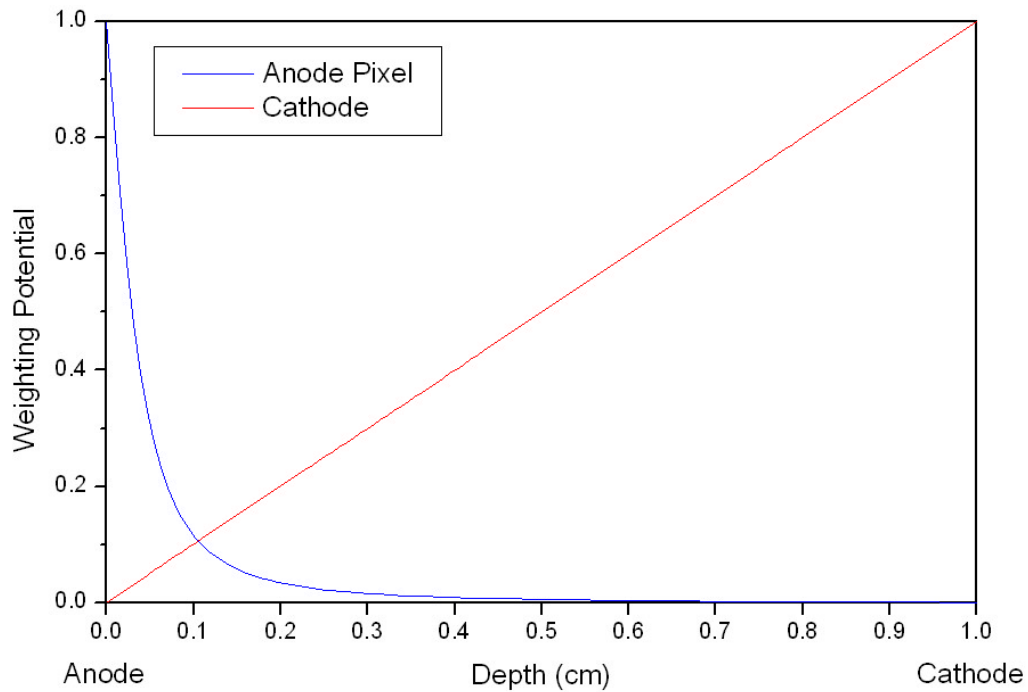
Figure 3.8. Weighting potential of one anode pixel (blue) and of the cathode (red).

41
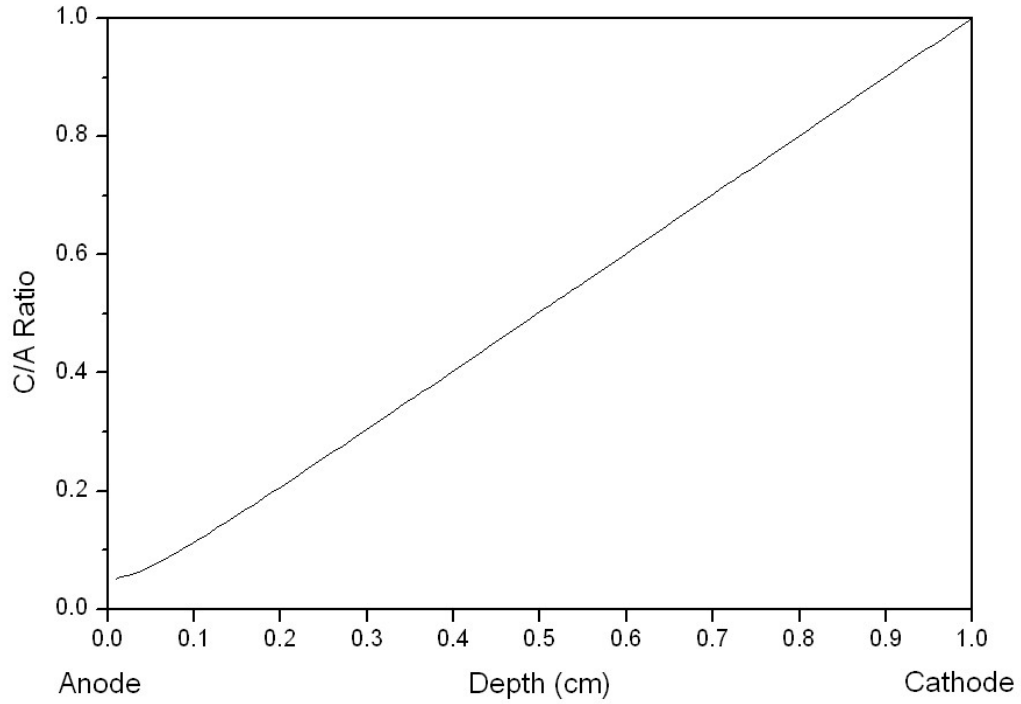
Figure 3.9. Cathode to anode signal ratio vs. interaction depth without considering electron trapping and hole contribution.

3.2.2 Weighting potential cross-talk

When the electrons drift toward the anode, they induce signals not only on the collecting anode pixels directly above them; they also induce signals on other pixels, especially on the neighboring pixels that are nearest to the collecting pixel. In detector materials with similar electron and hole mobilities, the induced signals on the non-collecting pixels are transient and integrate to zero net charge. The hole contribution exactly cancels the electron contribution. However, for CdZnTe and other detector materials with poor hole transport, there is a net induced charge on the neighboring pixels. The induced signal on the neighboring pixels will first gradually rise as the electrons move towards the anode pixels, reach the highest at around one pixel pitch away from the anode, and then quickly fall to zero as the electrons are collected by the

42

collecting pixel. Therefore, this is a transient signal and the net induced signal on the neighboring pixel will always be negative or zero. We call this phenomenon "weighting potential cross-talk." The magnitudes of weighting potential cross-talk on a neighboring pixel when the electron clouds are at different lateral locations under the collecting pixels are shown in Figure 3.10.
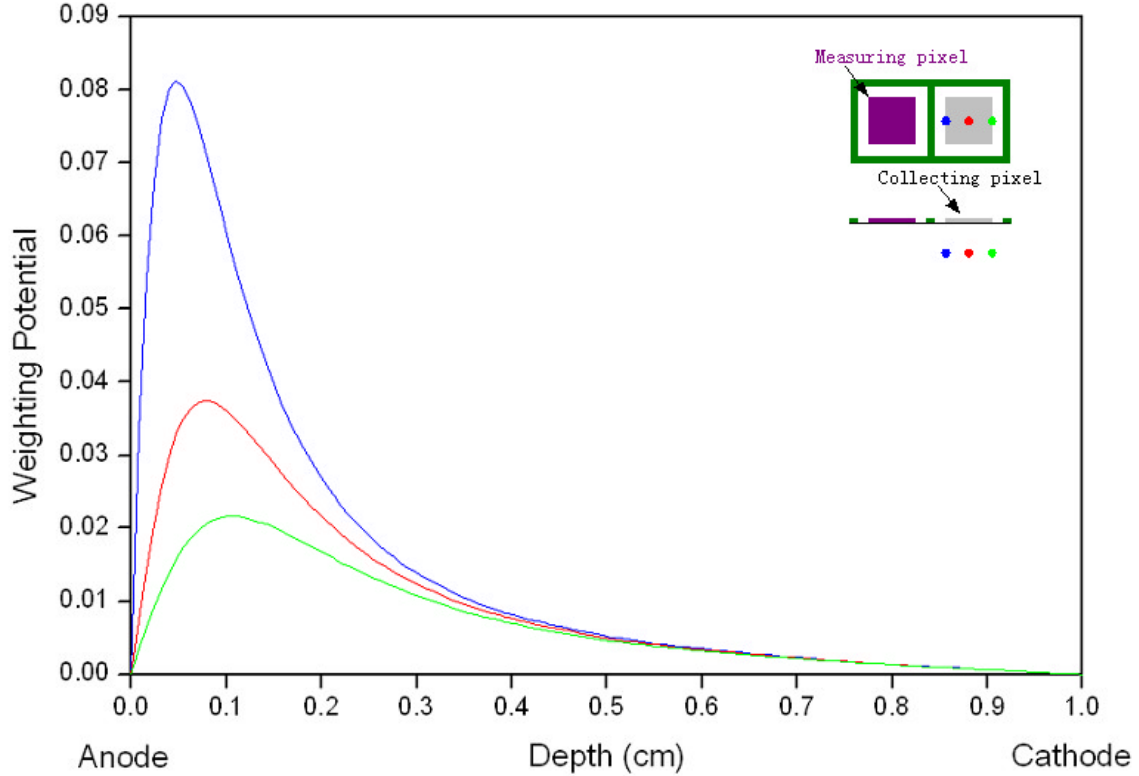
Figure 3.10. Weighting potential cross-talk on a neighboring pixel when the electron clouds are at different lateral positions under the collecting pixel.

This is not a problem for single-pixel events as long as the induced signal is not high enough to trigger the neighboring pixels. However, it becomes problematic for multiple-pixel events. If two interactions occur under neighboring pixels, then each pixel acts as both a collecting and a non-collecting pixel. The observed signal amplitude on each pixel is the sum of the induced charge from the event under that pixel (a positive

43

signal) plus the cross talk contribution from the event under the neighboring pixel (a negative signal).

3.3 Timing Resolution and Amplitude Walk

Electron drift time is obtained from the leading-edge triggering time difference between the cathode signal and the anode signals. In the current 3-D CZT systems, a CR-RC shaper with a 75 ns shaping time and a simple discriminator are used in each channel to retrieve the leading edge timing information from both the anode signals and the cathode signal. The detector is 1 cm thick and biased at -2000 V on the cathode. Assuming a normal electron mobility of 1000 cm^2/V·s, the maximum electron drift time is 0.5 μs. A simple model shown in Figure 3.11 was created using the Simulink toolbox in Matlab [66] to simulate the shaper output waveforms of the cathode and the anode signals. The timing resolution and amplitude walk were then calculated from these waveforms.

Simplification in the input pulse waveform was made in the simulation. The anode signal was assumed to remain zero until the electrons drift within one tenth of the detector thickness near the anode and then linearly rise to the full amplitude in 0.05 μs, as shown in Figure 3.14(a).
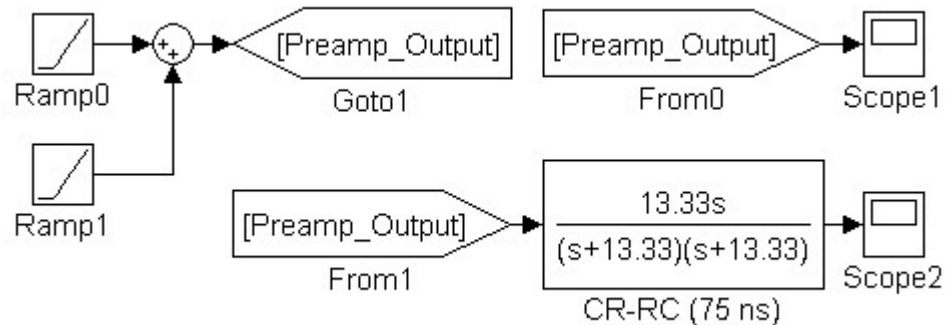
Figure 3.11. Simple simulation model created in Simulink [66] for the shaper in the timing channel.
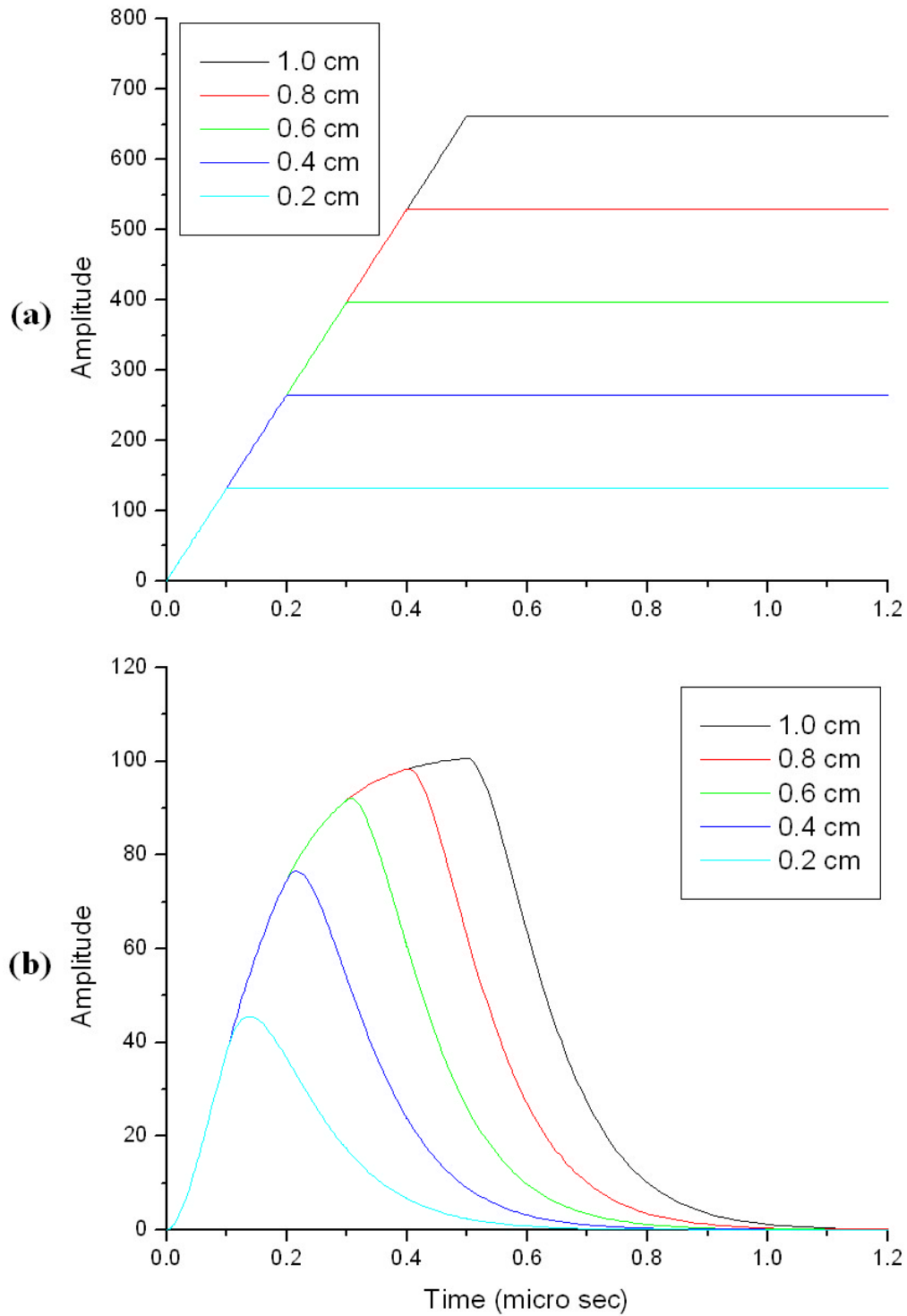
Figure 3.12. Simulated cathode signal pulse waveforms for the same energy deposition at different interaction depths. Assuming 75 ns shaping time. (a). Preamplifier output. (b). Shaper output simulated using Simulink.
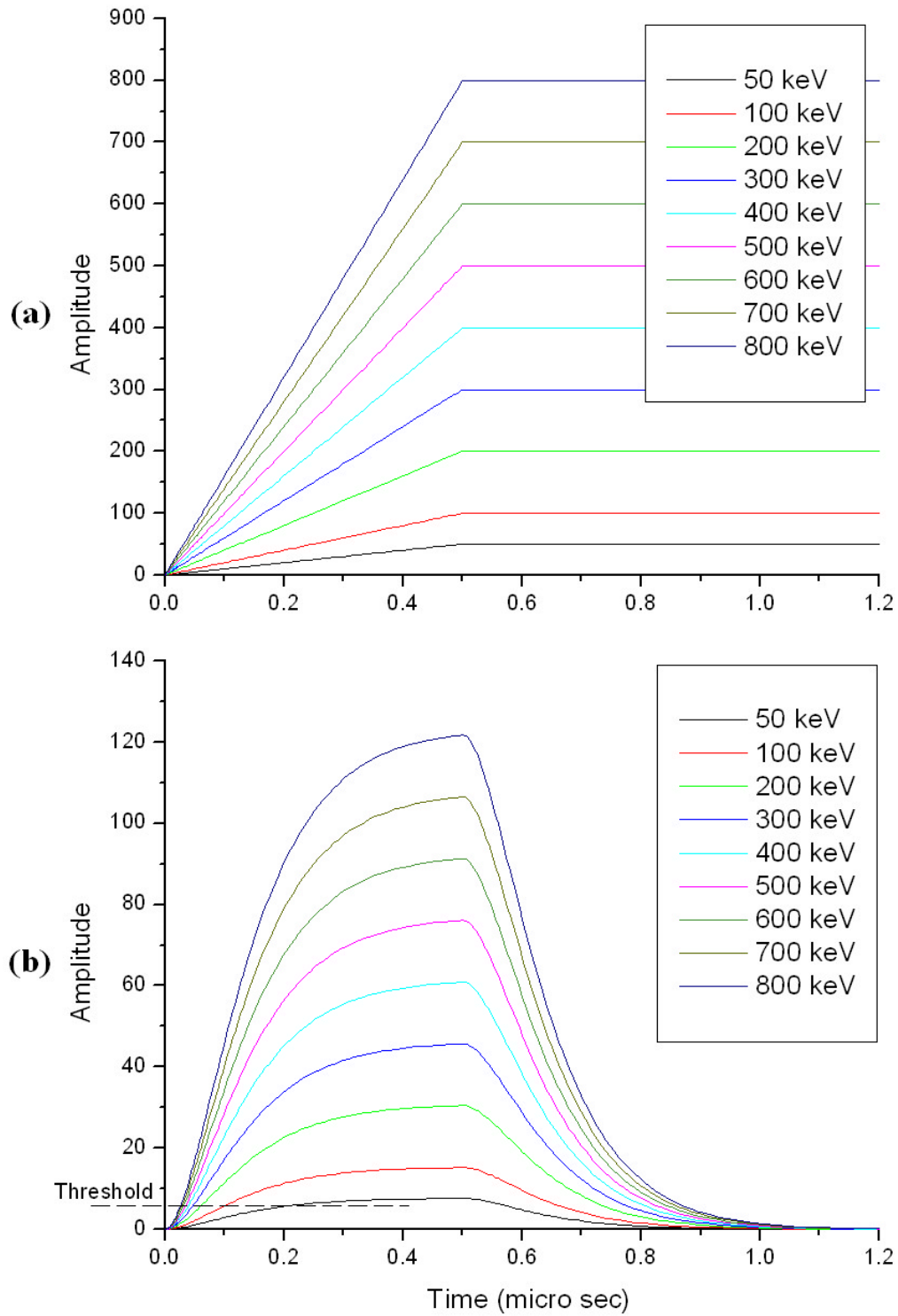
Figure 3.13. Simulated cathode signal pulse waveforms for different energy depositions near the cathode. Assuming 75 ns shaping time. (a). Preamplifier output. (b). Shaper output simulated using Simulink.

46
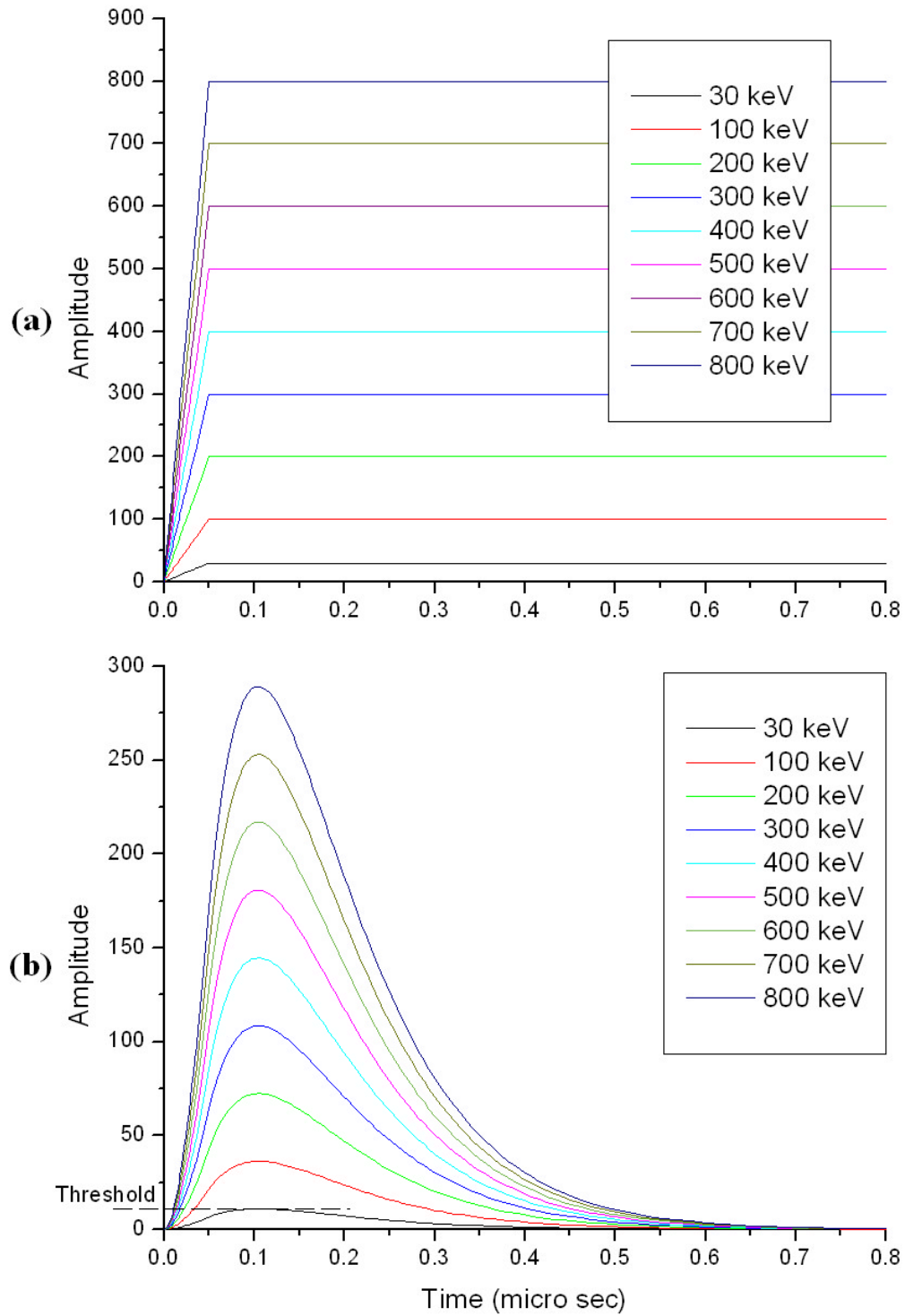
Figure 3.14. Simulated anode signal pulse waveforms for different energy depositions. (a). Preamplifier output. Assuming 75 ns shaping time. (b). Shaper output simulated using Simulink.

Figure 3.12 shows the preamplifier and shaper output waveform for the cathode signal when the same energy deposition happens at different depths. We can see the leading edges of the shaper output waveforms have the same slope. Therefore, with a constant and adequately low threshold, the timing is independent of the interaction depth for most of the detector thickness. However, for different amounts of energy deposition, there is amplitude walk in both the cathode signal and the anode signal, as can be clearly seen in Figure 3.13(b) and Figure 3.14(b). Assuming 40 keV cathode triggering threshold and 30 keV anode triggering threshold, the amplitude walks were measured for different energy depositions and compared in Figure 3.15(a) for the cathode and the anode. The amplitude walk increases as the energy deposition decreases. The amplitude walk in the anode signal is lower than that in the cathode signal due to the much faster anode pulse.

By assuming the 5 keV FWHM and 7 keV FWHM electronic noise in the energy channels (1.0 μs shaping time) of current 3-D CZT systems for the anode signal and the cathode signal, respectively, due to the white noise in the preamplifier output, the equivalent electronic noise in the timing channel shaper output was calculated and used to estimate the timing resolution. The estimated timing resolution was compared in Figure 3.15(b) for the cathode and the anode. The timing resolution degrades as the energy deposition decreases due to poorer signal-to-noise ratio. The timing resolution of the cathode signal is much worse than the anode signal and is the dominant factor in the overall timing resolution. Since the electron drift time is derived from the timing difference of the cathode and anode signals, the depth resolution derived from electron drift times can be calculated using Equation (2.13). It can be easily calculated that the timing resolution is 18 ns FWHM for 662 keV energy deposition and 44 ns FWHM for 200 keV energy deposition. Giving the maximum electron drift time of 0.5 μs, the

resolution of the interaction depth derived from the electron drift time is 0.36 mm

FWHM and 0.88 mm FWHM at 662 keV and 200 keV, respectively.
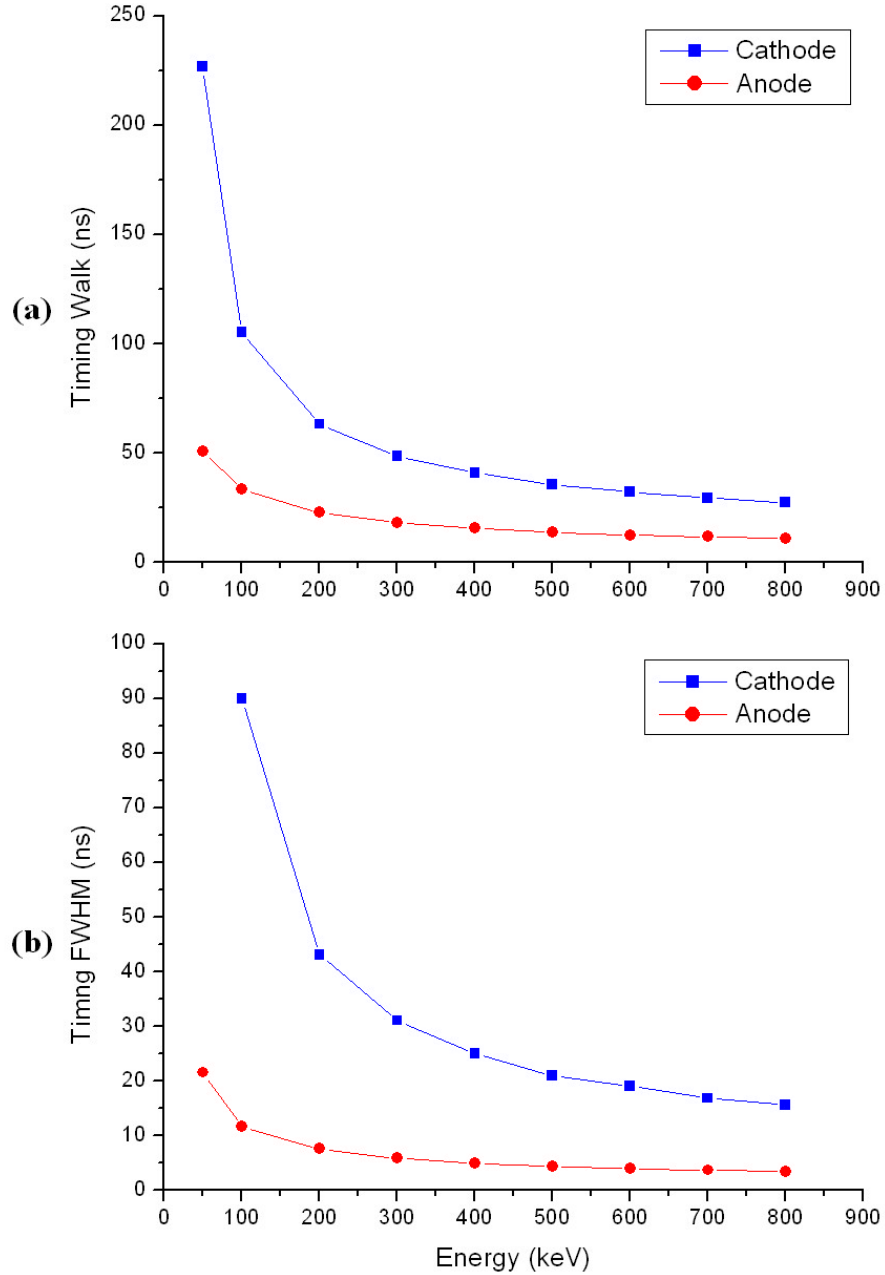
Figure 3.15. Estimated timing walk (a) and timing resolution (b) of the cathode and anode signal from single-pixel events. Assuming ~5 keV FWHM and ~7 keV FWHM electronic noise after 1 μs shaping for the anode and cathode signal respectively. Assuming 75 ns shaping time for the fast shaper.

CHAPTER 4
SYSTEMS

Three iterations of ASIC development have been carried out by the collaboration between Ideas ASA and our group – including VAS2/TAT2, VAS3/TAT3 and VAS3.1/TAT3. The basic structures of these ASICs are similar. Therefore, VAS2/TAT2 will be used as an example to introduce the principle of the readout system.

The electronic readout system is based on the VAS2/TAT2 ASIC chipsets. The VAS2 (Voltage ASIC with Stretcher, version 2) channels are used to read out the induced charges on the anode pixels. The TAT2 (Trigger ASIC with Timing, version 2) channels are used to trigger the system and read out the electron drift times. One VAS2 chip and one TAT2 chip form a chipset. The preamplifier output of each VAS2 channel is wire-bonded to the input of each TAT2 channel. Four chipsets are needed for each 121-pixel CdZnTe detector.

4.1 VAS2/TAT2 System

4.1.1 ASIC structure

Each VAS2 chip has 32 independent channels, each consisting of a preamplifier, a 1-μs-shaping-time shaping amplifier and a peak-hold and sample-hold circuit. The first channel on each VAS2 chip has an opposite polarity to the other 31 channels, to read out the signal from the cathode. Figure 4.1 shows the basic structure of a single VAS2/TAT2 channel. Because the anode pixels are directly connected to the ASIC inputs (DC

coupled), a leakage current compensation circuit (cf. Figure 4.2) is added to each channel, working as AC-equivalent coupling.

Each TAT2 chip also has 32 channels, each channel having a 75-ns-shaping-time fast shaper, a discriminator for triggering and a TAC for electron drift time sensing. A trigger mask can be set to disable those channels having high noise.
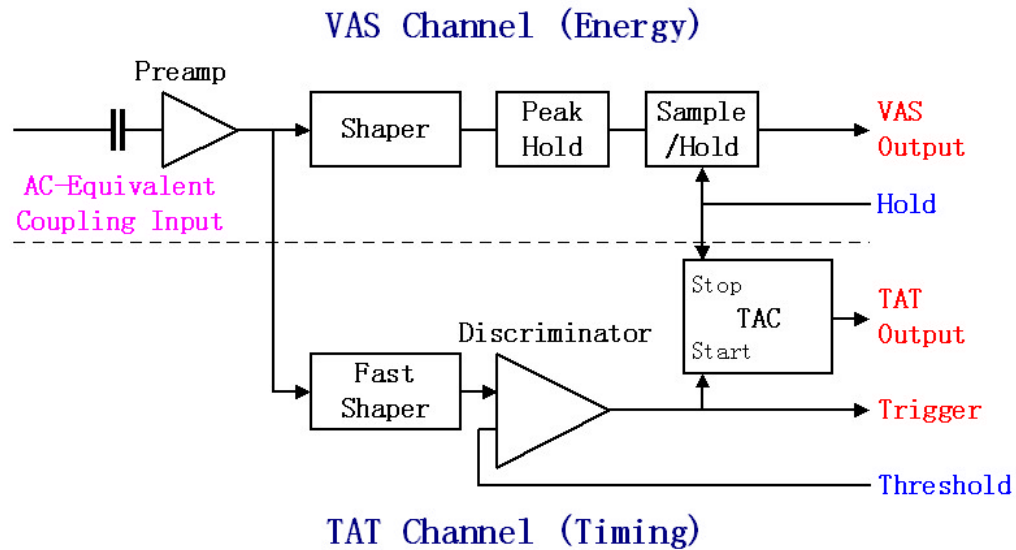
Figure 4.1. Illustration for the VAS2 (energy) and the TAT2 (timing) channels.
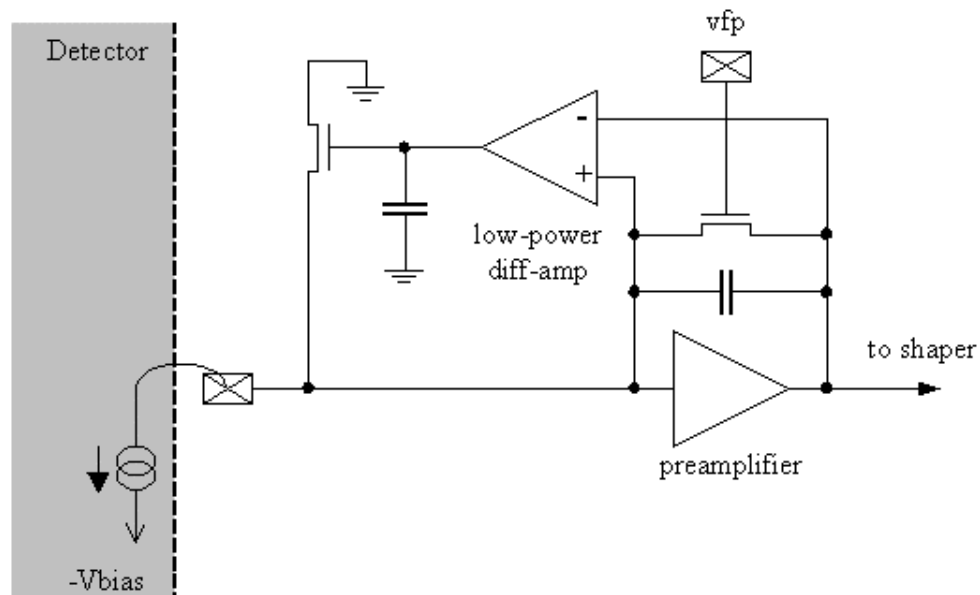
Figure 4.2. The current compensation principle [75].

4.1.2 Detector

Each detector has an 11×11 pixellated anode and a single cathode on a $1.5 \times 1.5 \times 1.0$ cm^3 CZT crystal, fabricated by eV-PRODUCTS. The pixel pitch is 1.27 mm. There is a common grid between pixel anodes biased at negative voltage to focus the electrons to the pixel anodes. The trace width of the grid electrode is 100 μm with a 200 μm gap between the grid and the pixel. The anode pixel-grid pattern and the pictures of the detector are shown in Figure 4.3(A)-(C). The CZT crystal is mounted on a ceramic plate (cf. Figure 4.3(B)). The conducting traces within the multi-layer ceramic plate connect every pixel anode to a corresponding metal pad on the periphery of the plate (cf. Figure 4.3(C)). Four VAS2/TAT2 chipsets are mounted on the front-end board to read out signals from 121 anode pixels and the cathode. A short wire-bond connects each pad on the ceramic plate to the input of each ASIC channel on the front-end board, as can be seen in Figure 4.3(D). The detector and the front-end board are mounted with a PVC plastic holder and placed inside an aluminum box, as shown in Figure 4.4. Two Amptek [76] PC-250 preamplifier boards are used to monitor the grid signal and provide bias voltages to the grid and the cathode.

4.1.3 System Structure

Figure 4.5 shows the basic system configuration of the 3D-CZT system. The CdZnTe detector and ASIC front-end board hybrid set is placed inside a metal box. A controller and repeater card (MCR3) generates and sends the readout clock signals to the ASIC and also converts the output of the ASIC to the voltage signal needed at the input of the data acquisition (DAQ) board. A PCI-6110 DAQ board from National Instruments [77] is used as the A/D converter and as the controller interface between the DAQ program and the detector system.
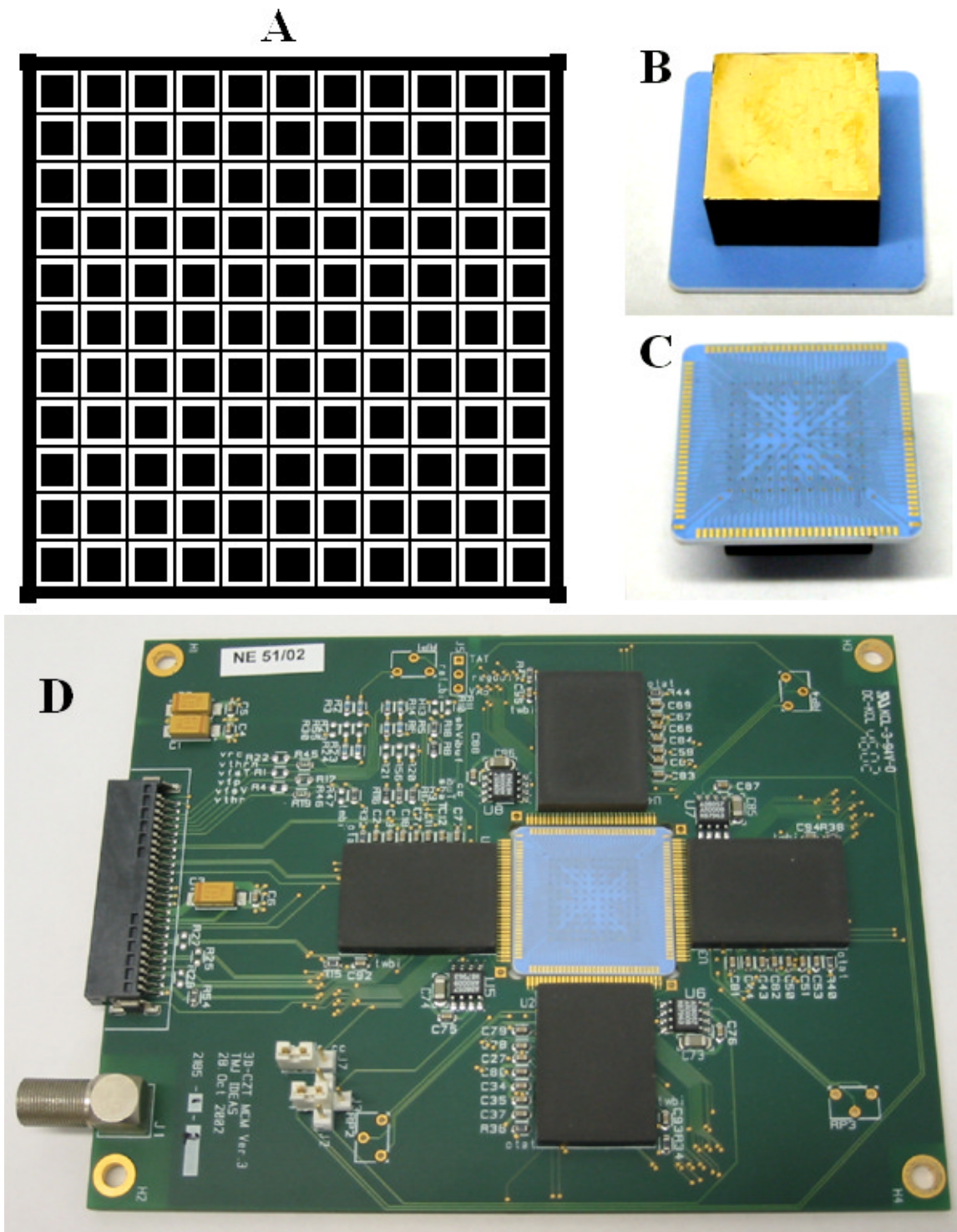
Figure 4.3. (A). 11×11 anode pixel-grid pattern. (B). Photo of the detector with the cathode facing up. (C). Photo of the detector with the ceramic substrate facing up. (D). Hybrid set - ASIC front-end board with the detector placed inside the hole.
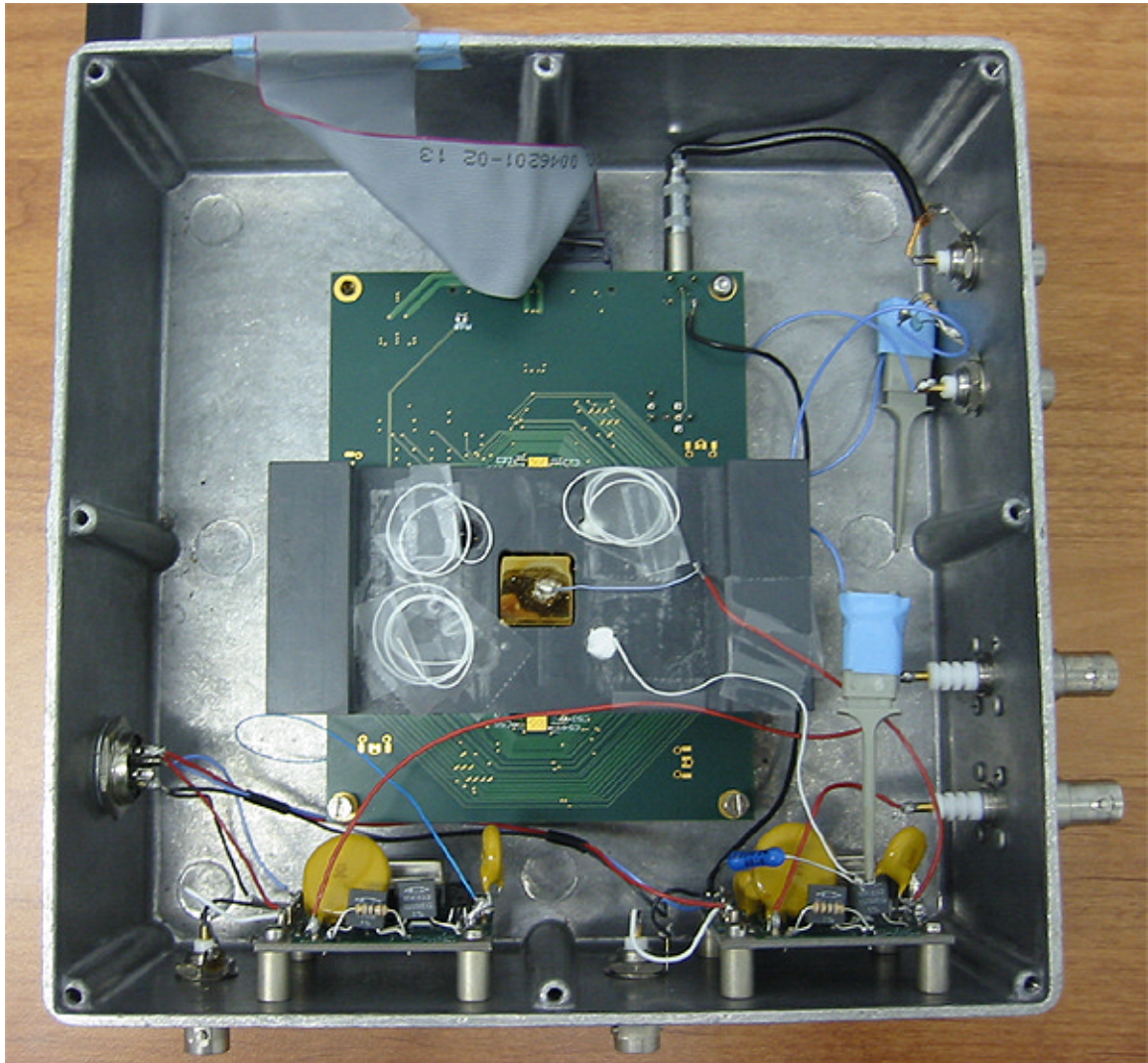
Figure 4.4. Detector mounted with the front-end board and placed inside an aluminum-housing box.
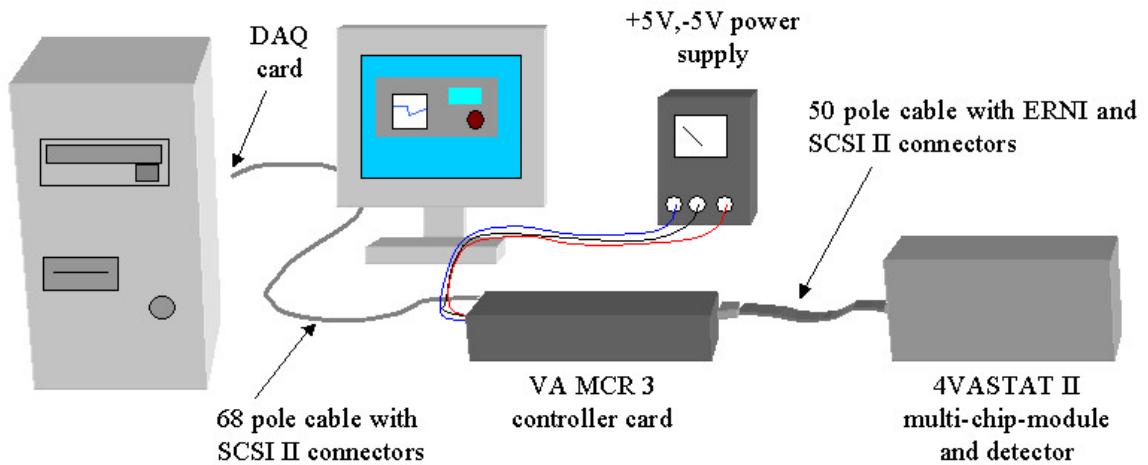
Figure 4.5. Basic system configuration.

4.1.4 Depth sensing using electron drift time

Figure 4.6 summarizes the basic concept of depth sensing using electron drift time for multiple-pixel events. When a gamma ray interacts inside the detector and the electron clouds start to drift, a trigger is generated by the TAT2 special channel when the induced signal on the cathode crosses a threshold. This trigger starts the TAC in the TAT2 special channel and generates the system trigger - C. When an electron cloud drifts near an anode pixel, the induced signal crosses a threshold, and triggers the corresponding TAT2 channel - a1. This trigger starts the TAC corresponding to that anode pixel channel. After a fixed delay ΔT after the system trigger, all the channels are read out in serial mode through a multiplexer built into the chips. By using peak-hold in addition to sample-hold circuits, the pulse amplitude of multiple-pixel events with different electron drift times (different peaking times) can be read correctly. The individual electron cloud drift times ($\Delta T - \Delta t_1$, $\Delta T - \Delta t_2$, …) can be retrieved from the timing signal generated by the TACs in the TAT2 channels.
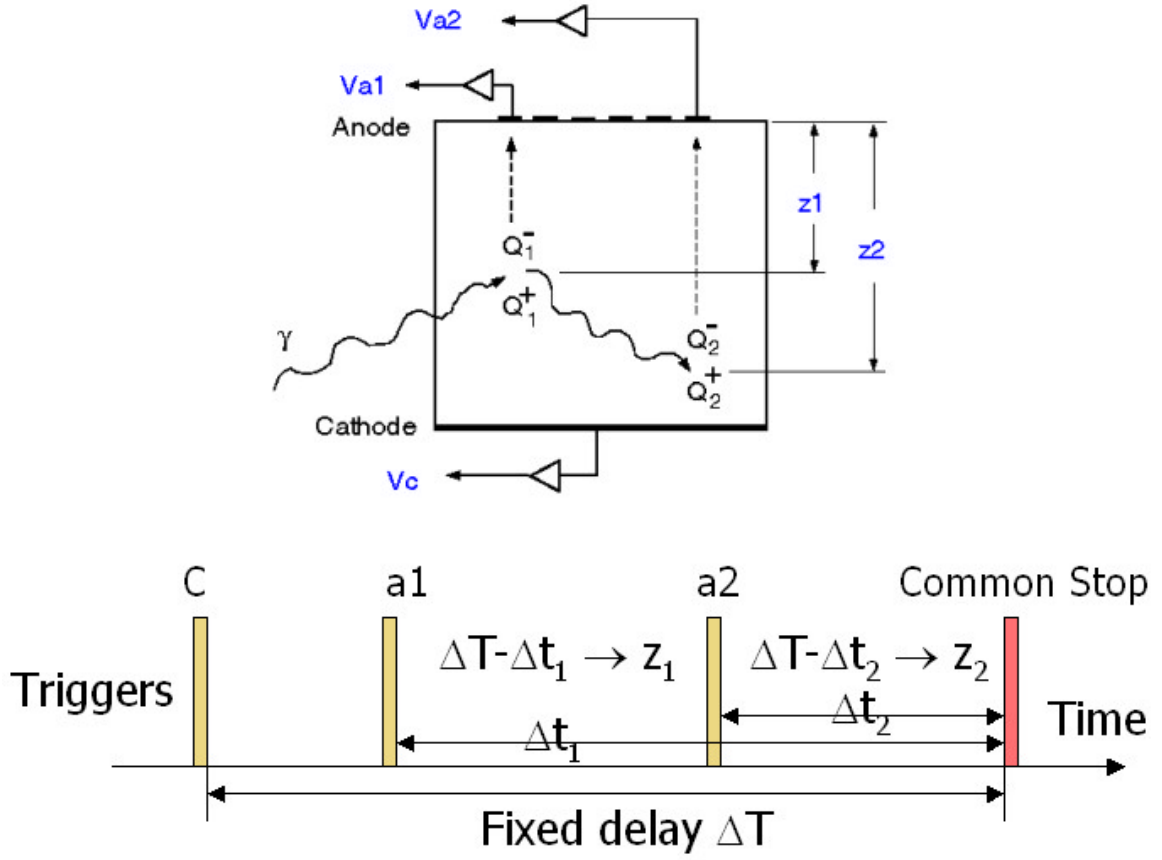
Figure 4.6. Interaction depth determination by electron drift time sensing. Va1, Va2 and Vc are the signals from two anode pixels and the cathode, respectively.

4.1.5 Working modes

The system can work in two readout modes: single-channel mode and serial readout mode. The single-channel mode is used for system testing. In this mode, the multiplexer is set so that one channel is constantly connected to the output and the test pulse generated by the DAQ board is injected into this channel. The output of this channel is read out continuously and the response of this channel, including voltage and timing response, to the test pulse can be monitored both in the DAQ program and on the oscilloscope. The serial read out mode is used to sequentially sample the output of all the channels by the multiplexer being automatically switched channel by channel by the

readout clock. Sparse readout mode is not available so it requires ~500 µs to read out the 128 channels. Thus the throughput is limited to ~2000 events per second.

4.1.6 Trigger and threshold

Two trigger modes can be chosen in the serial readout mode, the program trigger or the TA-trigger. The program trigger is generated by a general-purpose counter on the DAQ board. The system is then read out at a constant rate by programming the general-purpose counter. The TA-trigger is generated by the TAT2 chip. The discriminator outputs from the TAT2 channels are combined using "OR" logic to produce the TA-trigger. This is the mode used when serially reading events from the detector.

Ideally, the system should be triggered from the cathode side and the electron drift time could be derived from the time difference between the cathode trigger and the anode trigger. However, due to some layout design problems, there is large cross-talk on the cathode signal induced by the digital clock signals. A special add-on circuit was integrated into the system to reduce the cross-talk and suppress the induced triggering with this alteration. The cathode signal lowest threshold is limited to 110 keV by cross-talk induced triggering. The anode pixels have triggering thresholds ranging from 60 keV to 90 keV, with the spread caused by the variation of baseline levels and noise in each ASIC channel. For single-pixel events, the system can be triggered from either the cathode side or the anode side because the cathode to anode signal ratio (C/A ratio) can be used for depth sensing. For multiple-pixel events, the system has to be triggered from the cathode side. Each anode signal must also pass its threshold to register the electron drift time for its electron cloud. Since the cathode trigger signal is determined by the total energy deposition, while the anode trigger signals are determined by the smaller

individual energy depositions, the system threshold for multiple-pixel events is mainly limited by the anode threshold lower limit.

In the VAS2/TAT2 system, only a global threshold can be set for all the anode pixels. Thus, the global threshold has to be set above the highest threshold among all channels to avoid noise triggering.

4.1.7 Problems and solutions

4.1.7.1 Damage to the special channel

The first discouraging problem hindering the success of the VAS2/TAT2 system was the mysterious damage to the special channels. All four special channels stopped functioning after a period of operation. This is the reason why Wen Li had to use external discrete circuits to read out the cathode signal. This problem was observed again on other VAS2/TAT2 systems. However, the reason for this damage remained unclear. The most suspicious reason is the static charge. After paying the price of several more special channels, the rules of using the special channel and the cathode connection was finally established:

- Before soldering the special channel to the cathode, the special channel must first be connected to ground using a non-permanent connection such as a clip.

- While doing the soldering, it would be safer if the soldering iron were unplugged from the power supply and then touched to the ground (detector box) before doing the actual soldering.

- While soldering, the power supply of the ASIC should be ON so that the static charge, if any, can be dissipated.

- After the special channel has been connected to the cathode, if the ASIC power must be turned OFF for a time longer than one minute, the special channel must be connected to the ground (detector box) for protection.

After implementing the above rules in handling special channels, no damage has been observed ever since.

4.1.7.2 High cathode triggering threshold

After the damage problem in the special channels was solved, both the anode signal and the cathode signal could be safely read out through the ASIC for the first time. However, another serious problem was discovered. The differential digital signals on the front-end board were not properly routed. This resulted in very large pick-up noise on the cathode when the digital signal was sent to the ASIC, as can be seen from the preamplifier output (green) signal in Figure 4.7. During the read out, the HOLD signal will hold all channels and thus it will not affect reading out the true signals. However, after the readout is completed, a few more digital signals (RESET and READY) are sent to the ASIC. As a result, if the cathode triggering threshold is not high enough, the cross-talk signal induced on the cathode will cause a continuous re-triggering in the system, as shown in Figure 4.8. To prevent this re-triggering caused by the cross-talk, the cathode threshold had to be set unacceptably high (>500 keV). As discussed in Section 4.1.6, the system has to be triggered by the cathode signal first to properly do electron drift time sensing for multiple-pixel events. This 500 keV cathode threshold resulted in a significant efficiency loss. Something must be done to reduce the cross-talk and lower the cathode threshold.

The first thing we did is to add a thin copper plate between the front-end board and the cathode. However, if this copper plate was connected to the ground, there was very large oscillation in all the signals. If this plate was not connected to the ground, the shielding effect was very small and of little help.

Figure 4.7. Pulse waveforms from a VAS2/TAT2 system. Green: Special channel pre-amp buffered output. Magenta: Readout clocks. Purple: HOLD signal.
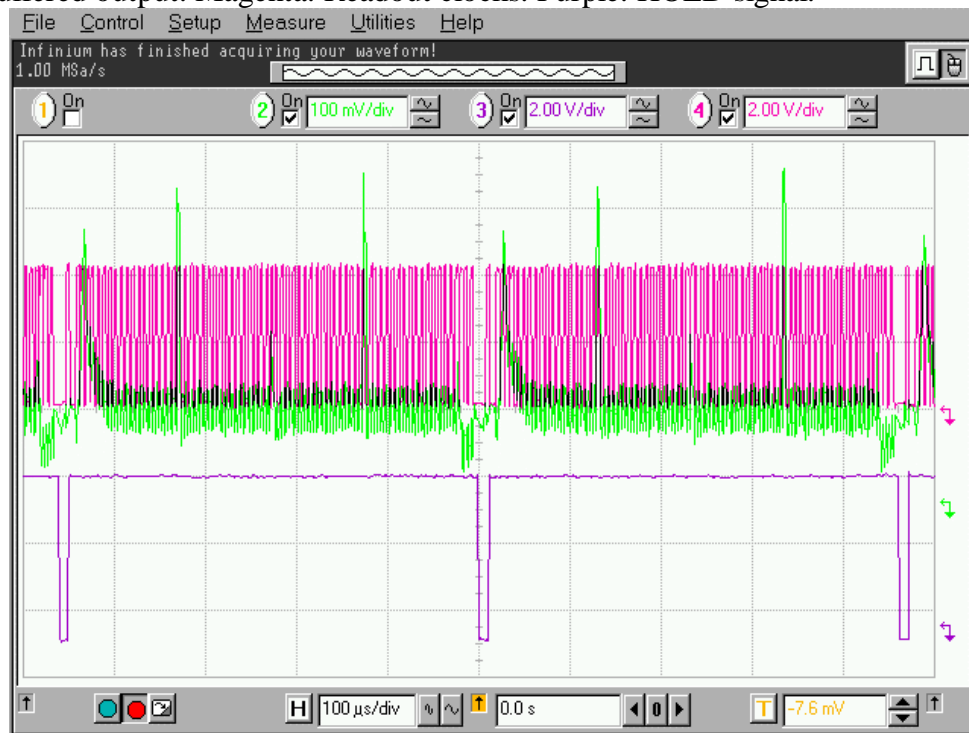
Figure 4.8. Re-triggering pulse waveforms from a VAS2/TAT2 system. Green: Special channel pre-amp buffered output. Magenta: Readout clocks. Purple: HOLD signal.

Since the cross-talk is due to the front-end board design and cannot be reduced without a redesign, we have to find a solution in the threshold itself. After some investigation, a simple special add-on circuit generating a varying cathode threshold was implemented in the system. It was discovered that the SHIFT_IN signal of the system jumped from 0V to and remained at +2V during the readout. Therefore, by carefully choosing the resistors of the circuit in Figure 4.9, the cathode threshold can be temporarily raised to a sufficiently high level to prevent re-triggering during the readout and returned to the normal level after a delay when the readout is completed, as shown by the waveforms in Figure 4.10. This modification successfully lowered the cathode threshold from ~500 keV to ~110 keV.
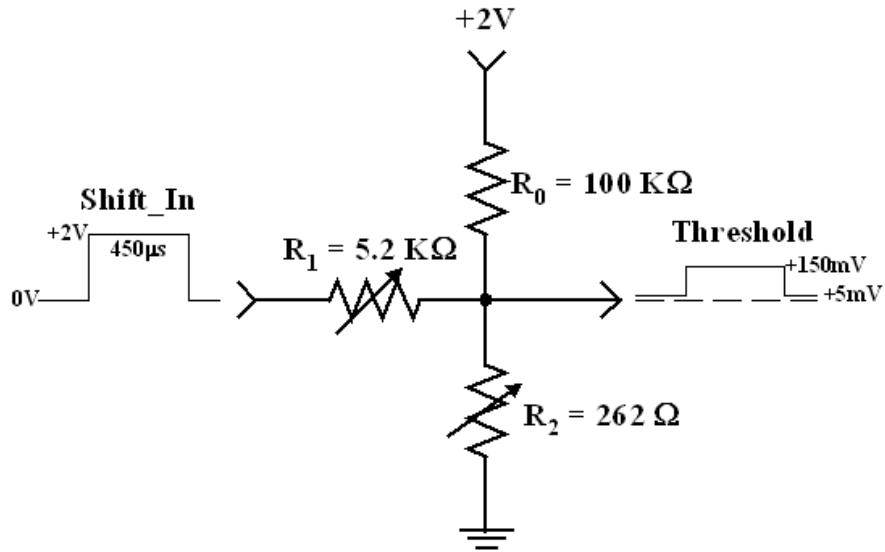
Figure 4.9. Circuitry used for varying cathode threshold.
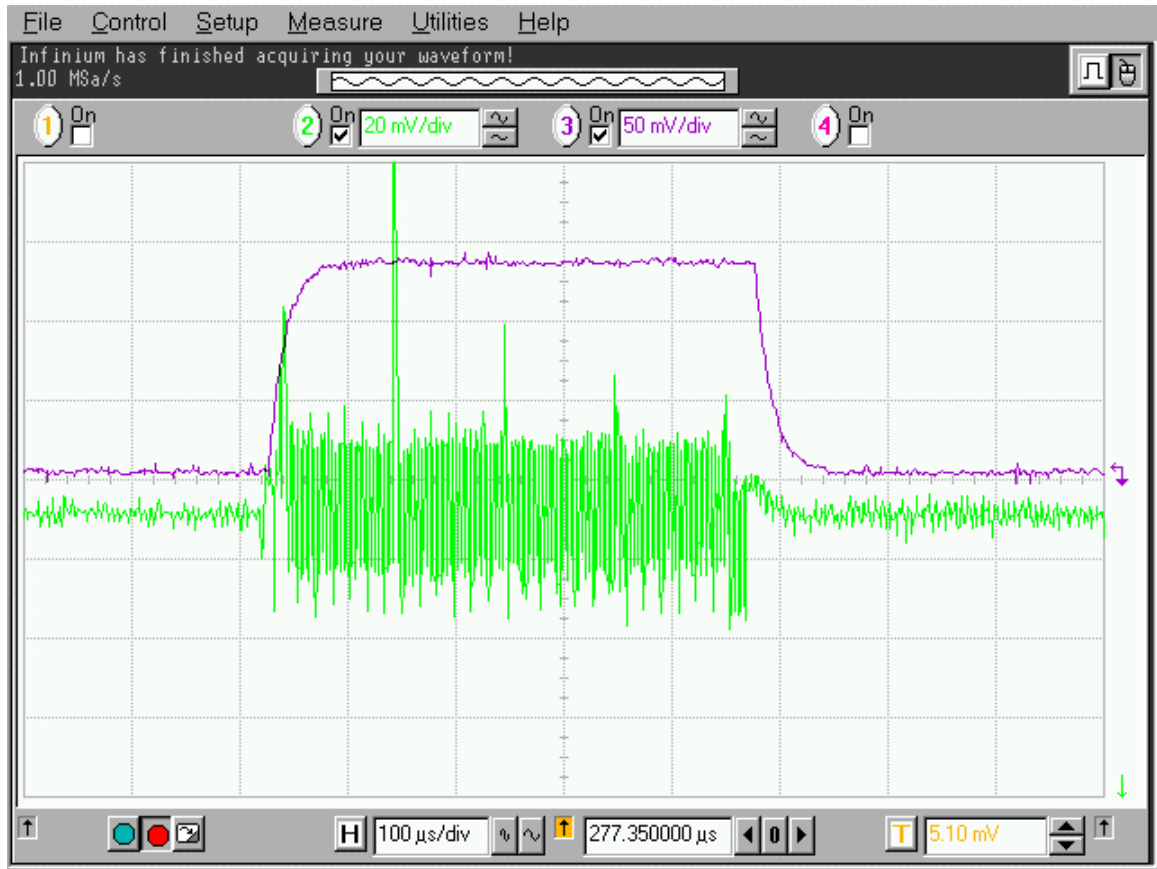
Figure 4.10. Pulse waveforms from a VAS2/TAT2 system. Green: Special channel pre-amp buffered output. Purple: Cathode threshold.

4.1.7.3 High cathode low energy threshold

Another problem caused by the cross-talk noise is the low energy threshold of the cathode signal. Although the re-triggering problem has been solved by raising the cathode threshold during the readout period, the cross-talk on the cathode after the RESET signal will cause residual signal on the peak-hold circuitry in the special channel. This residual signal is ~200 keV. Thus, although the triggering threshold is close to 100 keV, the signal smaller than 200 keV will have the same amplitude. As a result, the lowest cathode signal the system can correctly register is 200 keV when interactions

occur at the cathode side and even higher at the anode side, as can be seen from the cathode spectra in Figure 4.11.
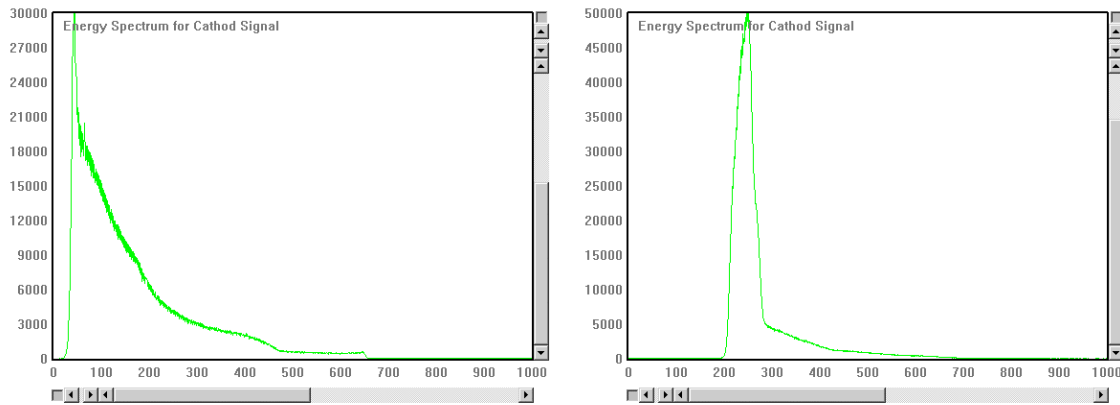
Figure 4.11. Cathode spectrum for a ^{137}Cs source. Left: Normal cathode spectrum. Right: High cathode low energy threshold (~200 keV) caused by the crosstalk.

After extensive investigation, the cause of this problem was found to be the READY signal after the RESET. This READY signal was on the same signal wire as the HOLD signal and following the HOLD signal after a delay. Since the HOLD_B signal had the same amplitude as, but the opposite polarity to, the HOLD signal, the problem could be solved by introducing a counter-cross-talk from the HOLD_B signal to compensate the cross-talk caused by the HOLD signal. Therefore, a short thin wire was connected to the HOLD_B signal, as illustrated in Figure 4.12. By carefully adjusting the position and orientation of this wire, the cross-talk on the cathode signal was successfully reduced by compensation, as shown in Figure 4.13. After this compensation, the low energy threshold of the cathode signal was reduced to ~30 keV.
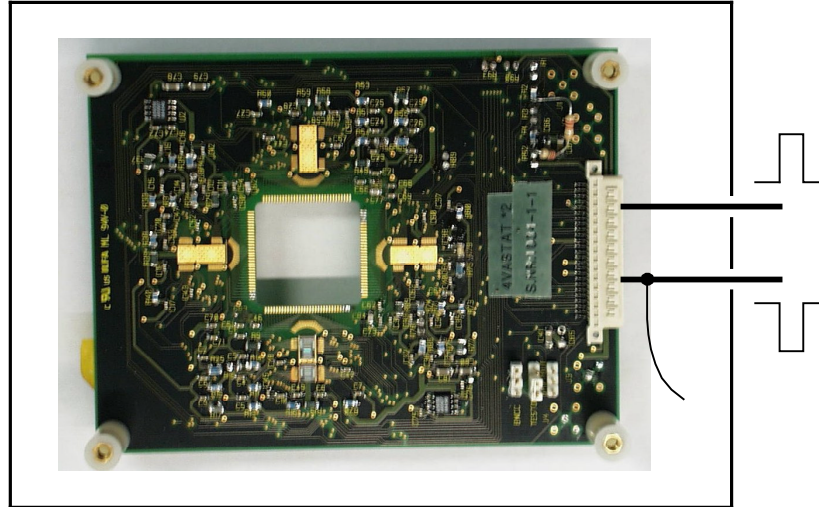
Figure 4.12. Compensating the cross-talk.
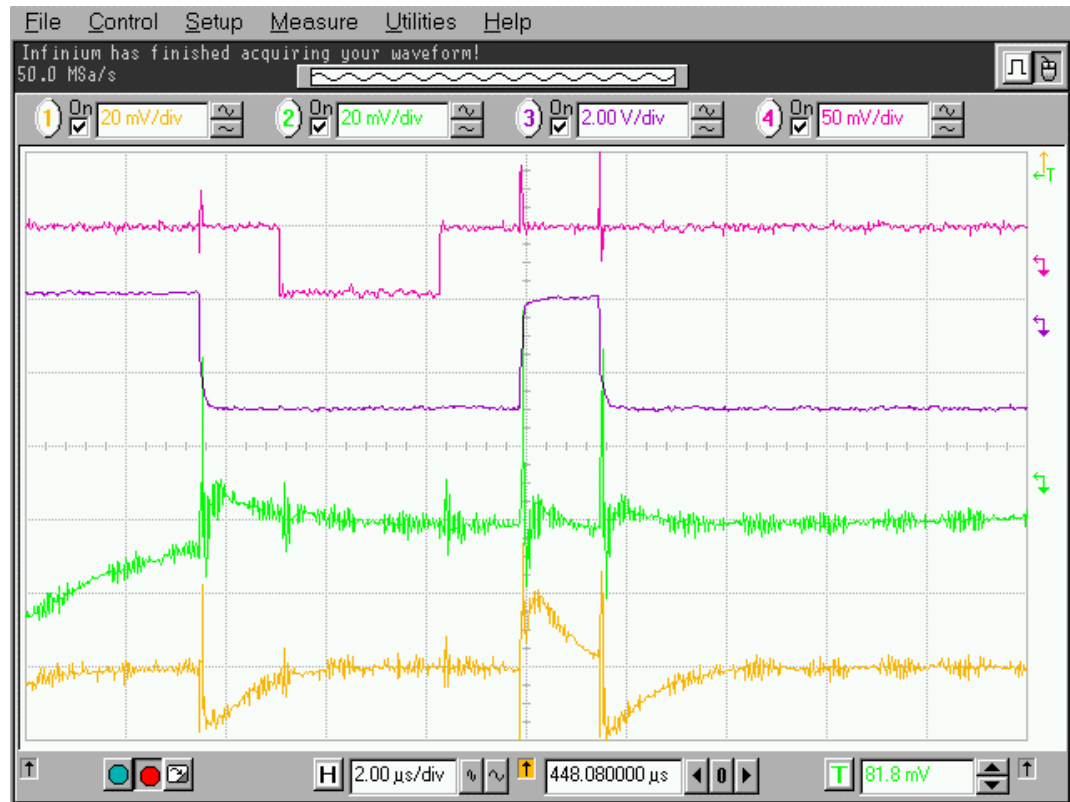
Figure 4.13. Cross-talk compensation waveforms from a VAS2/TAT2 system. Green: Special channel pre-amp buffered output. Magenta: RESET signal. Purple: HOLD&READY signal. Yellow: Compensating signal introduced from the opposite cross-talk of the HOLD_B signal.

After all the problems discussed above were solved, both the anode and the cathode signal were read out through the ASIC without any problem. The VAS2/TAT2 system was fully functional for the first time and had achieved good spectroscopic performance, which will be discussed in Chapter 6.

4.2 VAS3/TAT3 System

4.2.1 Modifications and Enhancements

Although the VAS2/TAT2 system was fully functional, there were still several unsolved problems degrading the system performance, such as the fairly high electronic noise, the large cross-talk, the high triggering thresholds and the large temperature drift of the baseline and gain. Before heading for the next-generation 3-D CdZnTe array system, we needed to do another design iteration to verify that all problems could be solved and better performance could be achieved. Therefore, the VAS3/TAT3 system was developed.

The modifications in the VAS3/TAT3 system are listed as follows:

п   One additional normal channel was added to the VAS3 ASIC, totaling one special channel and 32 normal channels on one chip. A digital bit is used to control the polarity of all the channels so that the chip can also be used to read out the positive charge pulses, such as the cathode signal of a silicon detector.

п   A 4-bit digital to analog converter (DAC) was implemented in each TAT3 channel, so that the threshold of each channel can be fine tuned in addition to the global threshold. The principle of this DAC threshold is shown in Figure

4.14 and the effect of trimming the threshold is shown in Figure 4.15. In addition, the electronic noise in the TAT channel was also reduced.

n Both the linearity and the dynamic range of the VAS channel were improved.

n The ASIC front-end board and the MCR3 controller board were also redesigned to reduce the digital signal pickup noise and the electronic noise.
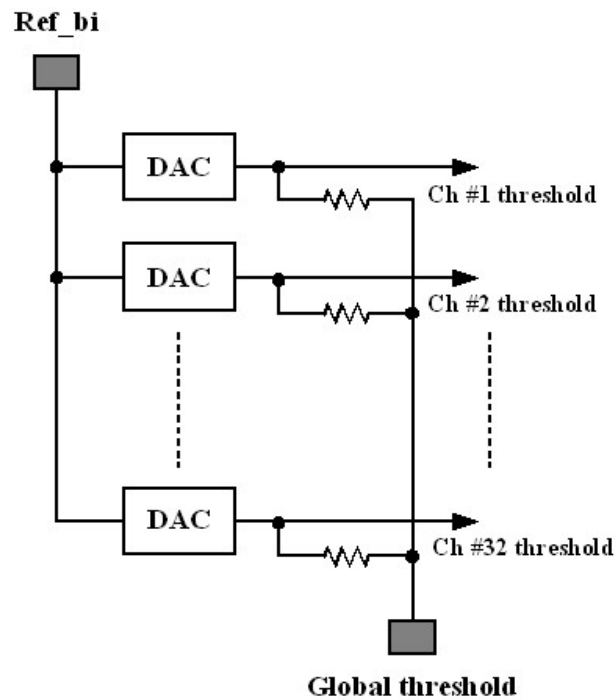
Figure 4.14. Functional principle of the trim-DAC threshold circuits in a TAT3 ASIC chip.
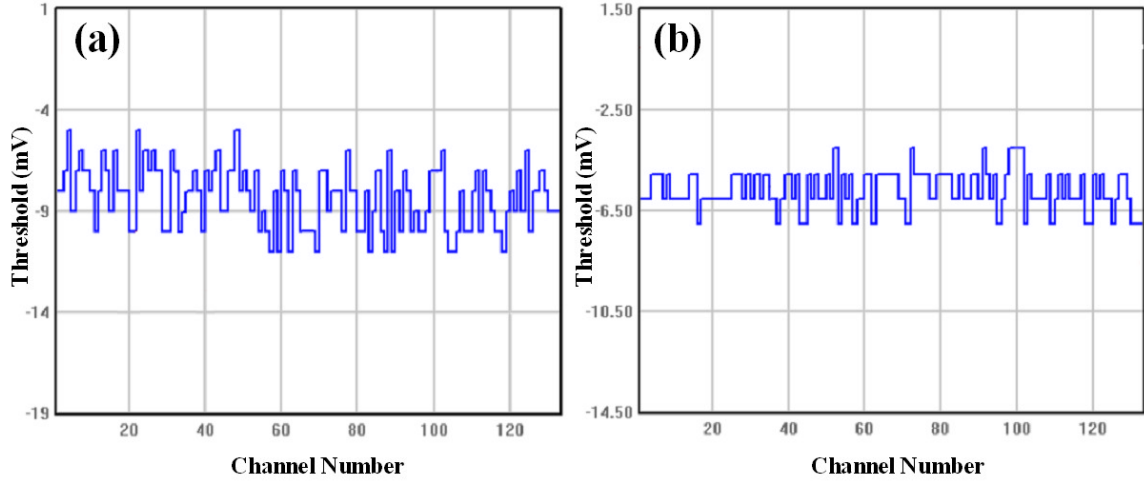
Figure 4.15. Effect of the trim-DAC threshold in the VAS3/TAT3 system. (a) Thresholds of all channels before applying the trim-DAC adjustments. (b) Thresholds of all channels after applying the trim-DAC adjustments.

4.2.2 Problems

Several problems were found in the VAS3/TAT3 system. Firstly, the shaper in the VAS channel was unstable. The leading edge of the shape output waveform had strange ripple shapes, as shown in Figure 4.16. Secondly, all channels had fairly large baseline offsets and the variation in this offset is quite large from channel to channel, as can be seen in Figure 4.17. Although the baseline offsets are expected and can be corrected in calibration, the large variations in these offsets may indicate potential problems in the system. Thirdly, the electronic noise was still similar to the VAS2 system. As a result, the energy resolution for single-pixel events was similar to that of the VAS2/TAT2 system. But the energy resolution for multiple-pixel events was much worse than that of the VAS2/TAT2 system. Fourthly, although the gain of the normal channels was fairly stable comparing to the VAS2/TAT2 system, the baseline still had large temperature drift. Lastly, the linearity of special channels was good, similar to the VAS2/TAT2 system. The overall linearity of normal channels also looked ok. But there is some small-scale

curvature shape in the linear relation. This might be the reason for the much worse than expected energy resolution for multiple-pixel events.

It was later found that most of the above problems were due to a design fault in the VAS3 ASIC. Therefore additional ASIC design iteration was carried out to address these problems.
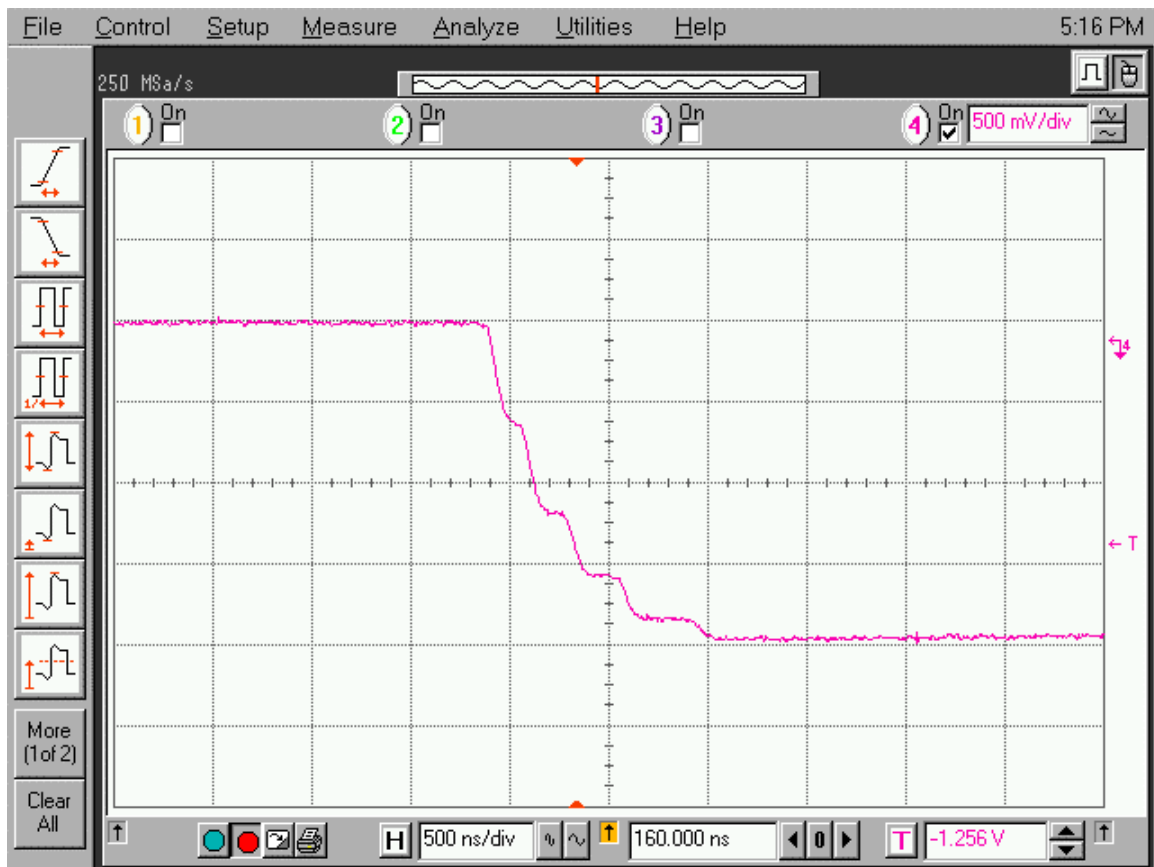
Figure 4.16. Waveform of the VAS3 single channel output. This is the waveform after the peak-hold circuit. Therefore, only the leading edge of the shaper output can be observed.
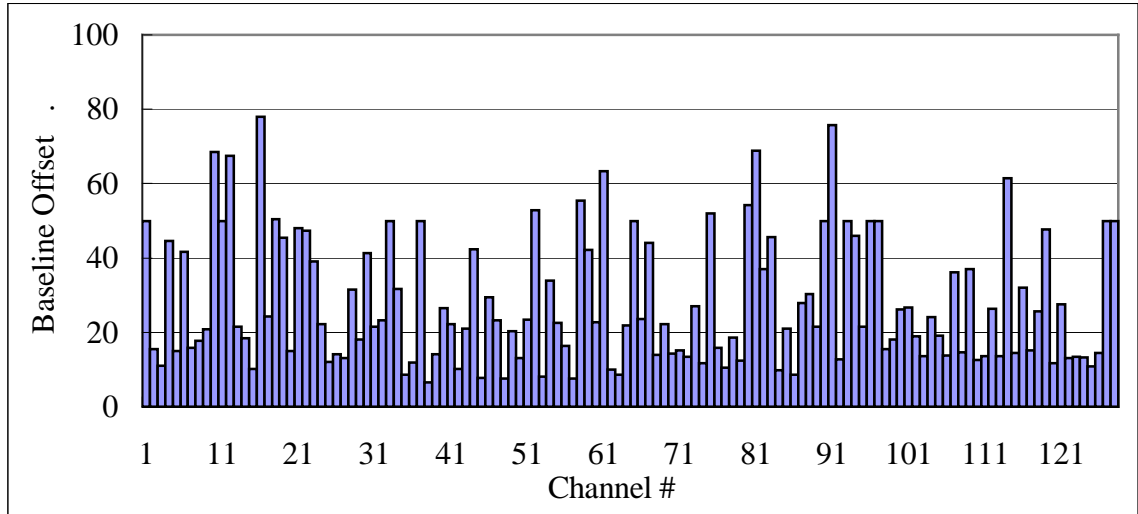
Figure 4.17. Variation of baseline offsets in a VAS3/TAT3 system.

4.3 VAS3.1/TAT3 System

In the VAS3.1/TAT3 system, the TAT3 ASIC was unchanged. But the VAS3 ASIC was re-designed as the VAS3.1 ASIC. There are several important modifications:

- п The inverter, which was used following the shaper to invert the polarity of the anode signal, was removed. Instead, a peak-hold circuit with selectable polarity (shown in Figure 4.18) was implemented. As a result, the shaper output waveform no longer has the ripple shape and the baseline of the VAS output is fairly insensitive to the temperature change.

- п An additional channel has been added to the VAS3.1 ASIC chip. This channel doesn't have a peak-hold circuit. Thus, we can directly observe the shaper output of the VAS channel in the single channel mode, and we can adjust the ASIC bias current settings to obtain the best pulse shape and the best signal to noise ratio.

- п The electronic noise was greatly reduced. Ideas ASA reported an electronic noise of ~3 keV FWHM in the ASIC alone. With the detector connected to

69

the ASIC, we measured the electronic noise to be no larger than ~4.5 keV
FWHM in the normal channels and ~7 keV FWHM in the special channel.

n   The front-end board was carefully examined and modified so that the cross-
    talk noise was further reduced. As a result, the triggering threshold has been
    lowered to <30 keV on the anode pixels and <60 keV on the cathode.

Thanks to all these efforts, significant improvements in spectroscopic
performance have been achieved in the VAS3.1/TAT3 system, detailing in Chapter 6.
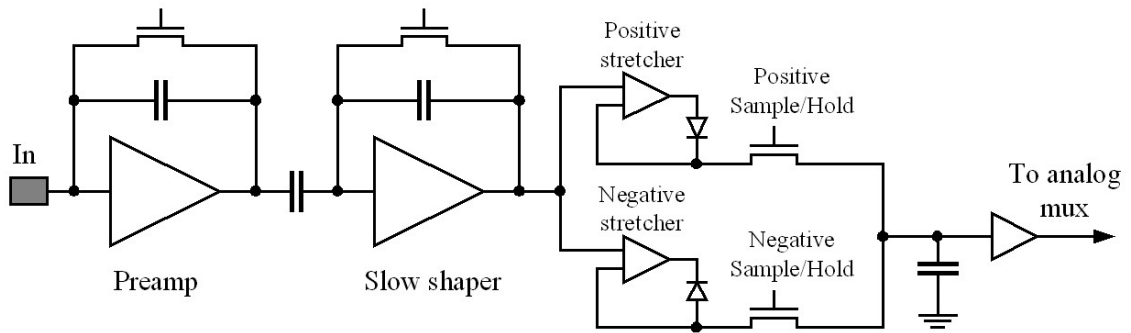
Figure 4.18. Functional principle of the peak-hold circuits with selectable polarity [78].

4.4 Software

4.4.1 Data acquisition program

Along with the hardware, Ideas ASA also provided a data acquisition program
written in Labview. Besides quite a few bugs, the program was also pretty slow and
inefficient in data processing. Therefore, after extensive study of how the program works
to control the hardware system, a replacement program was developed in Visual C++.
The program can do not only data acquisition, but also data pre-processing and
compression.

Due to the size of the raw data (~1 GB/h), data compression must be performed on the fly. There are two types of data compression levels available. The first level is loss less but only has a compression ratio of ~3:1, while the second level discards data from channels without true signal and has a compression ratio of ~40:1.

4.4.1.1 Lossless compression

For each event, there are two sets of 128 ADC values for the VAS channels and the TAT channels, respectively. Each ADC value is 16 bits, in which only the lower 12 bits are useful since it's a 12-bit ADC. However, for each event, only a few channels have true signal, while the signals of other channels are basically only noise. For every 1000 events, if we bin the value of each channel into the corresponding spectrum, the spectrum should have a peak at the baseline position of this channel and only a few counts corresponding to true signals are outside this peak. The centroid of the peak can be used as the baseline of the corresponding channel. By subtracting the ADC value of each channel from its baseline value, most channels will have a very small net value in the range of ± 7, and can be represented in only 4 bits. Thus, we only need to record 4 bits of data per channel for most channels, instead of 16 bits. This results in the compressed data size of around one third of the size of the raw data without any information loss.

4.4.1.2 Zero-suppressing compression

The second compression method is based on the first one. Instead of recording the value for all channels, this method only records the values larger than a pre-determined threshold value and the corresponding channel numbers. This results in a huge reduction in the data size and achieves a compression ratio of ~40:1.

After the calibration and with the calibration parameters loaded, the program can act as a real-time spectroscopy program. The deposited energy and the 3D position

information for each event can either be stored to files for post-processing (such as Compton imaging) or sent to another computer over the internet for real-time imaging.

4.4.2 Data processing program

After being collected from the detector system, the raw data must be processed to get the calibration parameters. Originally, Wen Li wrote some separate Matlab codes to process the data. However, these codes are hard to maintain and fairly slow. What's more, the huge size of the raw data makes it very difficult to manage. Therefore, an extensive data processing program has been developed in Visual C++ to do all the data processing and management.

CHAPTER 5

CALIBRATIONS AND EVENTS RECONSTRUCTION

Because of the variations and non-uniformity in both the detector response and the electronics several calibration steps must be carried out, such as the channel to channel gain variation, the baseline offset and non-linearity in each channel, the baseline and gain drift in each channel, the depth dependence of the charge collection efficiency (including the weighting potential effect and the electron trapping effect), the electron drift time vs. the depth, the timing-amplitude-walk, and the weighting potential cross-talk in multiple-pixel events. Before these corrections the collected anode spectra have very poor energy resolution. The calibration procedures are described one by one in the following sections, and the effects of the calibrations are also demonstrated step by step. Due to the improved design from the VAS2/TAT2 system to the VAS3.1/TAT3 system, some calibrations necessary in the VAS2/TAT2 system are no longer needed in the VAS3.1/TAT3 system. Flow charts summarizing the calibration and events reconstruction procedures for both systems are presented at the end of this chapter.

5.1 Single-Pixel Events

5.1.1 Baseline detection

In current 3-D CZT systems, the 128-channel VAS and TAT signals have not had the baseline subtracted. So, the baseline is not at zero or a fixed value and varies from

channel to channel, as can be seen in Figure 5.1. Furthermore, the baseline can drift with temperature. The baseline of each channel must be detected and monitored for any drift.
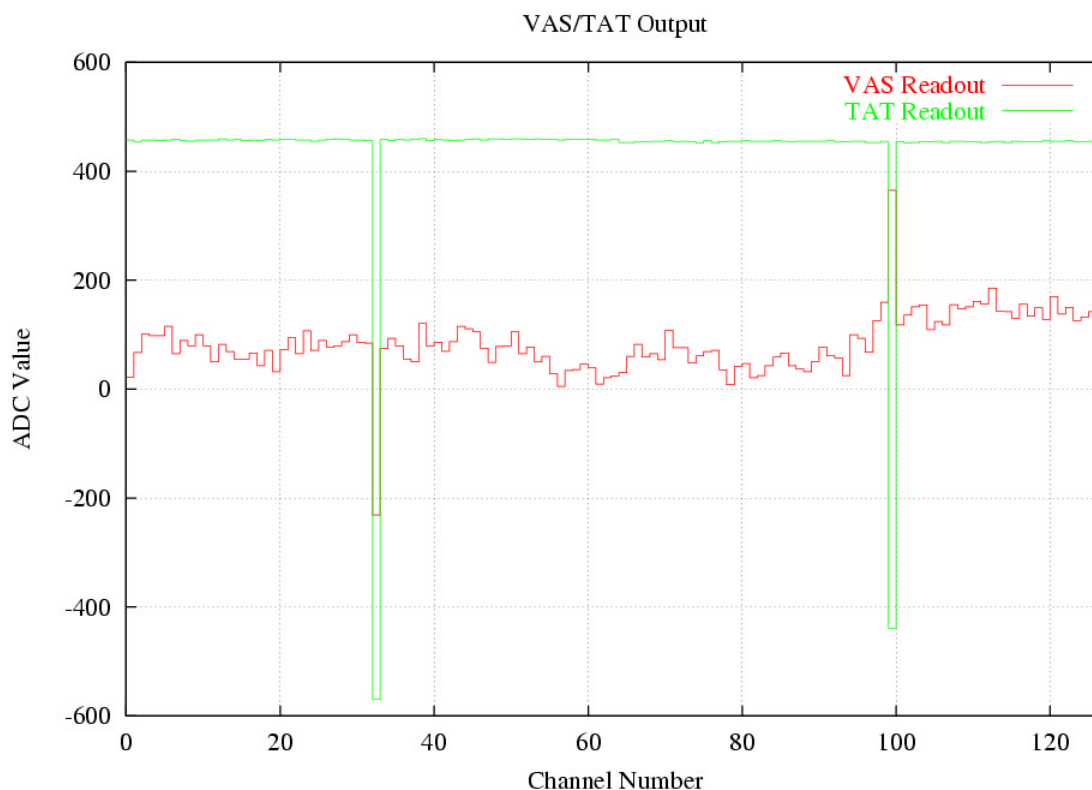
Figure 5.1. Output of the 128 VAS/TAT channels in serial readout mode for one typical single-pixel event. Channel #32 is the special channel used to read out the cathode signal.

In normal working mode all channels are readout serially, no matter which channels are actually triggered. Therefore, for each trigger (event) only a few channels have true signals, while other channels are fluctuating around their respective baselines. If for a certain number of triggers the signal from each channel was recorded into a spectrum for this channel, the spectrum should have a peak around the baseline of this channel with only a few counts outside the peak corresponding to true signals, as can be seen in Figure 5.2(a). The peak centroid can be used as the baseline of the corresponding

74

channel. In this way, we can dynamically detect and monitor the baseline of the normal channels (anode pixels). The net signal from each channel will be

$$S(n) = |V(n) - B(n)| \qquad (5.1)$$

where n is the channel number, V is the raw signal, B is the baseline and S is the net signal.

For the special channel (cathode signal), because the cathode will always have real signal, the spectrum described above for this special channel will not have a peak but rather a cutoff at the baseline, as shown in Figure 5.2(b). It is not reliable to detect the baseline of the special channel in the same way as the normal channels. So, for the special channel another unused special channel was chosen as a baseline reference because the special channels have relatively stable offsets with each other. The special channel used as the reference may also need to be grounded to prevent the influence of the cross-talk noise.

In the future, the ASIC may be designed to only output the net signal with the baseline subtracted. This on-chip baseline subtraction is also necessary for sparse-readout mode.

5.1.2 Common mode noise correction

By calculating the correlation matrix of the baseline fluctuations using Equation 2.23 for all 128 channels, common mode noise was discovered in the VAS2/TAT2 systems, as shown in Figure 5.3(a). The basic idea of the common mode noise correction is described as follows.

For each event all the channels are read out. Firstly, those channels with a net (baseline subtracted) signal larger than a certain threshold (e.g. 2 times the FWHM of the baseline fluctuation) are excluded. Secondly, the common mode noise is calculated by

adding the net signal from all remaining channels and dividing the sum by the total number of the remaining channels. Finally, this common mode noise is subtracted and the net signal is recalculated for each channel. The process can be summarized as

$$c = \frac{\sum_N S(n)}{N} \tag{5.2}$$

$$S'(n) = S(n) - c \tag{5.3}$$

where N is the number of channels whose net signal S is smaller than a given threshold, c represents the calculated common mode noise and S' is the net signal with the common mode noise subtracted.

Such common mode noise correction reduced the baseline fluctuation in all the channels and eventually improved the energy resolution of the VAS2/TAT2 system.

No common mode noise was observed in the VAS3.1/TAT3 system, as can be seen from Figure 5.3(b). This may be due to the greatly reduced cross-talk noise in the VAS3.1/TAT3 system.

5.1.3 Gain-temperature drift and gain-channel variation correction

It is pretty normal for ASIC to have gain variation among all channels, and the gain may also drift with temperature. Unlike the VA1 chips, the baseline and gain of VAS2 channels have significant sensitivity to temperature changes. The baseline drift can be monitored in real time and subtracted during the data acquisition. By dividing the collected data into subsets of ~1 hour period and finding out the gain and average baseline for each subset, the gain drift was found to have a monotonic relation with the VAS2 channel baseline position, as shown in Figure 5.4. Thus the gain variation can be corrected by monitoring the baseline shift in real time and using this relationship. The gain drift and variation correction can be expressed as

Typical VAS output signal amplitude spectrum for 1000 triggers (events) - ANODE channel

(a)

Typical VAS output signal amplitude spectrum for 1000 triggers (events) - CATHODE channel

(b)
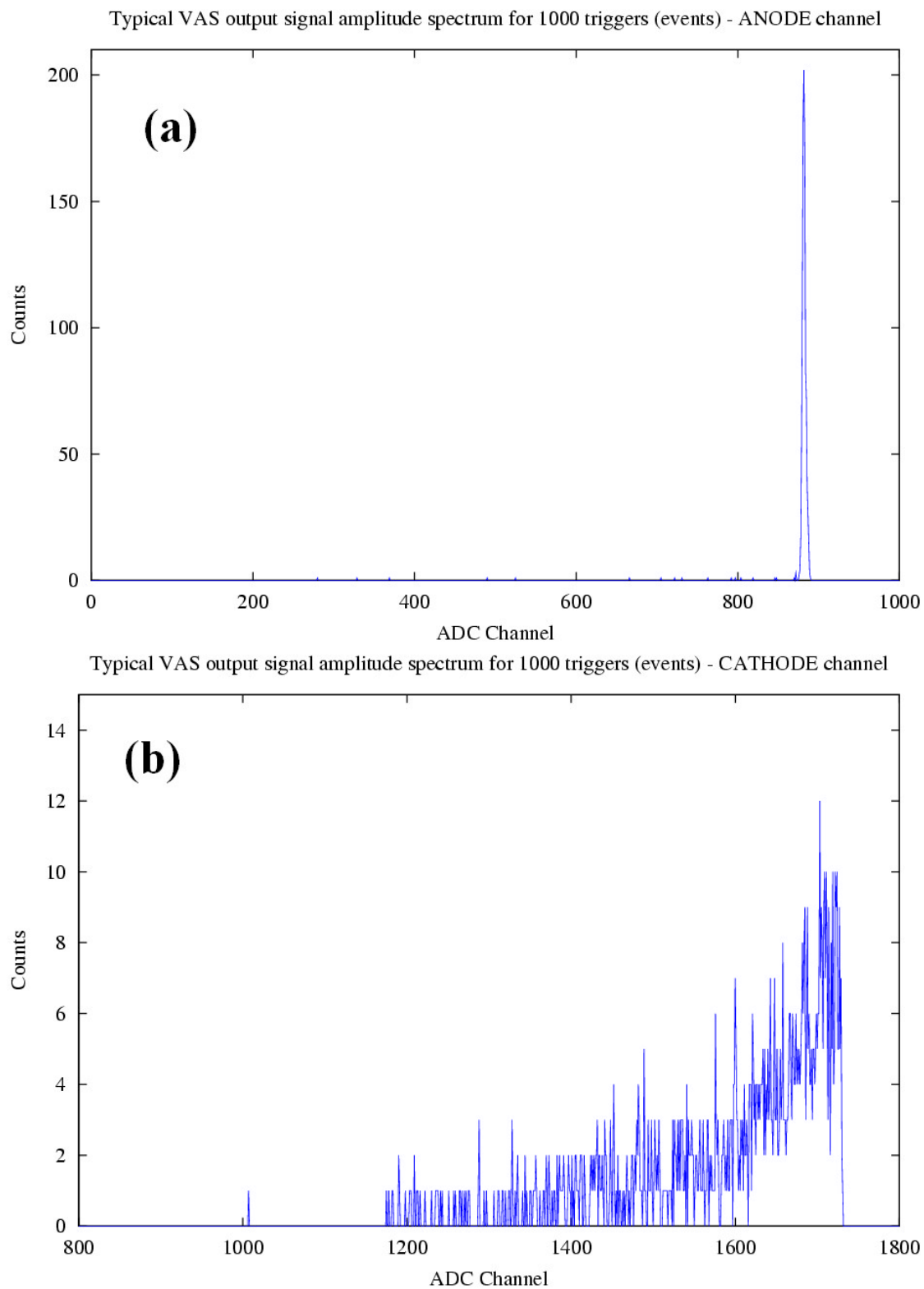
Figure 5.2. Typical VAS output amplitude spectra for (a) an anode pixel and (b) the cathode.
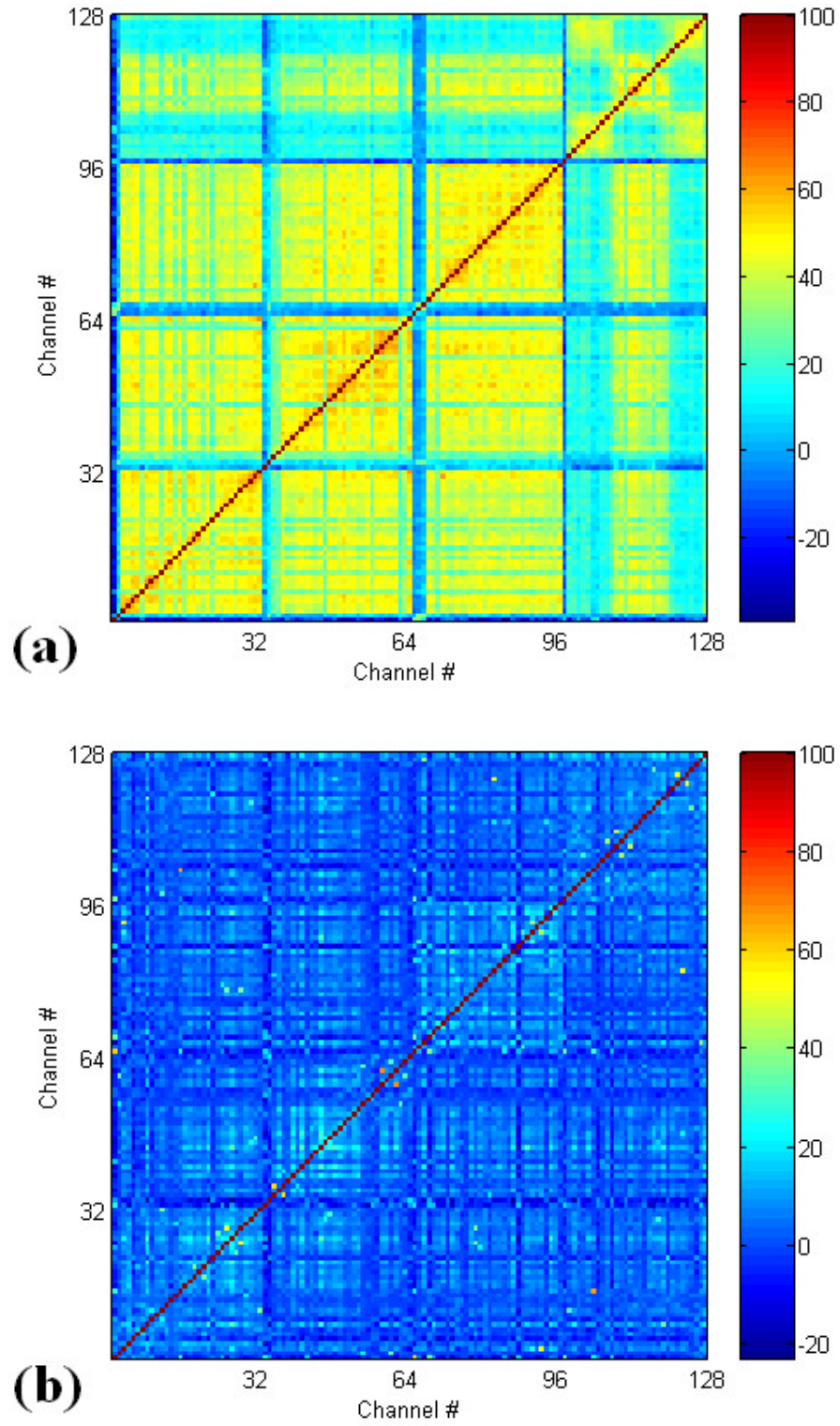
Figure 5.3. Correlation matrix of the baseline fluctuation for all 128 channels. (a) VAS2/TAT2 system. (b) VAS3.1/TAT3 system.

$$S'(n) = \frac{S(n)}{g(n, B(n))} \qquad (5.4)$$

where g is the gain correction coefficients obtained through the calibration. The effect of this correction can be clearly seen in Figure 5.5.

Before the depth correction, the anode spectrum has a broadened "photopeak" (let's call it photo-continuum) due to the varying electron trapping for interactions at different depths (cf. Figure 5.5). The gain variation among channels can be calibrated by detecting the high-end edge of the photo-continuum in the anode spectrum, because the events at the high-end edge of the photo-continuum should all be full energy deposit events occurring near the anode and having virtually the same percentage of electron trapping and the same amount of electrons collected by the anode pixel. The high-end edge is used for gain calibration because it is much sharper than the low-end edge and hence can be reliably detected by the program. Most of the events at the low-end edge of the photo-continuum are full energy deposit events occurring near the cathode and having maximum electron trapping. If there are some defects not very close to the anode, the events on the cathode side will always be affected, while the events on the anode side will not be affected.
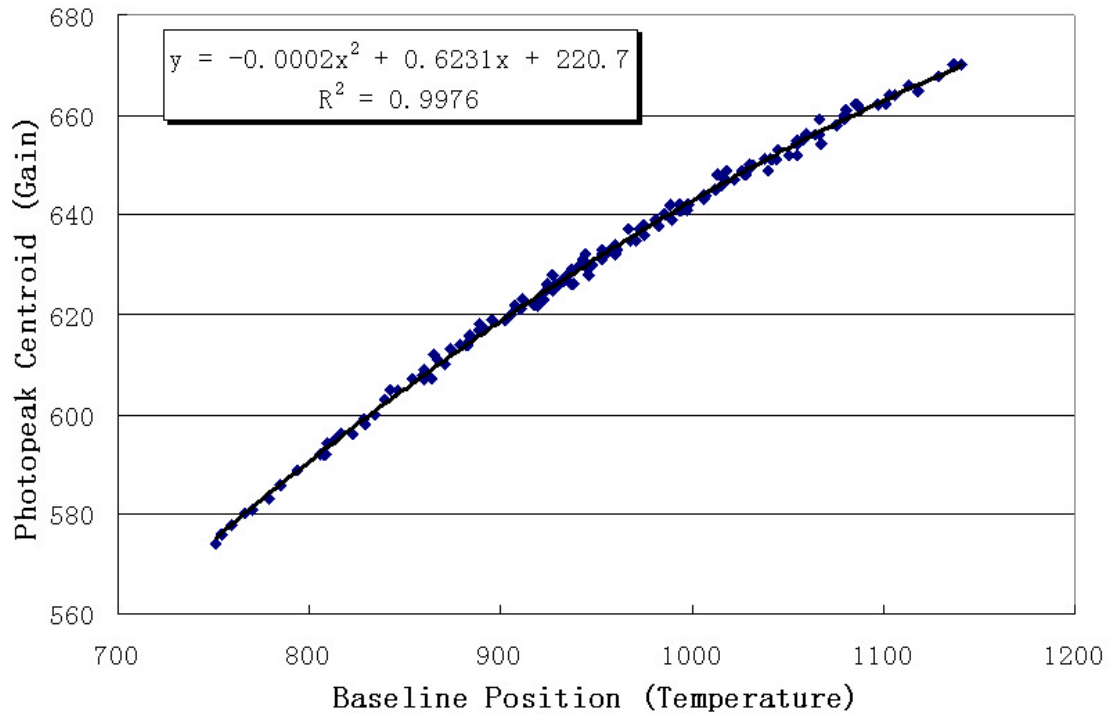
Figure 5.4. Correlation of photopeak position (gain) vs. baseline position (temperature) over a 40-hour measurement. The temperature range is $21^{\circ}C$ -$26^{\circ}C$.

If the gain drift is significant like in VAS2, the high-end edge of the photo-continuum can be used for gain calibration, and the relation between this drift and the temperature (the baseline position) can be used to correct for the gain drift. However, in the VAS3.1/TAT3 system, the gain drift is very small but not negligible. The high-end edge of the photo-continuum can no longer be used because the detection of the edge is relatively unreliable comparing with the very small drift in the gain. Alternatively, depth sensing and correction has to be done first and the drift of the photopeak centroid can be reliably detected to calibrate the gain drift. Since the gain drift is small, although this calibration relation was obtained after depth correction, it was proven that there was no problem to use it back before the depth correction.

Currently, the baseline position drifts with the temperature and can be used as a measurement of the temperature. If the baseline of future systems is no longer sensitive to temperature changes but the gain still drifts with the temperature, we have to use other methods to measure the temperature and correct for the gain drift.
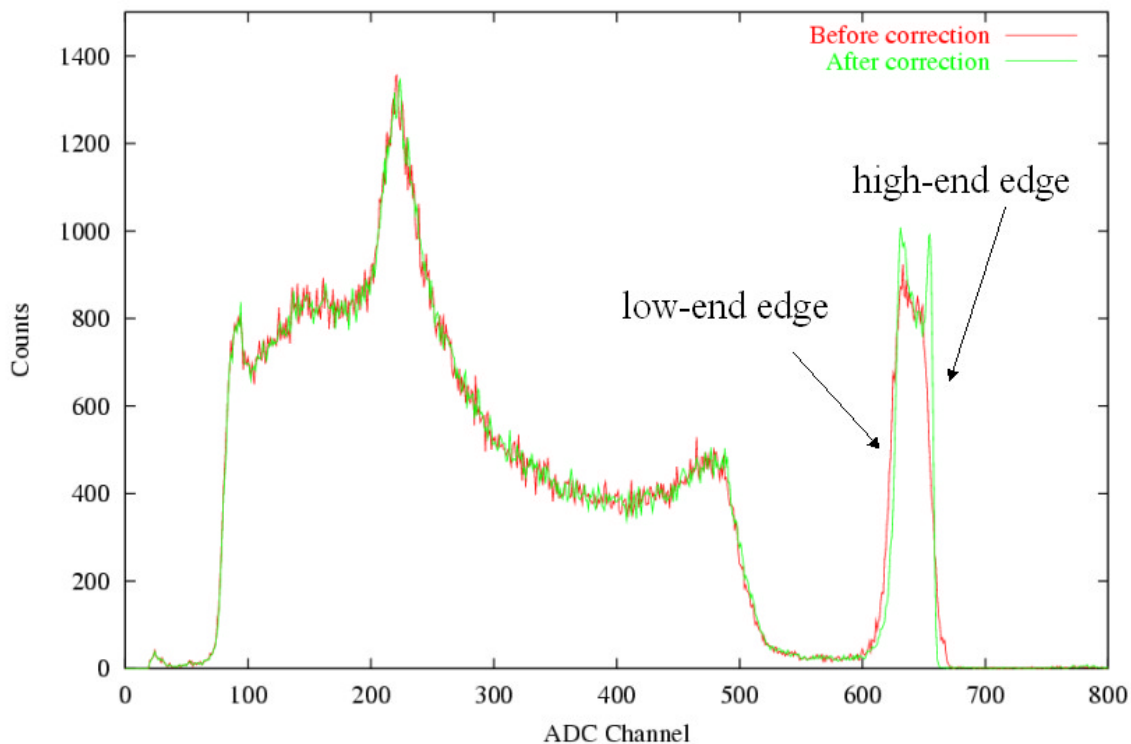
Figure 5.5. Raw spectra (before depth correction) for single-pixel events before (red) and after (green) gain-temperature drift correction.

5.1.4 Baseline offsets correction

It has been found that the VAS3.1 output signals have baseline offsets (or 0-channel offsets). The calibration of these baseline offsets can be done in two ways. If the linearity is good, a two-point calibration with a low gamma-ray energy (81 keV) and a high gamma-ray energy (662 keV) can be used to calibrate the baseline offset for each channel. If the linearity is not good, the baseline offset can be treated as part of the non-linearity and is taken care of in the non-linearity calibration described in Section 5.1.6.

81

Because the VAS3.1 has good linearity, [133]Ba (81 keV) and [137]Cs (662 keV) were chosen for the calibration. The 81 keV photons only interact in a thin layer near the cathode. Therefore the 81 keV photopeak events can be regarded as all from the depth index very near the cathode side. The photopeak centroids were then determined for all the channels as $P(n, 81)$. The 662 keV photopeak events occurring near the cathode were selected using the C/A ratio and the photopeak centroids were determined for all the channels as $P(n, 662)$.

Since the 81 keV and 662 keV photopeak events occurring near the cathode should have the same percentage of electron trapping, by assuming a linear relation between the VAS output and energy, the baseline offset can be determined as

$$o(n) = \frac{662 \times P(n, 81) - 81 \times P(n, 662)}{662 - 81} \tag{5.5}$$

$$S'(n) = S(n) - o(n) \tag{5.6}$$

where n is the channel number, o is the calculated baseline offset and S' is the net signal after the baseline offset correction.

By using the method described above, the baseline offsets for all channels were corrected and codes have been developed to do the correction automatically. Figure 5.6 shows the overall raw spectrum before and after the baseline offset correction. The improvement can be clearly seen in the spectrum after the baseline offset was corrected.
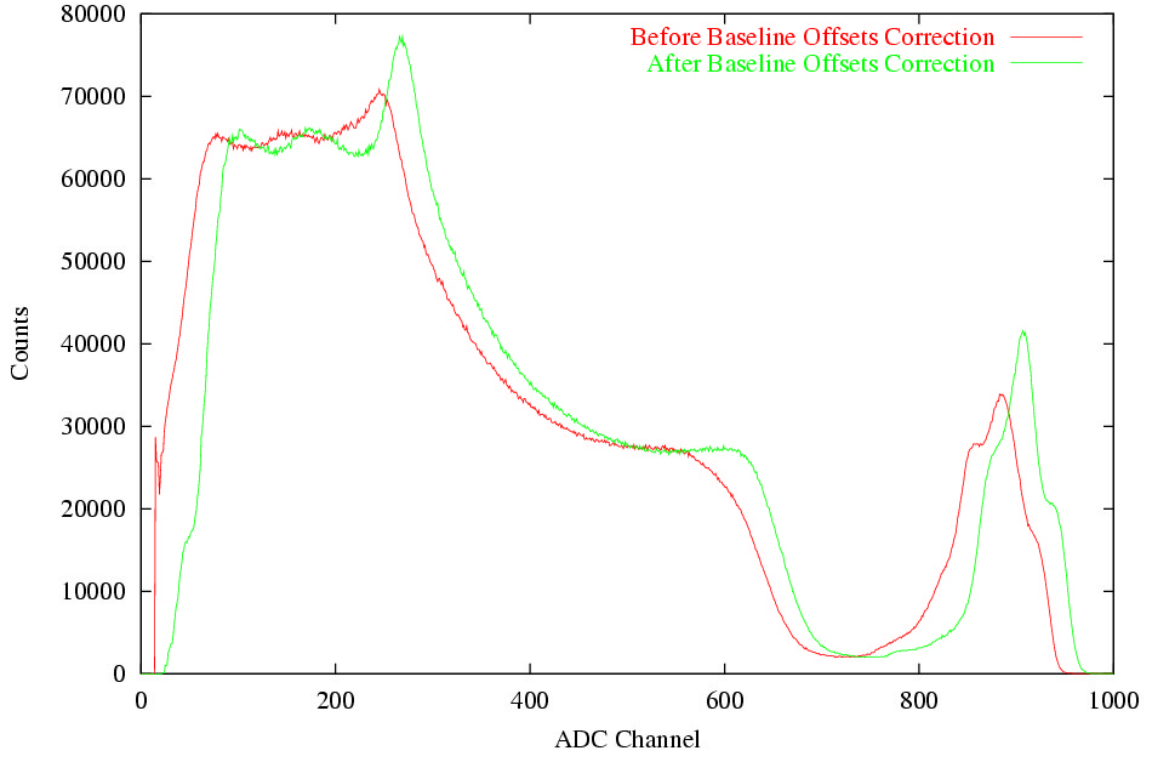
Figure 5.6. Raw spectra for single-pixel events from all pixels before and after the baseline offset correction.

5.1.5 Depth sensing and correction with C/A ratio

For the same amount of energy deposition at different depths, the percentage of signal loss due to electron trapping will vary since the longer path length the electrons travel the more electrons are trapped, resulting in photopeak broadening. The interaction depth can be derived from the cathode-to-anode signal ratio (C/A ratio)

$$d(n) = \frac{S_c(n)}{S_a(n)} \times N \tag{5.7}$$

where n is the channel number, d is the C/A ratio depth index, S_c and S_a are the cathode and the anode signals respectively, and N is a constant normalization factor. The detector is conceptually divided into slices of depth layers and together with the pixel anode pattern to form thousands of small voxels. Then, single-pixel events collected from

a ^{137}Cs source are recorded into the corresponding spectrum $Spectrum\_0(n, d(n))$ for each voxel according to the pixel location and the C/A ratio depth

$$S_a(n) \rightarrow Spectrum\_0(n, d(n)) \tag{5.8}$$

and the photopeak centroid $C\_D(n, d)$ can be determined for each voxel spectrum and used as the depth correction coefficient. The depth-separated spectra for one anode pixel are shown in Figure 5.7. The changes in the photopeak centroid are the integrative effects of the material non-uniformity in the lateral direction, and the electron trapping and the changes in the weighting potential in the depth direction. We know that these photopeaks are from a single gamma ray energy (662 keV). Thus, the relative position of these peaks can be used as the calibration data to correct for the effects described above and align to the same position to form a sharp photopeak

$$E(n) = \frac{S_a(n)}{C\_D(n, d(n))} \times E_0 \tag{5.9}$$

where C_D is the depth correction coefficients, E_0 is the calibration source energy and E is the calculated energy for the corresponding anode signal S_a.

5.1.6 Non-linearity correction

After the depth correction we can already obtain a spectrum with very sharp photopeak. However, if there is non-linearity in the system response, an energy calibration is needed. Furthermore, the key factor in good energy resolution for multiple-pixel events is good linearity in the system response - either the system has good linearity or has non-linearity that can be calibrated. Unfortunately, VAS2/TAT2 had prominent non-linearity (cf. Figure 5.8) that significantly degraded the energy resolution for multiple-pixel events. This might be one reason why previously energy resolution was at best 3.5% FWHM at 662 keV for two-pixel events from the VAS2/TAT2 system [52].
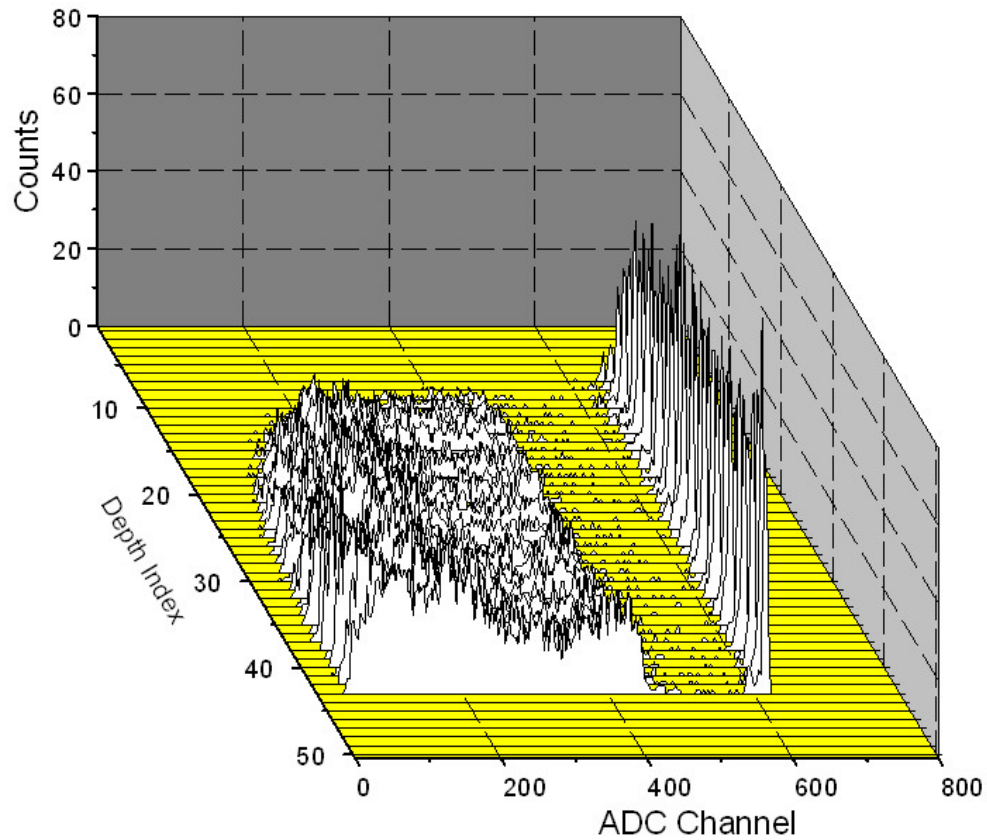
Figure 5.7. Single-pixel events spectra sorted into different C/A ratio depth indexes.

$$y = -0.000468\ x^2 + 1.356714\ x - 31.021069$$
$$R^2 = 1.000000$$
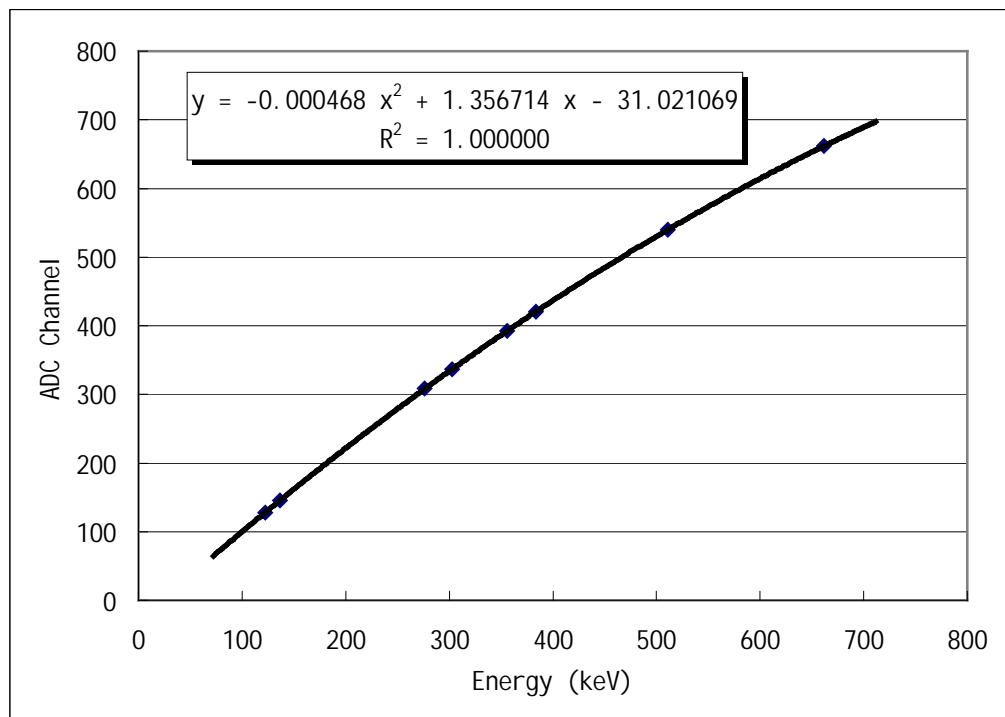
Figure 5.8. VAS2/TAT2 system non-linearity calibration curve.

To correct the non-linearity, we can use several gamma-ray sources that have energies covering the desired dynamic range. In the experiments, ^{57}Co (122 keV, 136 keV), ^{133}Ba (276 keV, 303 keV, 356 keV, 384 keV), ^{22}Na (511 keV), and ^{137}Cs (662 keV) were used. The non-linearity calibration data can be derived from the relation between the photopeak centroids and the expected energies. However, there is some difficulty here. Since the photopeak centroids used for non-linearity calibration can only be obtained after the depth correction, the non-linearity calibration has to be done after the depth correction. But this results in non-linearity and energy dependence in the depth itself according to Equation 5.7. In order to get correct depths for all energies, the non-linearity should be corrected before the depth correction. Thus, we first need to do a depth correction to get the photopeaks for all energies and derive the non-linearity correction parameters. Then apply the non-linearity correction to the anode signal before the depth correction, and go through the above calibration again to make a fine adjustment to the original non-linearity correction parameters. Iterations of non-linearity correction must be done until the results are satisfactory, as illustrated by the flow chart in Figure 5.9.

The above non-linearity calibration method worked well for the VAS2/TAT2 system. An alternative calibration method using test pulses was also studied. The calibration was done using the modified single-channel mode to automatically scan the output of the system with gradually increasing test pulse amplitude. There is no gamma ray source involved, which makes this method very simple and fast, and the calibration result is a single-pass direct measurement of the non-linearity in the electronics.

When the system is operated in the single channel readout mode, one channel is constantly connected to the output. The output waveform of this channel can be readout at a fixed sampling rate, just like we observe the waveform on the oscilloscope. Shown in

Figure 5.10 is the basic control sequence of the single channel mode. Two general purpose counters (GPCTR) on the PCI-6110 DAQ card were programmed to trigger and reset the system at a fixed rate. The channel being observed and the test pulse amplitude can be changed in the program. It is possible to modify this single-channel mode to let the program automatically change the test pulse amplitude and the channel and hence do linearity scans for all the channels.

```
┌─────────────────────┐                      ┌─────────────────────┐
│  Anode signal after │◄─────────────────────│ Apply the non-      │
│  the gain correction│                      │ linearity correction│
└─────────────────────┘                      │ to the anode signal │
          │                                  └─────────────────────┘
          ▼                                             ▲
┌─────────────────────┐                      ┌─────────────────────┐
│ Depth calibration ->│                      │ Adjust the non-     │
│ depth correction    │                      │ linearity correction│
│ coefficients        │                      │ coefficients        │
└─────────────────────┘                      └─────────────────────┘
          │                                             ▲
          ▼                                             │
┌─────────────────────┐                                 │
│ Depth corrected     │                                 │
│ spectra -> photopeaks│                                │
│ for different energies│                               │
└─────────────────────┘                                 │
          │                                             │
          ▼                                             │
      Is the error between                              │
      the corrected photopeak    ───── No ──────────────┘
      centroids and the true
      energies acceptable?
          │
         Yes
          ▼
┌─────────────────────┐
│ The final non-      │
│ linearity           │
│ coefficients        │
└─────────────────────┘
```

Figure 5.9. Flow chart of the iterative non-linearity correction procedures.
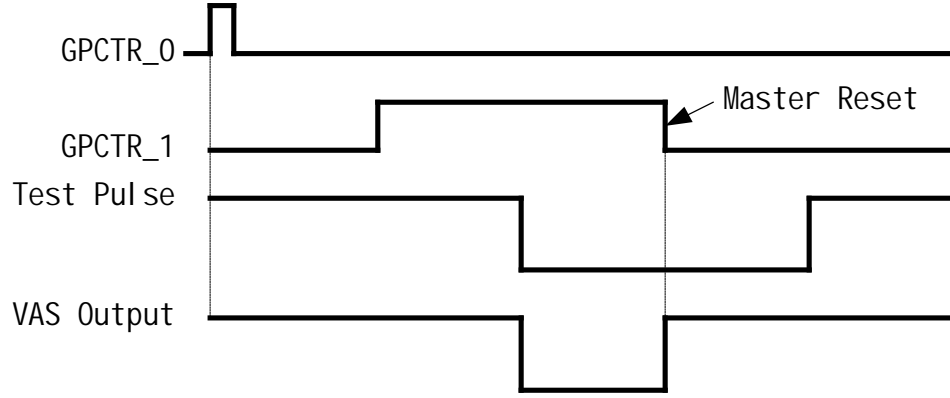
Figure 5.10. Control sequence of the single channel mode.

By programming the digital to analog converter (DAC) of the DAQ board, a special test pulse train was generated such that the test pulse amplitude would increase from 0 mV to 800 mV in a step of 10 mV and each amplitude was repeated for 100 times. The test pulse response of the VAS output was then binned into a spectrum, and the peak centroid was measured for each test pulse amplitude. To reduce the scan time, the cycle time was set to 500 µs for each test pulse. Thus, the scan time for one channel will be (800 mV range / 10 mV step) × (repeat 100 times) × 500 µs = 4s and the total scan time for all 128 channels is around 10 minutes. The scan results for one special channel and one normal channel of a VAS3/TAT3 system are shown in Figure 5.11.

From Figure 5.11 we can see that the special channel has very good linearity over the whole dynamic range. The normal channel has fairly good linearity for energies below 700 keV and shows non-linearity toward high energy. Both the special channel and the normal channel saturate at around channel -1800, which is the limit of the MCR3.

To practically use the linearity scan results for the non-linearity calibration, additional work is needed, such as the relation between the baseline detected in the single-channel mode and the serial readout mode and the accurate relation between the test pulse amplitude and the gamma ray energy.
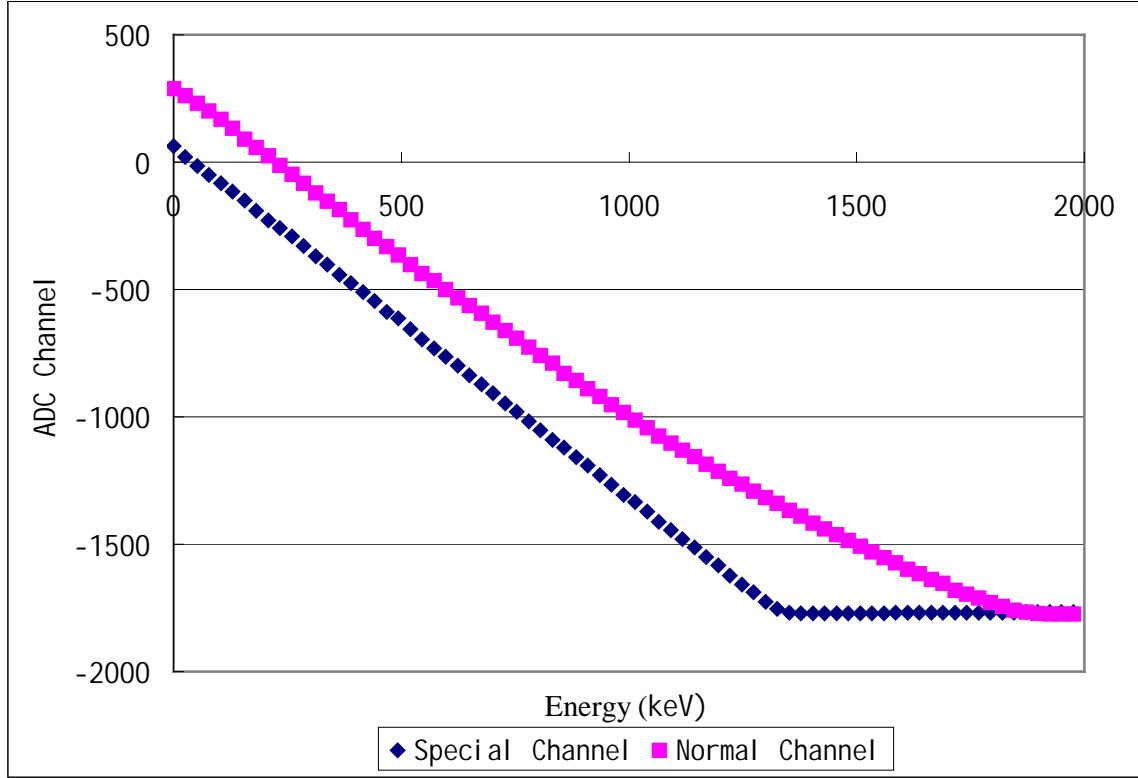
Figure 5.11. Linearity-scan results for one normal channel and one special channel of a VAS3/TAT3 system using the modified single-channel readout mode.

5.2 Multiple-pixel events

5.2.1 Electron drift time and C/A ratio correlation

For single-pixel events either the C/A ratio or the electron drift time can be used to get the interaction depth and to derive the depth correction coefficients. However, due to limited timing resolution, the depth correction coefficients derived from the electron drift time are worse than those derived from the C/A ratio and consequently result in poorer energy resolution. So, only the C/A ratio and the depth correction coefficients derived from the C/A ratio are used for single-pixel events.

For multiple-pixel events, although we can only get the interaction depths from the electron drift times, we still want to use the better depth correction coefficients

89

derived from the C/A ratio in the single-pixel events calibration. Thus, the relation between the C/A ratio and the electron drift time must first be calibrated for single-pixel events. Hence for multiple-pixel events, the equivalent C/A ratio can be deduced from the electron drift time for each pixel.

The timing signal for 662 keV photopeak events were recorded into channel number and C/A ratio depth indexed spectra:

$$t(n) \rightarrow Spectrum\_1(n, d(n)) \qquad (5.10)$$

where n is the channel number, d is the C/A ratio depth index derived from Equation 5.7 and t is the timing signal. The timing-amplitude-walk was not considered since the variation in the signal amplitude due to electron trapping is only a few percent. The timing spectrum for each depth should have a single peak because the events in the spectrum are from the same depth and have the same electron drift time, as can be seen in Figure 5.12. The relation between these peak centroids and the C/A ratio depths can be used as the calibration data to get the equivalent C/A ratio from the electron drift time, which can be expressed as

$$Spectrum\_1(n, d(n)) \rightarrow T\_C(n, d) \rightarrow T\_C'(n, t) \qquad (5.11)$$

$$T\_C'(n, t) \rightarrow d \qquad (5.12)$$

where T_C is the timing-peak centroid as a monotonic function of the C/A ratio depth d, T_C' is the conversion function from the electron drift time t to the C/A ratio depth d.

90
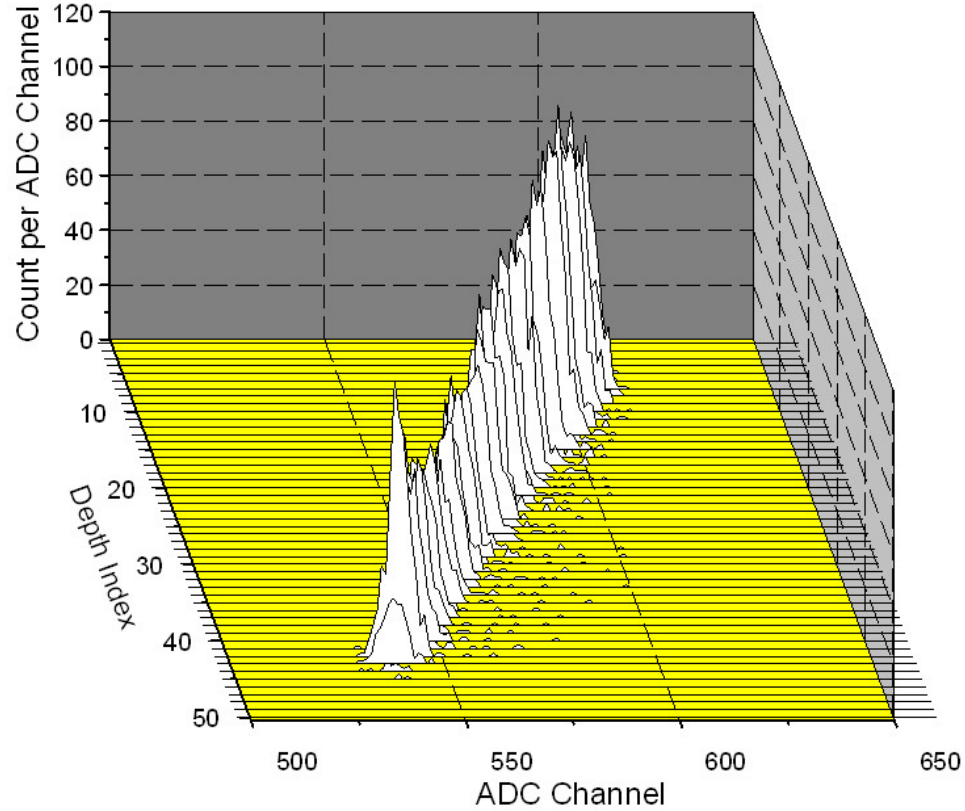
Figure 5.12. Timing spectra for 662 keV single-pixel photopeak events, depth separated.

5.2.2 Timing-Amplitude-Walk correction

The electron drift time is derived from the triggering time difference between the cathode and the anode pixel. The timing-amplitude-walk (TAW) in both the cathode and the anode signal can affect the accuracy of measurement on the electron drift time, as discussed in Chapter 3. Since the current ASIC cannot measure signal timing independent of pulse amplitude, the timing-amplitude-walk must be corrected for both the anode and the cathode signal. Timing calibration methods have been developed for the current ASIC.

5.2.2.1 Anode TAW calibration

Two-pixel 662 keV photopeak events were used to calibrate the TAW for the anode signal. For these two-pixel 662 keV photopeak events, there is no time-walk on the

cathode triggering time. However, each of the two anode signals can have an amplitude anywhere between 0 and 662 keV, and thus have time-walk on the anode triggering time. The smaller the anode signal, the later the anode will be triggered, and the more the deduced depth of interaction will be biased toward the cathode side. Figure 5.13 illustrates the TAW calibration for the anode signal. Suppose we have a 662 keV two-pixel event with the two interactions of different energy depositions occurring at the same depth. Due to the amplitude time-walk, the triggering time of the two anode pixels will be different, as depicted by the blue bars - the shorter the blue bar, the longer the electron drift time appears to be.
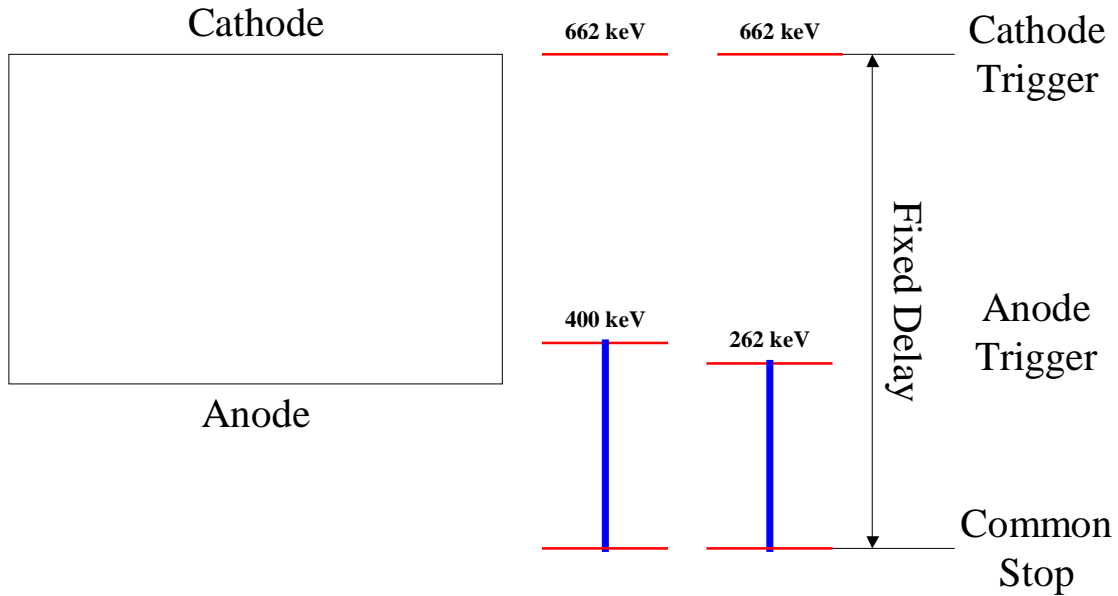
Figure 5.13. Illustration of the anode timing-amplitude-walk calibration.

7

Therefore, for these 662 keV two-pixel photopeak events, if we record the anode timing signalsfor different energy ranges, changes in the timing spectra should be observed, as can be seen in Figure 5.14. The left side of each timing spectrum corresponds to interactions that happened on the cathode side, while the right side of each timing spectrum is from interactions happened on the anode side. We can clearly see that

the timing spectrum shifts to the cathode side (left) as the energy decreases. The key basis of this calibration is (1) there is no time-walk in the cathode triggering time and (2) we know that the counts on the left edge of the timing spectra come from the interactions very close to the cathode surface and hence the same physical depth. Therefore, the differences in left edge positions of the timing spectra for different energy ranges should only be due to timing-amplitude-walk on the anode signal. The advantage of this method is that no hardware collimation is required.

By measuring the shift of the left edge of each timing spectrum, we can establish the relation between the time-walk and the amplitude of anode signals, as shown in Figure 5.15. For simplification, average values of two fitting curves are used for interpolation. This relation can then be used to correct the TAW in anode timing signals.

Considering the actual weighting potential of the anode at different depths, we may worry that for different pulse amplitude, the anode triggering locations are different – the higher the energy, the farther away from the anode will the anode be triggered. However, if this is really the case, it is also taken care of in the calibration described above.
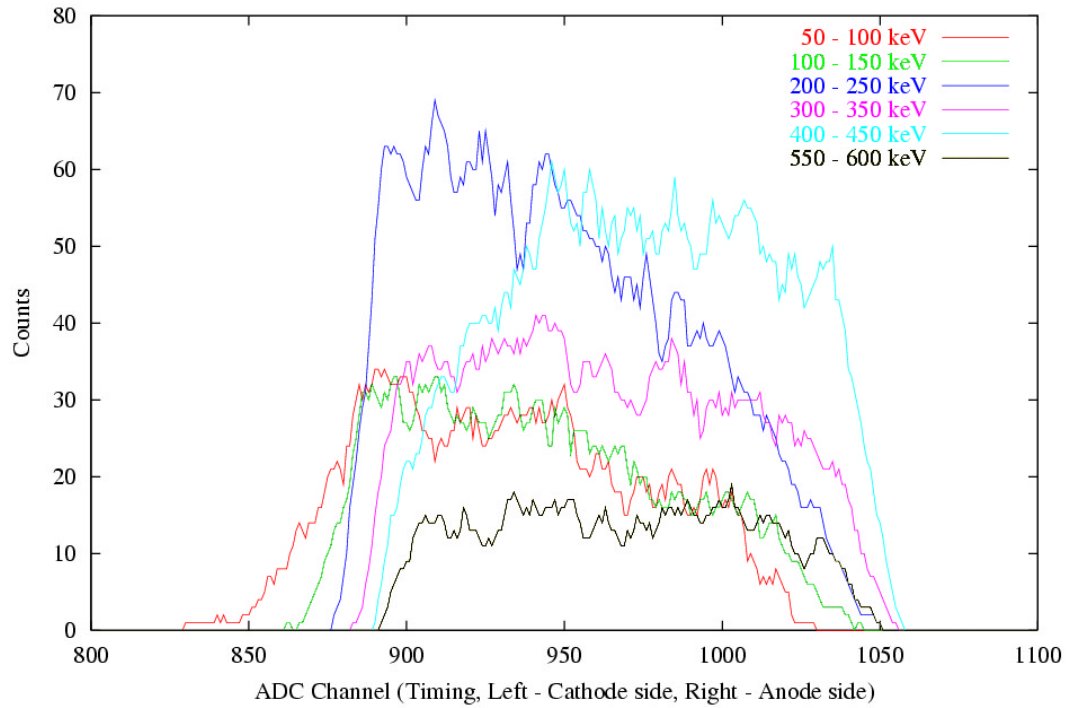
Figure 5.14. Anode timing spectra of different energy ranges for 662 keV two-pixel photopeak events.
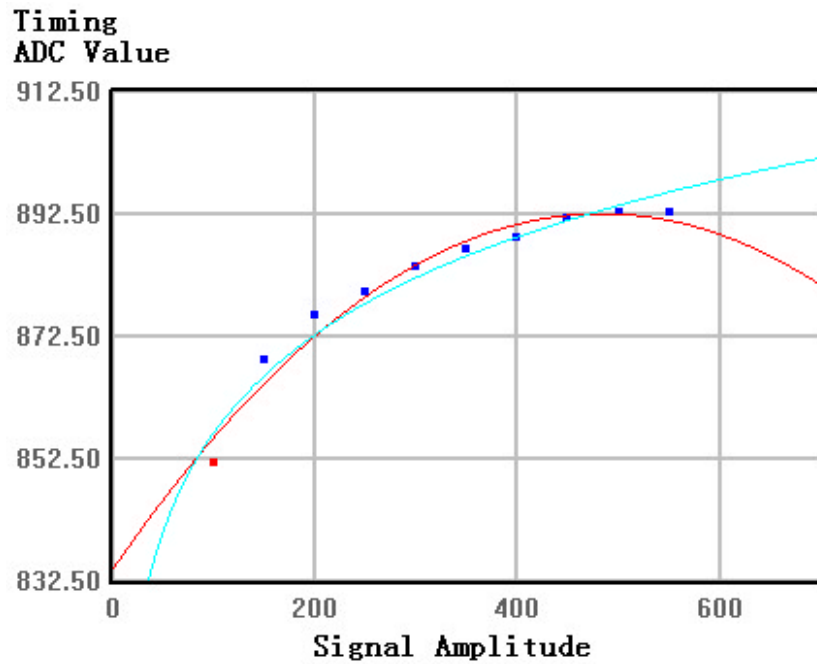
Figure 5.15. Relationship between the position of the left edge of the timing spectrum and the anode signal amplitude. Average values of two fitting curves are used for interpolation.

5.2.2.2 Cathode TAW calibration

The TAW calibration for the cathode signal can be done using all single-pixel events (not only photopeak events). For single pixel events, the events occurring near the cathode (thus with the same electron drift time) can be chosen using C/A ratio. Since TAW in the anode signal is already corrected using the method discussed in the previous section, anode signals of different amplitudes are now triggered at the same time after correction. If we again separate the timing spectrum for different energy ranges, the difference in the timing spectra should only be due to the TAW of the cathode signal. Figure 5.16 illustrates TAW calibration for the cathode signal. Suppose we have two single-pixel events of different energy depositions occurring at the same depth. The amplitude time-walk of the anode signal is already corrected. However, the triggering time of the cathode signal will not be the same due to the amplitude time-walk of the cathode signal. The higher the energy, the earlier the cathode will be triggered. Because of the fixed delay following the cathode trigger, the timing signal (blue bar) of the event triggered will be stopped earlier and have lower amplitude, biasing towards the cathode side.
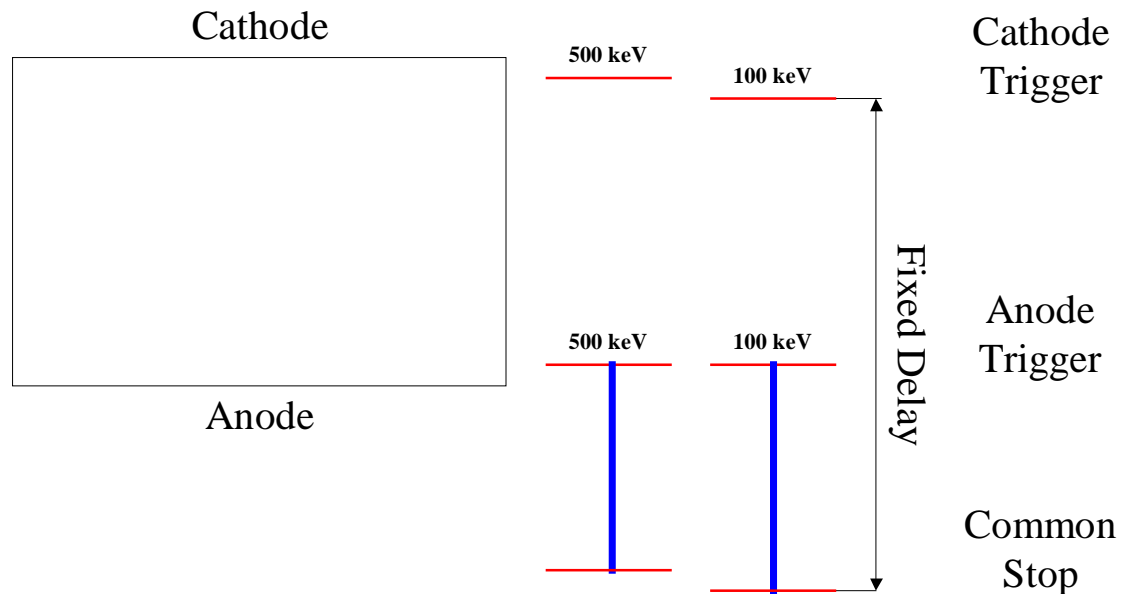
Figure 5.16. Illustration of the anode timing-amplitude-walk calibration.

Similar to the TAW calibration of the anode signal, if we record the timing signal (with anode TAW already corrected) of single-pixel events occurring near the cathode (selected using C/A ratio) into spectra of different energy ranges, variation in the centroid timing which can be seen in Figure 5.17, should only be due to timing-amplitude-walk of the cathode signal. Figure 5.17 also shows that the timing resolution degrades with decreasing signal amplitude due to the poorer signal to noise ratio, which agrees well with the modeling in Chapter 3. By measuring the peak centroids of timing measurement, we can establish the relationship between the time-walk and the cathode signal amplitude, as shown in Figure 5.18. This relation can then be used to correct the TAW in the cathode timing signal.
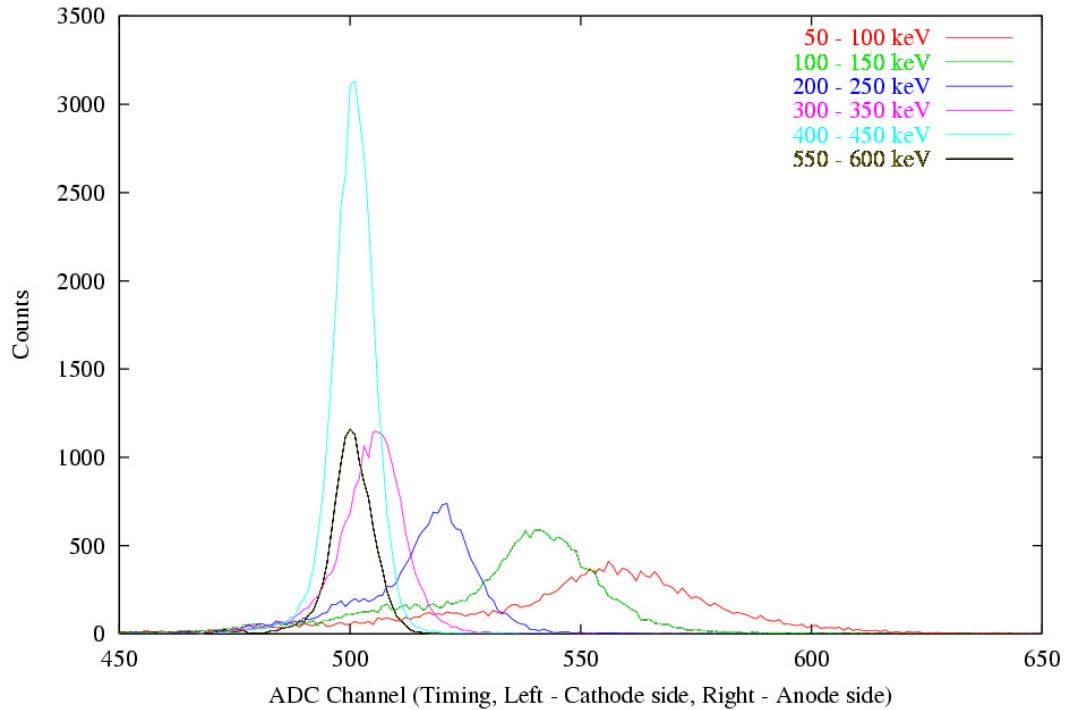
Figure 5.17. Timing spectra (with anode TAW corrected) of different energy ranges for single-pixel events.
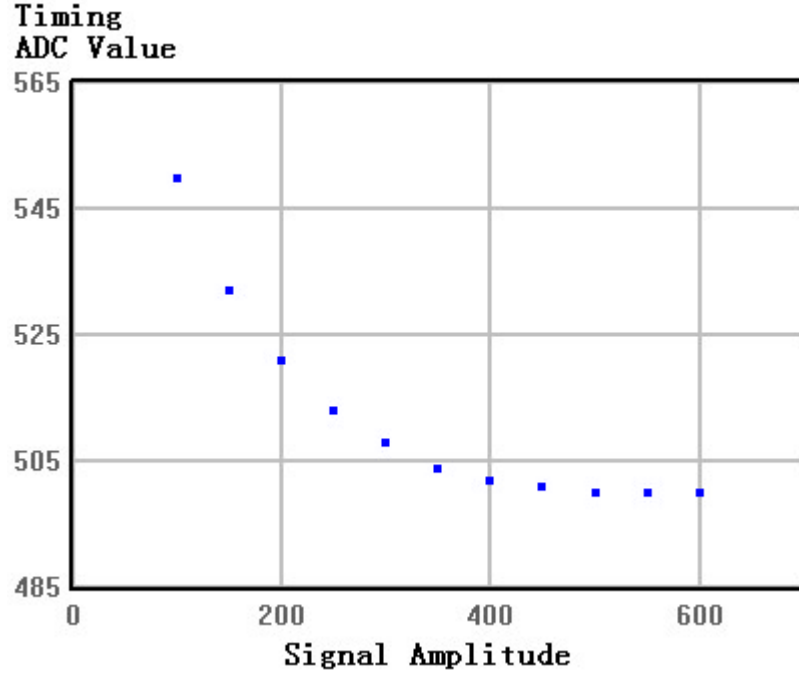
Figure 5.18. Relation between the position of the timing peak centroid and the cathode signal amplitude.

5.2.3 Depth deviation reduction with the cathode signal

For multiple-pixel events, the electron drift time is used to obtain the depth for each individual interaction. But the cathode signal amplitude is not utilized. This additional information can be used to increase the accuracy of the depth measurement derived from the electron drift time.

Equation 5.13 shows the basic technique of using the calculated and measured cathode signal ratio to correct for the depth:

$$R = \frac{C_c}{M_c} = \frac{C_{a1} \times d_{t1} + C_{a2} \times d_{t2}}{M_c} \tag{5.13}$$

where C_{a1} and C_{a2} are the calibrated anode signals for the two pixels, d_{t1} and d_{t2} are the depths derived from the timing signals of the two pixels with electron drift time $t1$ and $t2$ respectively, C_c and M_c are the calculated total cathode signal and measured total cathode signal respectively, and R is their ratio.

97

The curve in Figure 5.19 is the distribution of the ratio between calculated and measured cathode signals for all two-pixel events. The distribution peaks at $R_0 = 0.97$. Therefore, if this ratio deviate from the expected value of 0.97, we can correct the measured centroid depth so that the ratio is consistent with the expected value. The correction procedure can be expressed as below

$$D_{t1} = \frac{R_0}{R} d_{t1} \tag{5.14}$$

$$D_{t2} = \frac{R_0}{R} d_{t2} \tag{5.15}$$

where D_{t1} and D_{t2} are the calculated depthsafter correction.

Taking two-pixel events as an example, since the depth resolution from the timing signal is worse than from the C/A ratio, if the two depths derived from timing signals are both larger or smaller than the actual depths, the calculated to measured cathode signal ratio will be larger or smaller than the coefficient R_0. Therefore, the depths can be corrected using this ratio. If one depth is larger and the other is smaller, the correction will have less effect. In these cases, the correction on detector response, such as the effects of charge trapping and induction, is opposite in amplitude for these two interactions. The error in each correction due to the error in depth measurement tends to compensate on each other. This makes the reconstructed signal amplitude deviate less from the true value.
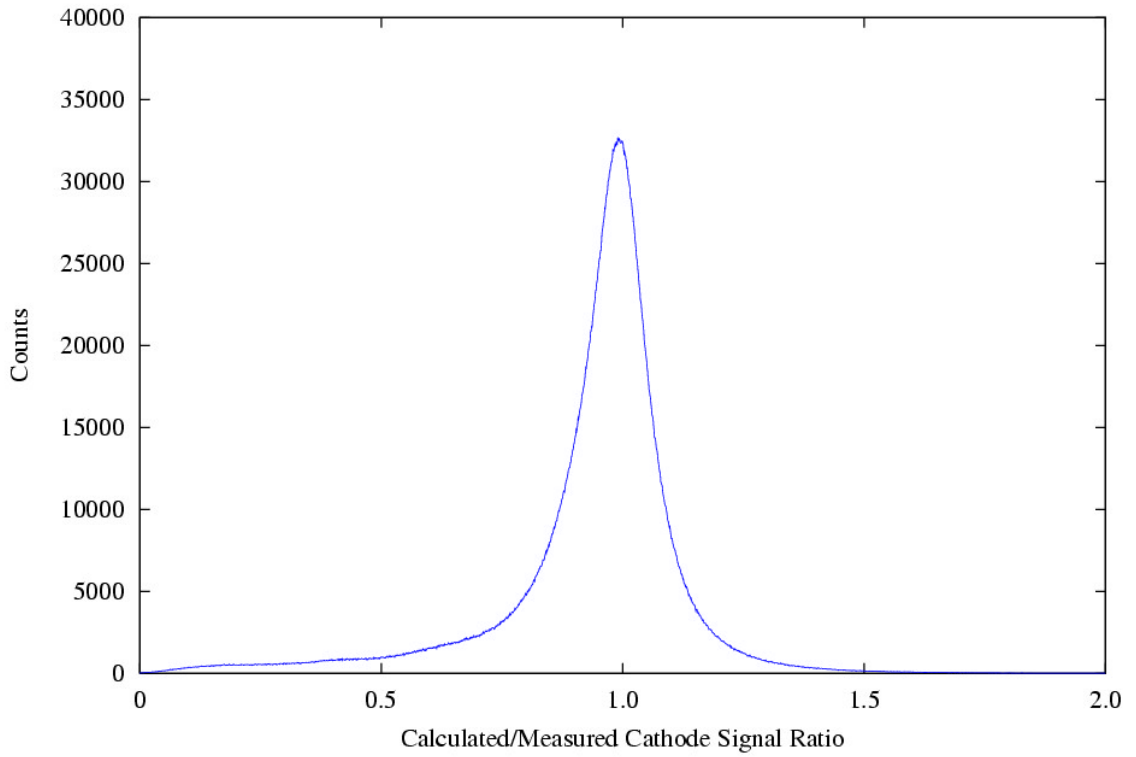
Figure 5.19. Distributions of the calculated to measured cathode signal ratio of all two-pixel events.

There are two comments on this correction method. First, this calibration procedure may be used several times in an iterative manner in order to achieve the best correction. Second, we should make sure that the cathode signal is not saturated due to limited dynamic range. The induced signal on the cathode is the sum of all the energy deposited and may be larger than any anode signals. If the cathode signal is saturated, this correction method cannot be used; otherwise the corrected depths have a systematic bias.

5.2.4 Weighting potential cross-talk correction

As discussed in Chapter 3, due to weighting potential cross-talk, the electron clouds of multiple-pixel events will induce signal on other pixels. This effect depends on the distance between the electron clouds and the centroid depth. The amplitudes

measured from both pixels are reduced, and the recorded energies are less than the actual deposited energies. To calibrate this effect, all two-pixel events are separated into a 2-D array of spectra according to centroid depths and distances between interactions. The recorded total energy deposited (which will be less than the actual energy deposited) is determined for each combination of the centroid depth and the lateral separation between interactions, as shown in Figure 5.20. A correction factor W, defined by the true energy divided by the simple summed energy, is determined for each centroid depth and interaction distance pair. The individual events are then adjusted by the same correction factor using

$$E = S \times W(\sqrt{\Delta x^2 + \Delta y^2}, \overline{d}) \tag{5.16}$$

where $\sqrt{\Delta x^2 + \Delta y^2}$ is the distance of the two pixels, $\overline{d}$ is the centroid depth of the two interactions, W is the weighting potential cross-talk correction factor, S is the uncorrected energy and E is the final corrected energy.

For three-pixel and four-pixel events, the weighting potential cross-talk correction factors can be calculated from those factors obtained from two-pixel events using the following equations

$$W_{123} = \sqrt[3]{W_{12} \times W_{13} \times W_{23}} \tag{5.17}$$

$$W_{1234} = \sqrt[4]{W_{12} \times W_{13} \times W_{14} \times W_{23} \times W_{24} \times W_{34}} \tag{5.18}$$

where W_{12}, W_{13} and etc are the weighting potential cross-talk correction factors for different combinations of the multiple pixels.
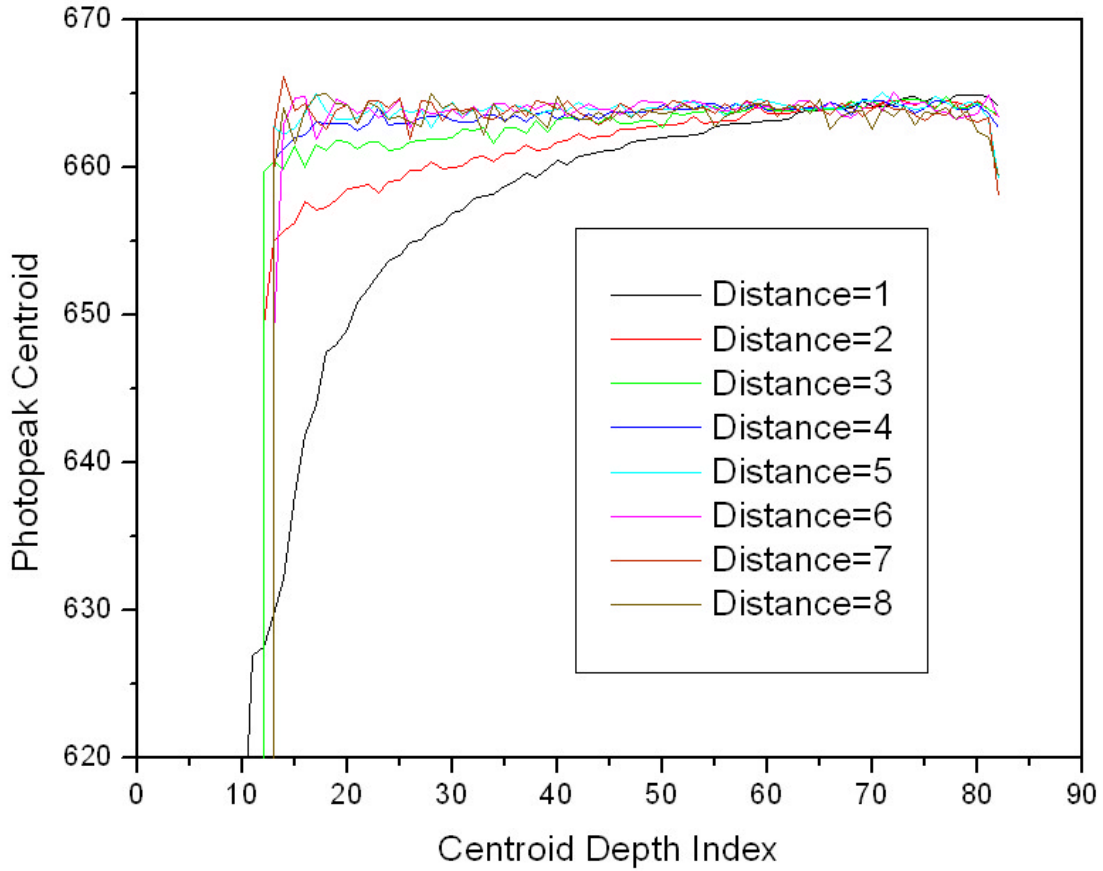
Figure 5.20. Photopeak centroid of 662 keV two-pixel events as a function of the distance between the two pixels and the centroid depth of the two interactions. The distance is in the unit of the pixel pitch.

5.3 Summary

The calibration procedures of single-pixel events are summarized in Figure 5.21. Due to the improved design in the ASIC, different calibrations are needed in the VAS2/TAT2 system and the VAS3.1/TAT3 system, such as the iterative non-linearity calibration and the baseline offsets calibration. For multiple-pixel events, the calibration procedures are the same for both systems, as shown in Figure 5.22. After the calibration coefficients are obtained, the single-pixel and multiple-pixel events can be reconstructed

following the procedures depicted in Figure 5.23. Different procedures are designated in different colors for the VAS2/TAT2 system and the VAS3.1/TAT3 system.

VAS2/TAT2
Single-Pixel Events
Calibration Procedures

VAS3.1/TAT3
Single-Pixel Events
Calibration Procedures
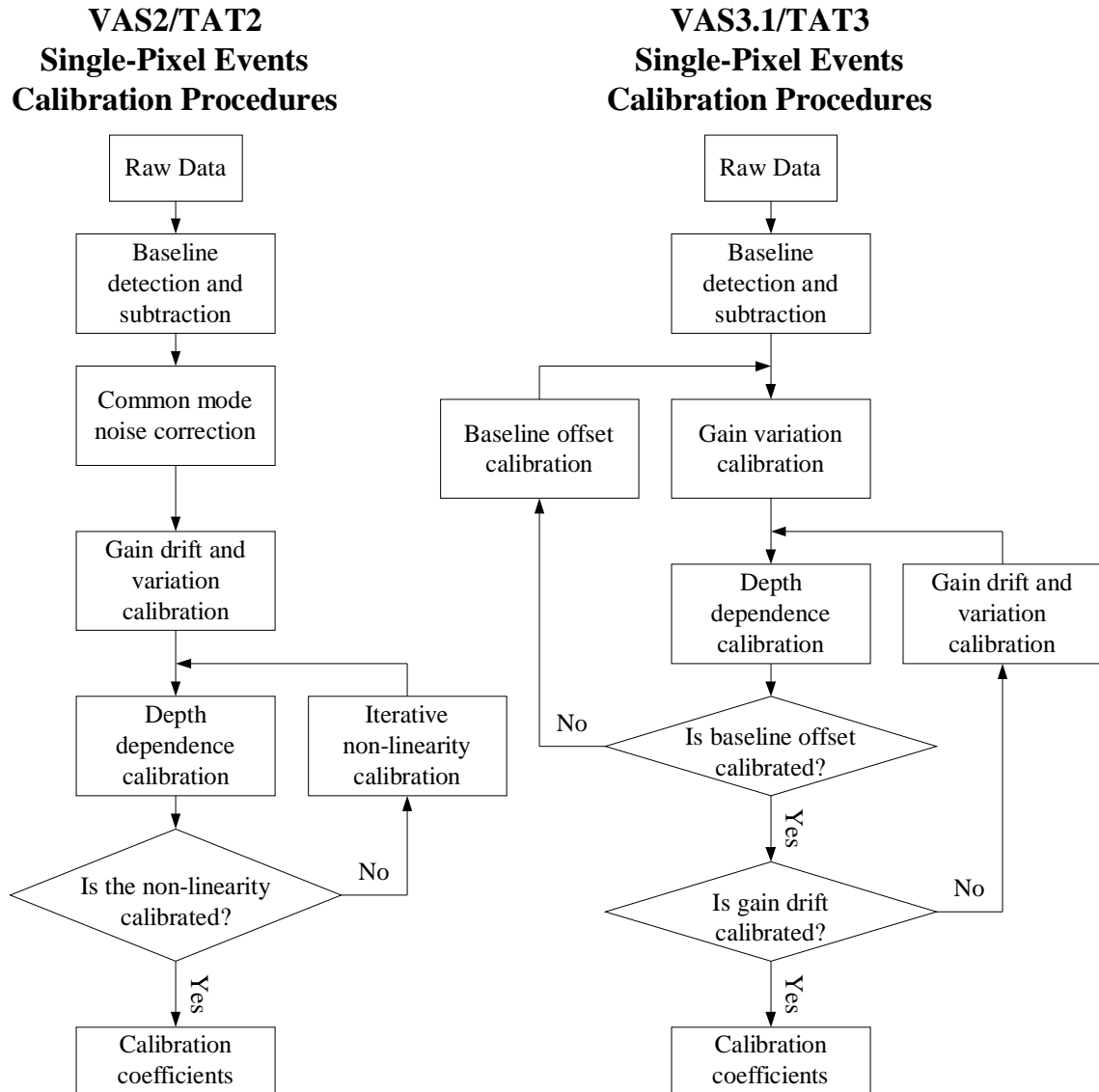
Figure 5.21. Single-pixel events calibration procedures for the VAS2/TAT2 system and the VAS3.1/TAT3 system.

Multiple-Pixel Events
Calibration Procedures

```
┌─────────────────────────────┐     ┌─────────────────────────────┐
│ Raw data + single-pixel     │───▶│ Electron drift time & C/A   │
│ events calibration          │     │ ratio correlation           │
│ coefficents                 │     │ calibration                 │
└─────────────────────────────┘     └─────────────────────────────┘
                                                    │
                                                    ▼
┌─────────────────────────────┐     ┌─────────────────────────────┐
│ Cathode timing-amplitude-   │◀───│ Anode timing-amplitude-walk │
│ walk calibration            │     │ calibration                 │
└─────────────────────────────┘     └─────────────────────────────┘
              │
              ▼
┌─────────────────────────────┐     ┌─────────────────────────────┐
│ Calculated/measured cathode │───▶│ Weighting potential cross-  │
│ signal calibration          │     │ talk calibration            │
└─────────────────────────────┘     └─────────────────────────────┘
                                                    │
                                                    ▼
                                    ┌─────────────────────────────┐
                                    │ Multiple-pixel events       │
                                    │ calibration coefficients    │
                                    └─────────────────────────────┘
```
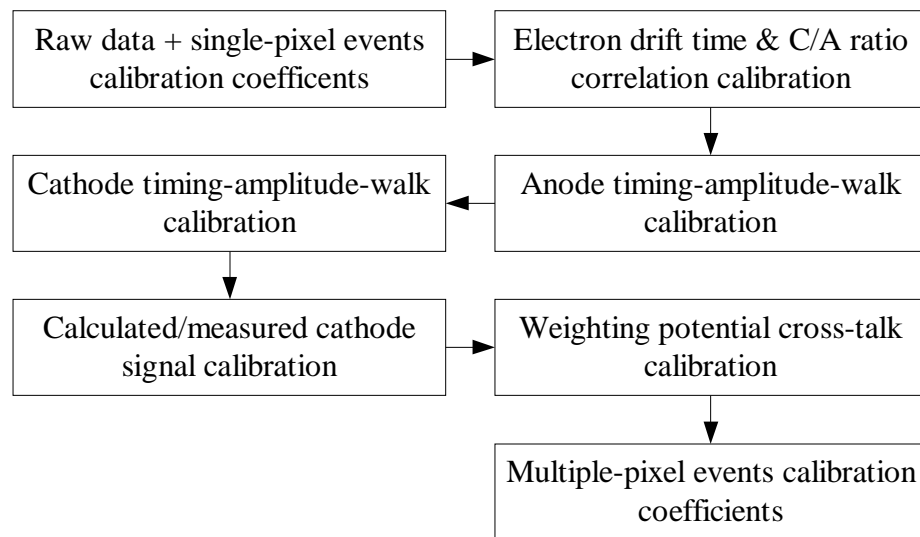
Figure 5.22. Multiple-pixel events calibration procedures. No difference between the VAS2/TAT2 system and the VAS3.1/TAT3 system.

Events Reconstruction
Procedures

Raw Data

↓

Baseline detection and subtraction

Common mode noise correction   Baseline offset correction

Gain drift and variation correction

Non-linearity correction

Single-pixel events? — No → Timing-amplitude walk correction

Yes ↓   ↓

Depth from C/A ratio   Depths from electron drift times

↓   ↓

Depth correction   Calculate/measured cathode signal correction

↓   ↓

Energy and 3-d coordinates for single-pixel events   Depth correction

                                     ↓

                                     Weighting potential cross-talk correction

                                     ↓

                                     Energies and 3-d coordinates for multiple pixels

VAS2/TAT2 System

VAS3.1/TAT3 System

Figure 5.23. Single-pixel and multiple-pixel events reconstruction procedures. The differences between the VAS2/TAT2 system and the VAS3.1/TAT3 system are designated in different colors.

CHAPTER 6
EXPERIMENTAL RESULTS

Two generations of electronic readout for the 3-D CdZnTe spectrometer (three versions of ASICs - VAS2/TAT2, VAS3/TAT3 and VAS3.1/TAT3) have been developed. Two CdZnTe detectors (#2.2 and #2.3) of the same dimensions (1.5 cm $\times$ 1.5 cm $\times$ 1.0 cm) have been wire-bonded to and tested with these electronics.

The cathode was biased at a negative potential so that the electrons created by the gamma ray interactions can drift towards the anode pixels. Both detectors could be biased up to -2500 V on the cathode. But the cathode signal became unstable after several hours. Therefore, a lower cathode bias voltage was chosen for the stability of the cathode signal.

The common grid electrode between the pixels was biased at a negative voltage to steer the electrons drifting towards the anode pixels. The larger the voltage difference between the anode pixels and the grid, the more efficient the steering effect is. However, we do not want the grid bias to be excessively high either because high grid bias results in high leakage current. The selection of the grid bias voltage was based on an electric field calculation to prevent charge sharing on the grid electrodes.

Detector #2.2 was biased at -2200 V on the cathode and -65 V on the anode grid. Detector #2.3 was biased at -2000 V on the cathode and -60 V on the anode grid. The anode pixels were at ground potential and connected to the input of the ASIC by wire-bonds. Both systems were operated at room temperature ($\sim 20^{\circ}C$ - $28^{\circ}C$), irradiated from the cathode side with uncollimated gamma-ray sources placed 5 cm away from the cathode. A 10-μCi ^{137}Cs 662 keV gamma-ray source was used as the major calibration

source for its simple spectrum profile and moderately high energy. Since the data will be divided into thousands of small voxels during the data processing, a huge amount of data must be collected. It normally takes ~40 hours to collect enough data for the calibration of each detector. Data from ^{133}Ba, ^{57}Co and ^{22}Na gamma-ray sources were also collected for the non-linearity calibration in the VAS2/TAT2 system. Since the VAS3.1/TAT3 system has low triggering threshold, data from ^{241}Am source were also collected for measuring the electron mobility-lifetime products and estimating the electronic noise.

The experimental results from both generation detectors, such as the energy resolution for single-pixel and multiple-pixel events and the electron mobility-lifetime products are presented and compared in this chapter.

6.1 Results for VAS2/TAT2 Systems

6.1.1 Electronic noise

Before the detector is wire-bonded to the ASIC, the electronic noise can be measured by directly injecting a test pulse into the input pads of the ASIC. However, this is impossible to do without damaging the wire-bonds after the detector has been wire-bonded to the ASIC and the bias voltage applied to the detector. Due to this limitation, the electronic noise cannot be measured directly. Instead, the energy resolution measured for a low-energy gamma ray was used to estimate the electronic noise.

Because of the high triggering threshold in the VAS2/TAT2 systems, 60 keV photons from ^{241}Am cannot be observed. Instead, a ^{133}Ba gamma ray source was used to irradiate the detector from the cathode side. Most of the 81 keV photoelectric events should occur in a thin layer near the cathode. The FWHM of the 81 keV photopeak was then used to estimate the electronic noise of the system and found to be ~6 keV FWHM.

6.1.2 Energy resolution for single-pixel events

After the calibration procedures discussed in Chapter 5 were performed, energy resolution of 1.11% FWHM and 1.14% FWHM at 662 keV were achieved for single-pixel events for detector #2.2 and #2.3, respectively. The energy spectrum for 662 keV single-pixel events is shown in Figure 6.1. The 662 keV photopeak is very sharp at the high-energy edge but has a small low-energy tail. A small bump in the lower energy tail ~23 keV below the 662 keV photopeak can be barely observed. This is believed to be the Cd X-ray escape peak from the 662 keV photoelectric interactions occurring very near the cathode surface.

The distributions of the 662 keV single-pixel events energy resolution for both detector #2.2 and #2.3 are shown in Figure 6.2. We can see that detector #2.2 appears to have better overall material quality than detector #2.3 (, which was later found to be not the case). One possible reason for detector #2.3's worse performance is material or surface defects shown in the top 3 rows. The other possible reason is that the VAS2 ASIC chip used to read out signals from that region has a smaller gain and worse signal/noise ratio than the ASICs used to read out other regions. However, in the good regions of detector #2.3, there are more pixels that have an energy resolution of better than 1% than detector #2.2, which makes the overall energy resolution of detector #2.3 comparable to that of detector #2.2, as can be seen in Table 6.1.

Figure 6.1. Single-pixel events energy spectrum from a ^{137}Cs source collected for 40 hours from all working pixels in detector #2.2.

Figure 6.2. Energy resolution distribution for single-pixel events from a ^{137}Cs source collected over 40 hours for (A): Detector #2.2 and VAS2/TAT2 system, (B): Detector #2.3 and VAS2/TAT2 system.

6.1.3 Energy resolution for multiple-pixel events

As discussed in Chapter 5, additional calibrations must be carried out for multiple-pixel events. After the calibration, energy resolution of 1.57% FWHM and

2.13% FWHM at 662 keV were achieved for two-pixel and three-pixel events respectively for detector #2.2. Detector #2.3 yielded 1.64% FWHM and 2.2% FWHM at 662 keV for two-pixel and three-pixel events respectively. Even for four pixel events the energy resolution is better than 3% FWHM for both detectors, as can be seen in Table 6.1. The two-pixel events energy spectrum for detector #2.2 is shown in Figure 6.3.

Figure 6.4 shows the comparison of the 662 keV energy spectra for single-pixel, two-pixel, three-pixel and four-pixel events. The photopeaks have been normalized to the same height for better comparison. The rather complete absorption of the gamma ray in multiple-pixel events is evident from the high peak to Compton ratio in the multiple-pixel events spectra and is one important feature of the intelligent gamma-ray spectroscopy [54].

Table 6.1. Energy resolution (FWHM) at 662 keV for single-pixel events and multiple-pixel events from the whole bulk of two detectors read out by VAS2/TAT2.

Detector	Single-Pixel Events	Two-Pixel Events	Three-Pixel Events	Four-Pixel Events
#2.2 biased at -2200 V, -65 V	1.11% (7.35 keV)	1.57% (10.4 keV)	2.13% (14.1 keV)	2.64% (17.5 keV)
#2.3 biased at -2000 V, -60V	1.14% (7.55 keV)	1.64% (10.9 keV)	2.2% (14.6 keV)	2.74% (18.1 keV)

Figure 6.3. Two-pixel events energy spectrum from a ^{137}Cs source collected for 40 hours from all working pixels in detector #2.2.
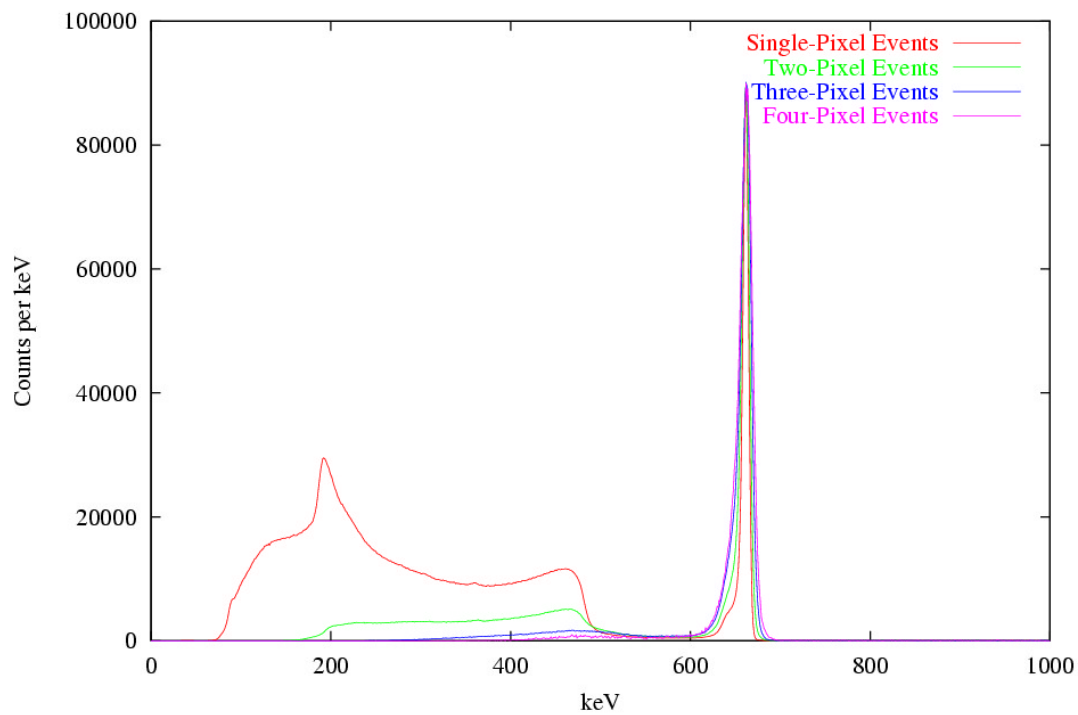
Figure 6.4. Comparison of 662 keV energy spectra for single-pixel, two-pixel, three-pixel and four-pixel events.

6.1.4 Energy spectrum for multiple gamma-ray sources

      Data from multiple gamma-ray sources, ^{57}Co, ^{133}Ba, ^{22}Na and ^{137}Cs, were collected to verify the spectroscopic capability of the system. The calibrated energy spectra for single-pixel events and two-pixel events are shown in Figure 6.5 and 6.6, respectively. The good energy resolution is preserved through all energies and the photopeaks are well distinguished. The low energy threshold of the two-pixel events is around two times that of the single-pixel events, since both of the two pixels must pass the triggering threshold.
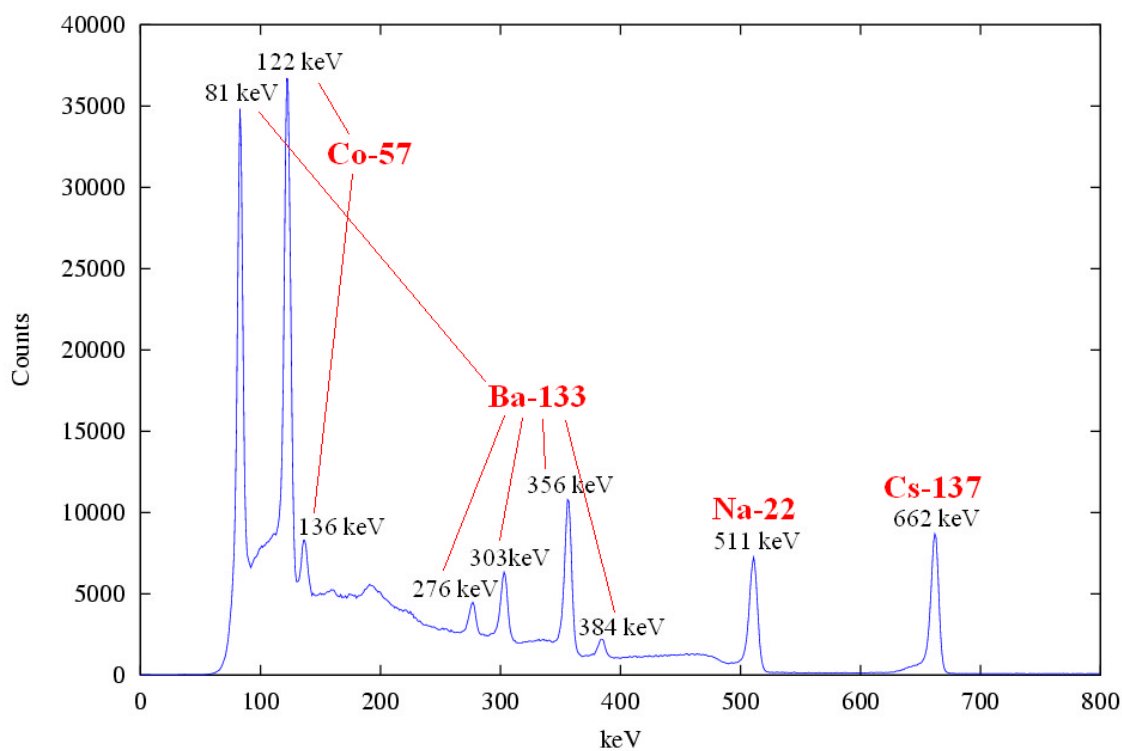
Figure 6.5. Single-pixel events energy spectrum for multiple gamma-ray sources collected for 1 hour from all working pixels in detector #2.2.
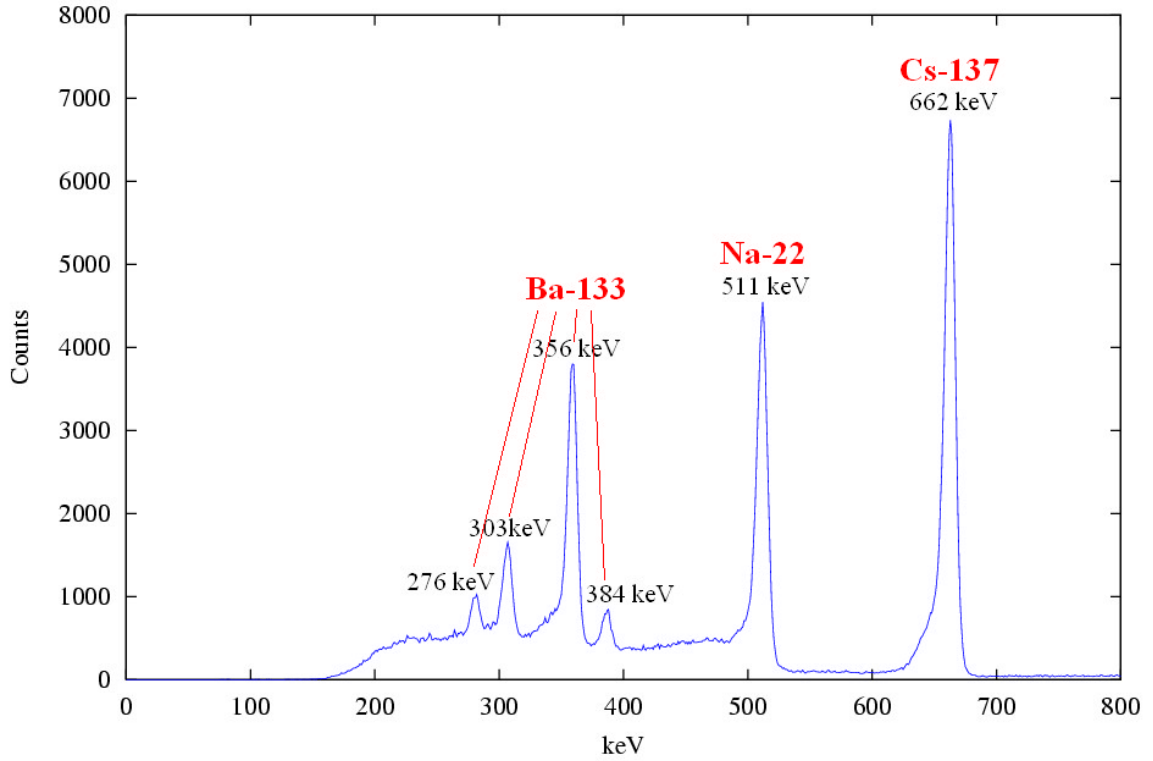
Figure 6.6. Two-pixel events energy spectrum for multiple gamma-ray sources collected for 1 hour from all working pixels in detector #2.2.

6.2 Results for VAS3.1/TAT3 Systems

6.2.1 Electronic noise

The VAS3.1/TAT3 systems have several significant improvements over the VAS2/TAT2 systems, such as the stable baseline and gain, the better linearity and lower electronic noise and cross-talk noise. Before the detector was wire-bonded to the ASICs, the electronic noise was measured to be ~3 keV FWHM by directly injecting test pulses into the inputs of the ASIC.

However, due to a design limitation, the electronic noise of the ASIC cannot be directly measured after the ASIC has been wire-bonded to the detector. In order to

estimate the overall electronic noise of the system, an uncollimated [241]Am source was placed 5 cm away from the cathode. The 59.5 keV gamma rays from the [241]Am source should all be stopped in a very thin layer on the cathode side. So, the collected anode signals should all come from the interactions at the same depth, without extra broadening due to depth dependence.

The energy resolution of the [241]Am anode spectrum was measured to be ~4.8 keV FWHM, as shown in Figure 6.7. If we only consider the statistical fluctuation in the charge carrier creation and assume a Fano factor of 0.1 [79], the electronic noise in the channels reading out the anode signal should be less than 4.5 keV FWHM after removing the photopeak broadening due to charge carrier generation from the observed overall energy resolution. Similarly, the electronic noise in the channel reading out the cathode signal was estimated to be ~7 keV FWHM.
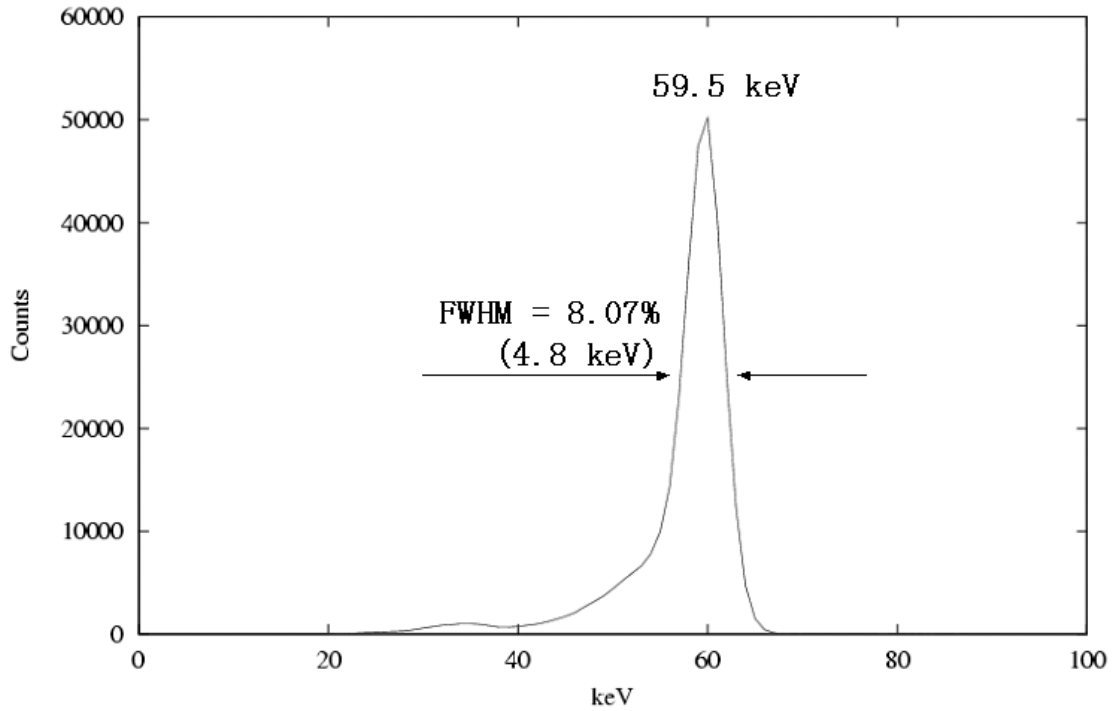
Figure 6.7. [241]Am energy spectrum for detector #2.2+VAS3.1/TAT3 system.

6.2.2 Energy resolution for single-pixel events

By doing 3-D corrections, an unprecedented energy resolution of 0.93% FWHM at 662 keV for single-pixel events was achieved from the entire 2.25 cm^3 volume of detector #2.2 with an uncollimated ^{137}Cs source, as shown in Figure 6.8. As a result of the much lower thresholds than the previous systems, the 32 keV ^{137}Cs K x-ray was observed in the 3-D CdZnTe system for the first time. Later, an even better energy resolution of 0.78% FWHM at 662 keV for single-pixel events was achieved for detector #2.3.

Figure 6.9 shows the energy resolution (FWHM at 662 keV) distribution for single-pixel events for two detectors. The bad pixels in the lower-left corner of detector #2.2 and on the lower-right edge of detector #2.3 are probably due to bad wire-bond. More than 2/3 of the pixels of detector #2.2 and 116 pixels of detector #2.3 have better than 1% FWHM energy resolution. 16 pixels of detector #2.3 are even better than 0.7% FWHM.
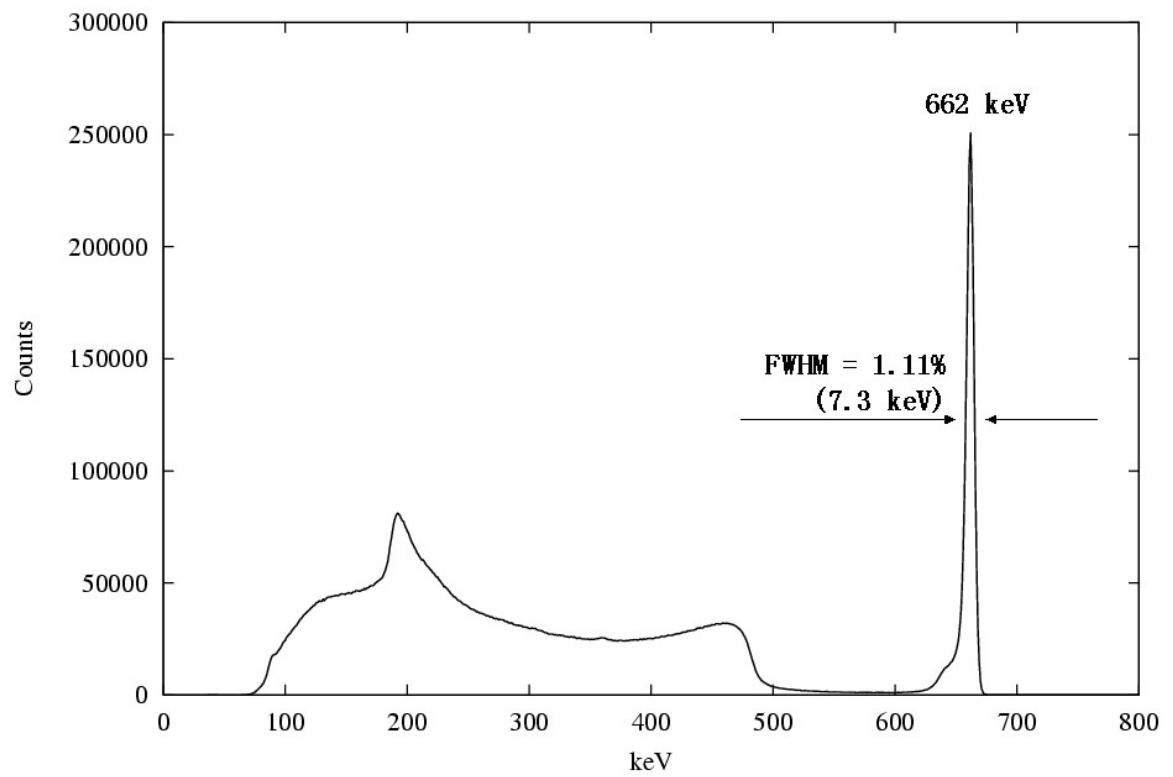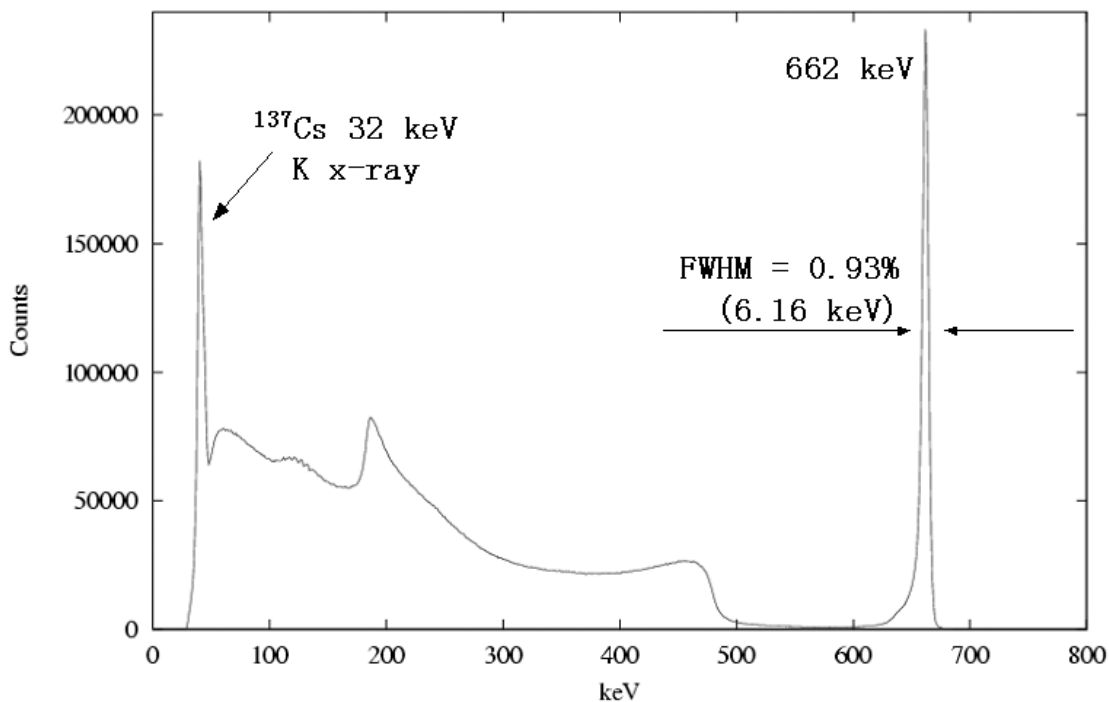

Figure 6.8. Single-pixel events energy spectrum from a ^{137}Cs source collected for 40 hours from all working pixels in detector #2.2+VAS3.1/TAT3 system.
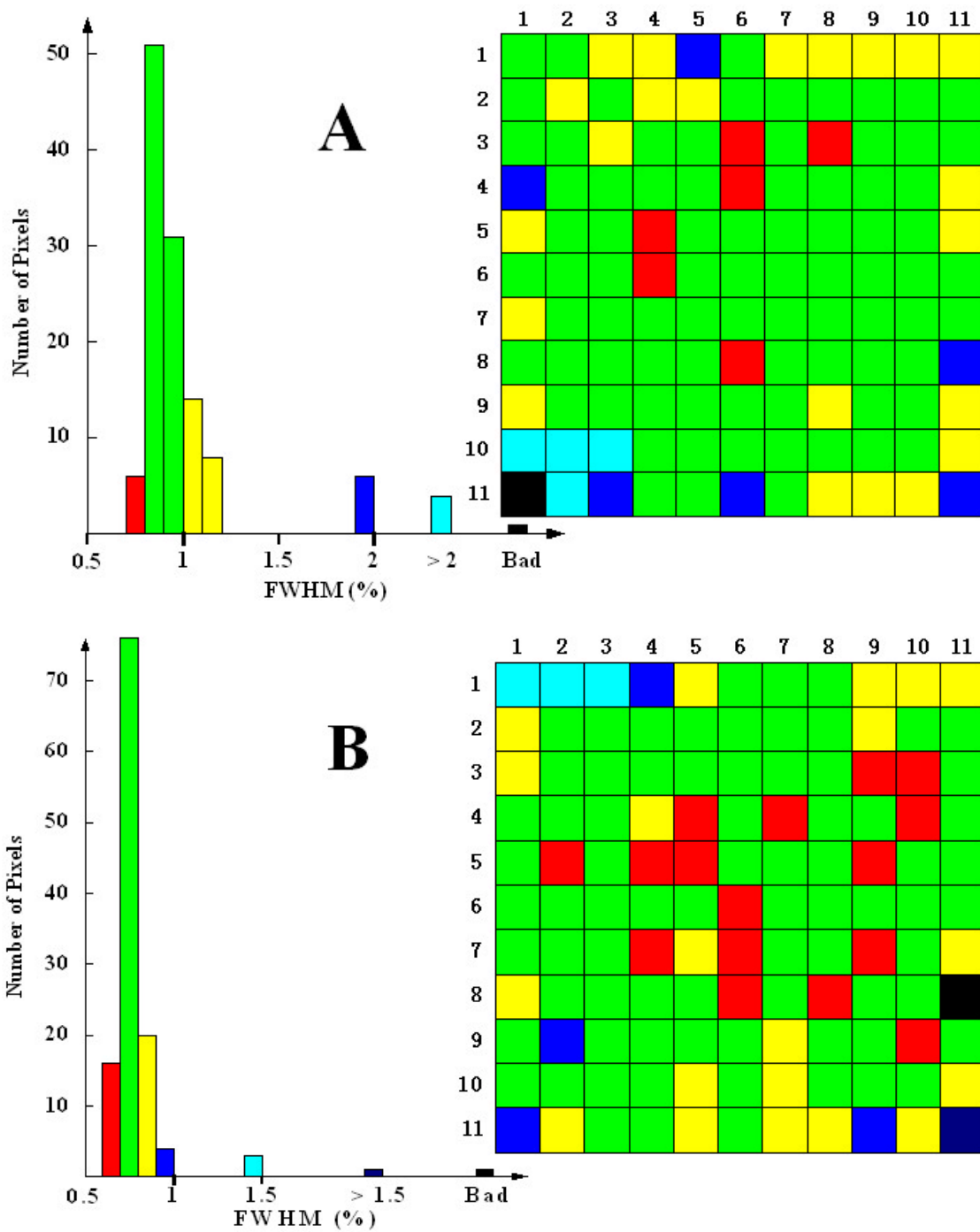
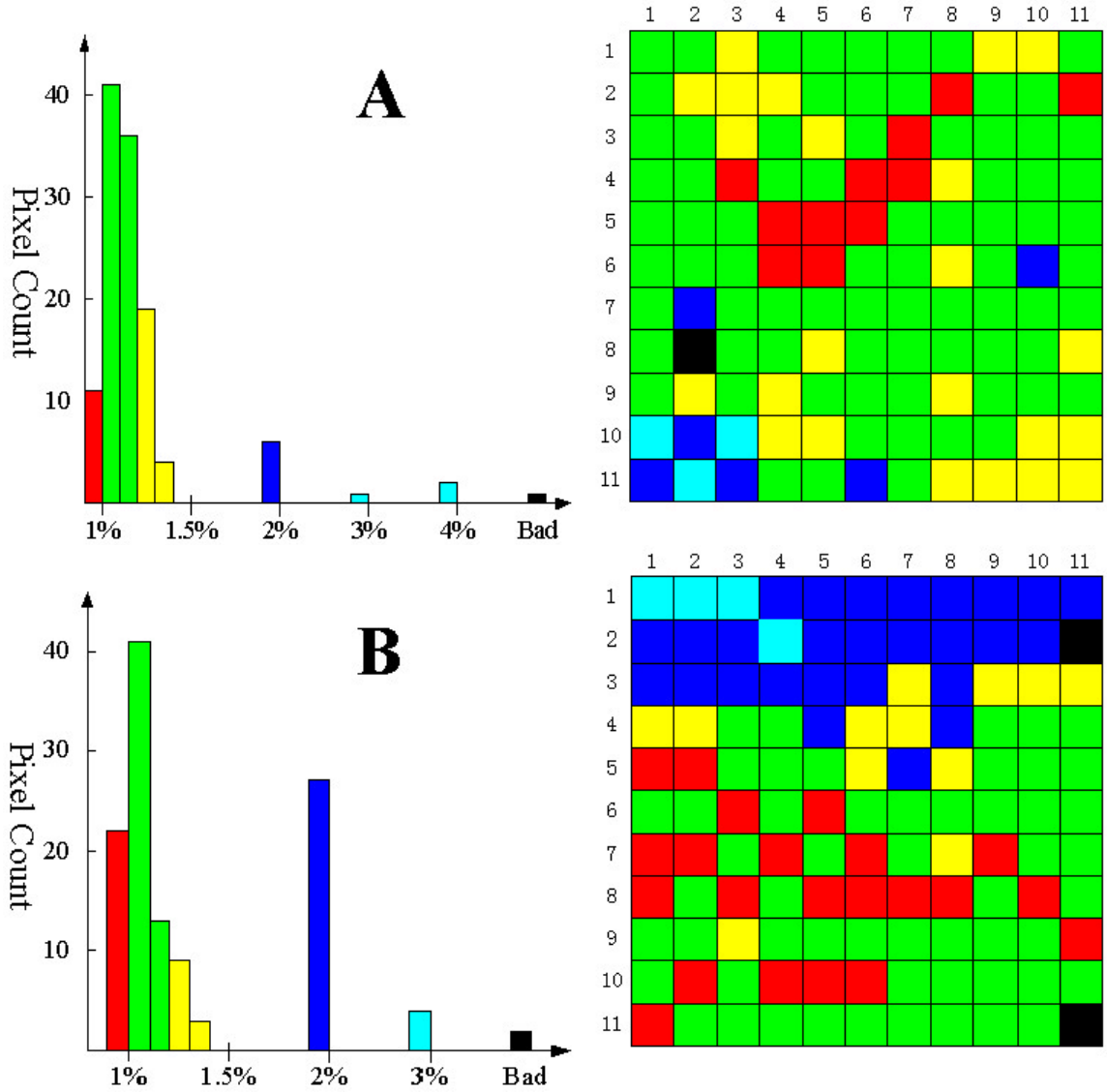Figure 6.9. Energy resolution distribution for single-pixel events from a ^{137}Cs source collected over 40 hours for (A): Detector #2.2 and VAS3.1/TAT3 system, (B): Detector #2.3 and VAS3.1/TAT3 system.

By comparing Figure 6.2(B) and Figure 6.9(B), we can conclude that the bad region (top three rows) of detector #2.3, when it was read out by the VAS2/TAT2 system, was not due to the detector itself but some problem in the electronics. However, the four pixels in the upper-left corner have worse than average response in both systems, indicating some material or surface problem in that corner region.

6.2.3 Energy resolution for multiple-pixel events

After the correction for timing-amplitude-walk, electron trapping and non-linearity for each signal, the true energy and 3-D position information can be obtained for each interaction of multiple-pixel events. An energy resolution of 1.24% FWHM at 662 keV has been achieved for two pixel events collected from the entire volume of detector #2.3, as shown in Figure 6.10.
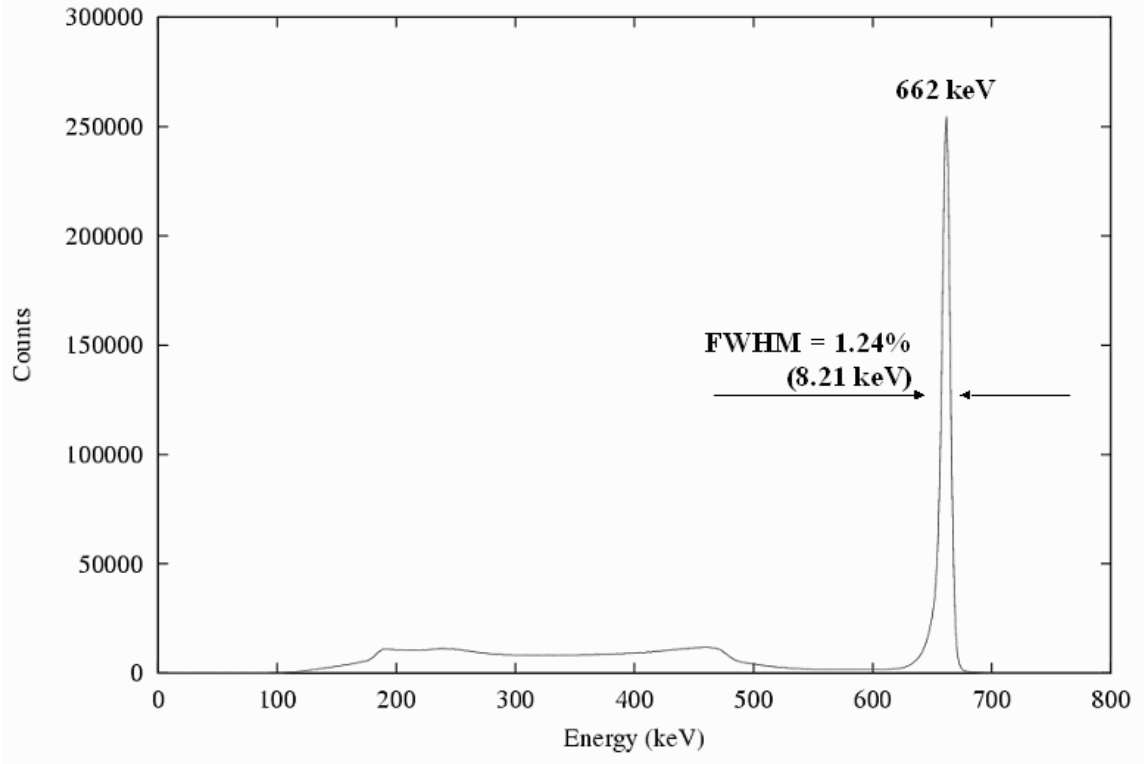
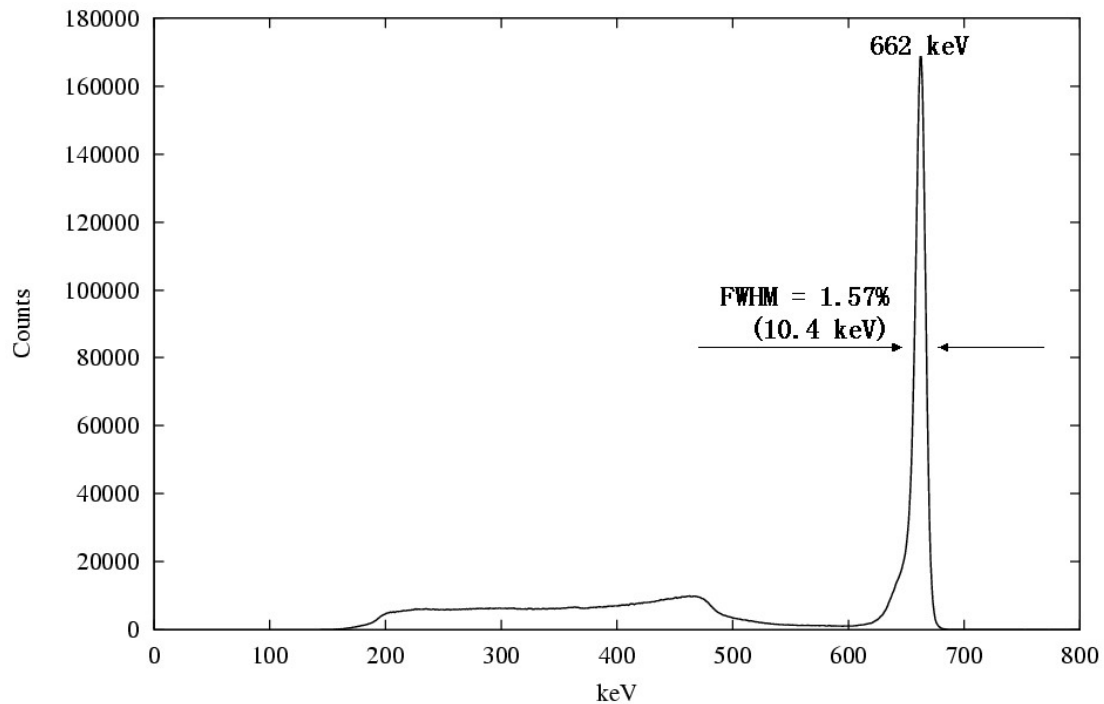Figure 6.10. Two-pixel events energy spectrum from a ^{137}Cs source collected for 40 hours from all working pixels in detector #2.3+VAS3.1/TAT3 system.

The energy resolutions for both detectors are summarized in Table 6.2. Both detectors have achieved better than 1% FWHM resolution for single-pixel events. The resolutions for two-pixel events are also better than those of the VAS2/TAT2 system, but are worse than expected given the excellent resolution for single-pixel events. The results for three-pixel and four-pixel events are even worse than with the VAS2/TAT2 system, indicating some problem inherent in the VAS3.1/TAT3 system.

Table 6.2. Energy resolution (FWHM) at 662 keV for single-pixel events and multiple-pixel events from the whole bulk of two detectors read out by VAS3.1/TAT3.

Detector	Single-Pixel Events	Two-Pixel Events	Three-Pixel Events	Four-Pixel Events
#2.2 biased at -2200 V, -65 V	0.93% (6.16 keV)	1.46% (9.67 keV)	2.42% (16.0 keV)	3.11% (20.6 keV)
#2.3 biased at -2000 V, -60V	0.78% (5.16 keV)	1.24% (8.21 keV)	2.17% (14.4 keV)	2.89% (19.1 keV)

6.2.4 Factors degrading the energy resolution for two-pixel events

If we take detector #2.2 as an example, although an energy resolution of 0.93% FWHM at 662 keV has been achieved for single-pixel events, the energy resolution for two-pixel events was only 1.46% FWHM, worse than the conservatively estimated energy resolution based on single-pixel resolution $- \sqrt{(0.93\%)^2 + (0.93\%)^2} = 1.32\%$ FWHM. We can analyze the factors affecting the energy resolution for two-pixel events in more details.

First, we have estimated the electronic noise to be less than 4.5 keV. Let us take 4.5 keV as a conservative estimate. The electronic noise from both pixels will contribute

to the energy resolution degradation, at estimated amplitude of $\sqrt{4.5^2 + 4.5^2} = 6.4$ keV by assuming that the noises are not correlated.

Secondly, due to the timing resolution of 20 ns FWHM at 662 keV and a maximum electron drift time of ~500 ns, the depth resolution from electron drift time is ~0.4 mm FWHM. Thus, the uncertainty in the depth will contribute an uncertainty of 4% to the depth correction. The total change of the photopeak centroid over the whole thickness (1 cm) of the detector is ~7%. Therefore, the uncertainty in the depth corrected energy due to depth resolution is 4% $\times$ 7% $\times$ 662 keV = 1.86 keV.

Thirdly, the depth resolution for single-pixel events is ~0.2 mm FWHM and thus ~2% uncertainty in the depth correction – 2% $\times$ 7% $\times$ 662 keV = 0.93 keV. The contribution of factors other than the electronic noise and the depth uncertainty is $\sqrt{(0.93\% \times 662)^2 - 4.5^2 - 0.93^2} = 4.1$ keV.

Then, by adding all these known factors, we can get an estimation of the energy resolution for two-pixel events - $\sqrt{6.4^2 + 1.86^2 + 4.1^2} = 7.82$ keV FWHM or 1.2% FWHM. This is far better than the experimental result of 1.46% FWHM. There must be some other factors in an amount of $\sqrt{(1.46\% \times 662)^2 - 7.82^2} = 5.7$ keV FWHM contributing to the energy resolution degradation for two-pixel events. Two possible factors, charge sharing and non-linearity, have been investigated.

6.2.4.1 Charge sharing

Because the finite electron cloud size (~220 μm at 662 keV) is comparable to the 1.27 mm pixel pitch, the possibility for one electron cloud being created near the pixel boundary and shared by two pixels is fairly high. This charge sharing makes an actual single-interaction event to appear as a two-pixel event. Some charges may be collected by the grid or be trapped in the gap between the pixel and the grid, resulting in a loss in the

collected signal. In addition the weighting potential cross-talk effect will be the strongest for such events.

Table 6.3 shows the energy resolution and the photopeak counts for selected two-pixel events from the two detectors. The two-pixel events fitting the selection criteria that the two interactions occur in neighboring pixels with a depth separation smaller than 1 mm are probably charge-sharing events. We can see that almost one third of all two-pixel 662 keV photopeak events are charge sharing events, consistent with the modeling results in Chapter 3. If charge sharing is a major reason for the energy resolution degradation of two-pixel events, we should see much worse energy resolution for these charge-sharing events. However, the energy resolutions for non-neighboring, neighboring and charge-sharing events are almost the same. Therefore, charge sharing is not the reason.

Table 6.3. Comparison of selected two-pixel events.

		All	Non-neighboring	Neighboring	Neighboring and $\Delta d < 1.0$ mm
Detector #2.2	FWHM (%)	1.46	1.45	1.47	1.46
	Photopeak counts ($\times 10^6$)	1.98	0.87	1.11	0.61
Detector #2.3	FWHM (%)	1.24	1.25	1.23	1.21
	Photopeak counts ($\times 10^6$)	2.65	1.13	1.52	0.91

6.2.4.2 Non-linearity

For multiple-pixel events, the reconstructed total energy is the sum of the reconstructed energies of different amount from several pixels. Non-linearity in the system response can result in significant variation in the reconstructed total energy and degrade the energy resolution for multiple-pixel events. The VAS2/TAT2 system has significant non-linearity and the energy resolutions for multiple-pixel events have been

greatly improved after the non-linearity correction. The linearity of the VAS3.1/TAT3 system was verified to be much better than the VAS2/TAT2 system. Good energy resolutions for multiple-pixel events have been achieved from the VAS3.1/TAT3 system without doing any non-linearity correction. Non-linearity calibration with multiple gamma ray sources had been performed and could not improve the energy resolution. However, the small-scale fluctuation in the system linear response, if any, cannot be revealed by a few discrete calibration points, yet it can degrade the energy resolution for multiple-pixel events.

The DAQ program was modified to do a fine linearity scan for the VAS3.1/TAT system using the method discussed in Chapter 5. The noise in the test pulse response is ~7 ADC Channel (~6 keV FWHM). The step of the test pulse was set to 2 mV per step (~5 keV) and 100 pulses were used for each step. The differential responses of one typical channel at two different measuring times are shown in Figure 6.11.
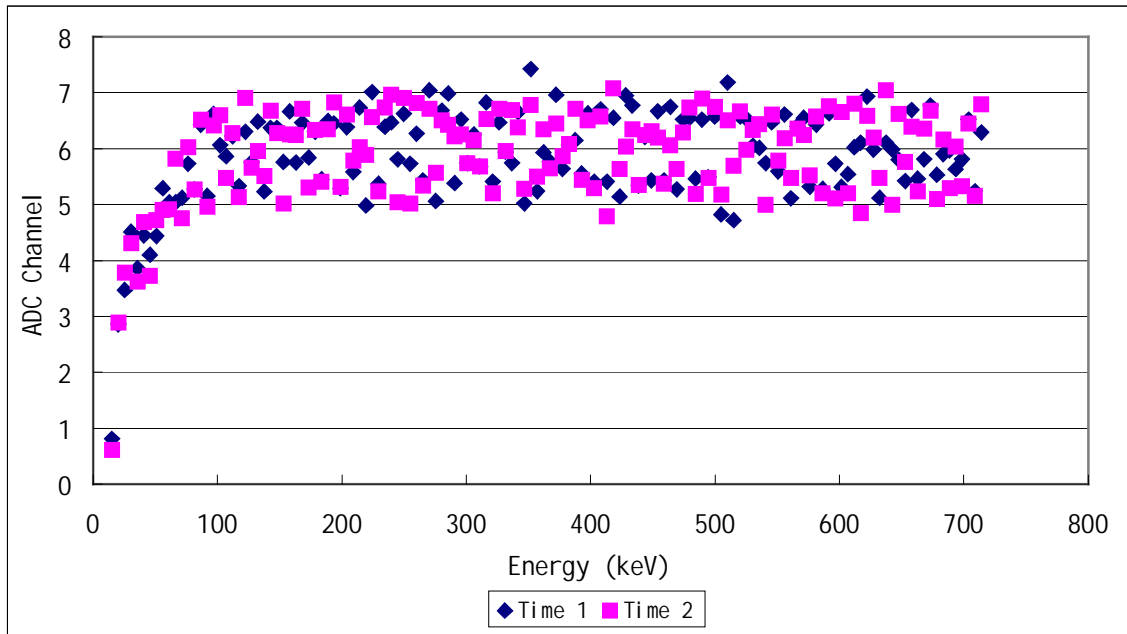
Figure 6.11. Differential VAS3.1 output (the increment in the output for each fixed and equal increment in the test pulse amplitude) vs. test pulse amplitude for channel #5 at two different measuring times.

121

Non-linearity is observed at the low energy side (< 80 keV), but has been verified to have only 0.02% degradation effect probably due to the small fraction of the events in this low energy region. Most energy range is quite linear. There are still some fluctuations in the differential response - ~1.4 ADC Channels FWHM or ~1.25 keV FWHM. However, if we add two signals together, the fluctuation only adds to ~1.76 keV FWHM. This is still much smaller than the ~6 keV FWHM unknown factors that degrade the energy resolution for two-pixel events. If we consider that only 100 samples are used for each test pulse amplitude step, the true fluctuation should be even smaller. Therefore, non-linearity is unlikely the major reason for the energy resolution degradation of multiple-pixel events in the VAS3.1/TAT3 system.

The problem of energy resolution degradation for multiple-pixel events remains to be resolved.

6.2.5 Energy spectrum for a sample of uranium ore

The VAS3.1/TAT3 system has a dynamic range up to ~1.5 MeV, limiting its ability to detect high-energy gamma rays if only single-pixel events can be utilized. With its ability of reconstruct multiple-pixel events, the 3-D CdZnTe spectrometer should be able to detect gamma rays of energy much higher than the dynamic range of one channel. In order to examine 3-D CdZnTe spectrometer's ability of detecting high-energy gamma rays, such as the 2.6 MeV gamma ray from the ^{208}Tl decay (a daughter product of ^{235}U), events from a sample of uranium ore were collected using a calibrated VAS3.1/TAT3 system. The spectra are shown in Figure 6.12. The single-pixel events spectrum clearly shows that the dynamic range of the VAS3.1/TAT3 is ~1.5 MeV. The ~1.1 MeV photopeak in which NASA is interested can be clearly identified in all spectra, although

the energy resolution of the four-pixel events spectrum still needs improvement. The 2.6 MeV photopeak can barely be identified in the four-pixel events spectrum.
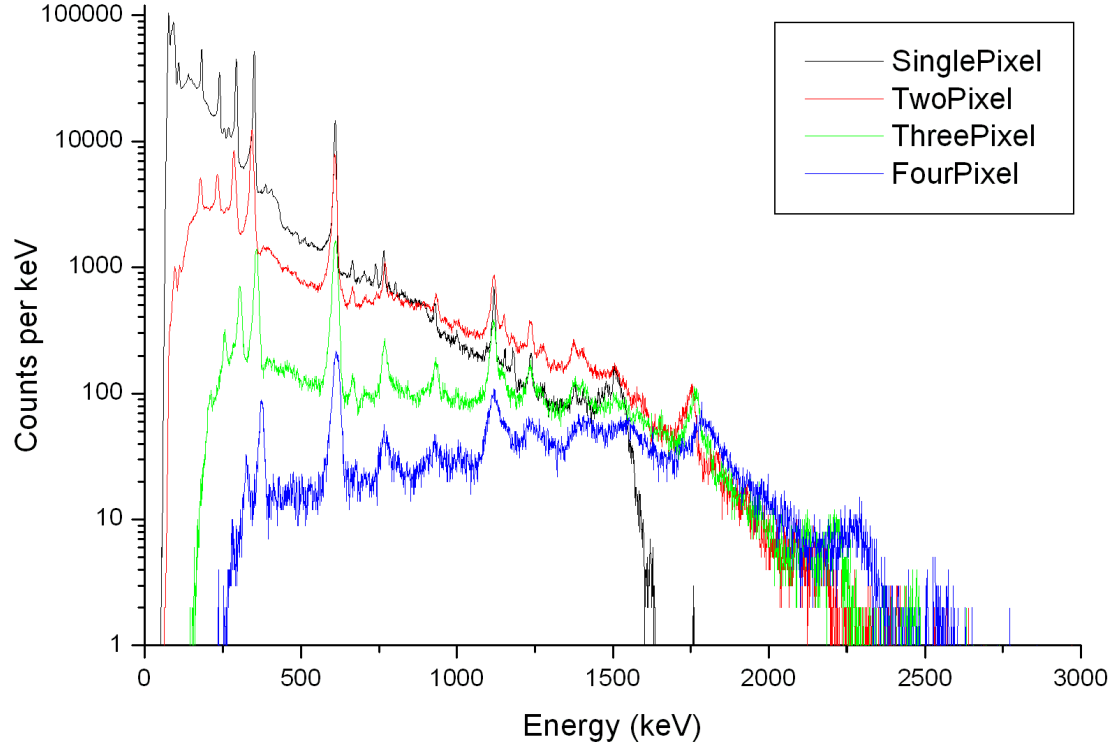
Figure 6.12. Energy spectra of a sample of uranium ore collected for 24 hours using detector #2.2 and the VAS3.1/TAT3 system.

6.3 Electron mobility-lifetime product

Using the photopeak events occurring near the cathode under two different cathode biases, $(\mu\tau)_e$ was measured for each pixel of detector #2.2 and #2.3. The results are shown in Figure 6.13 and 6.14. The mean value of $(\mu\tau)_e$ is ~3.22×10^{-3} cm^2/V for detector #2.2 with a standard deviation of 0.22×10^{-3} cm^2/V. The mean value of $(\mu\tau)_e$ is ~6.79×10^{-3} cm^2/V for detector #2.3 with a standard deviation of 0.51×10^{-3} cm^2/V. The

mean $(mt)_e$ of detector #2.3 is more than two times that of detector #2.2, indicating much better electron transportation properties in detector #2.3.

The correlation between the energy resolution and $(mt)_e$ for a given pixel was calculated to be -0.06 and 0.4 for detectors #2.2 and #2.3 respectively. The numbers indicate that there is some correlation between the better energy resolution and the higher $(mt)_e$ for detector #2.3, but no correlation for detector #2.2. Higher $(mt)_e$ might lead one to predict better performance from detector #2.3, which was indeed observed. These results may suggest some subtle differences in the quality of the detector materials. However, it is hard to make any conclusion without the information about the original crystals, such as the size of the tellurium inclusions and any twins or grain boundaries.
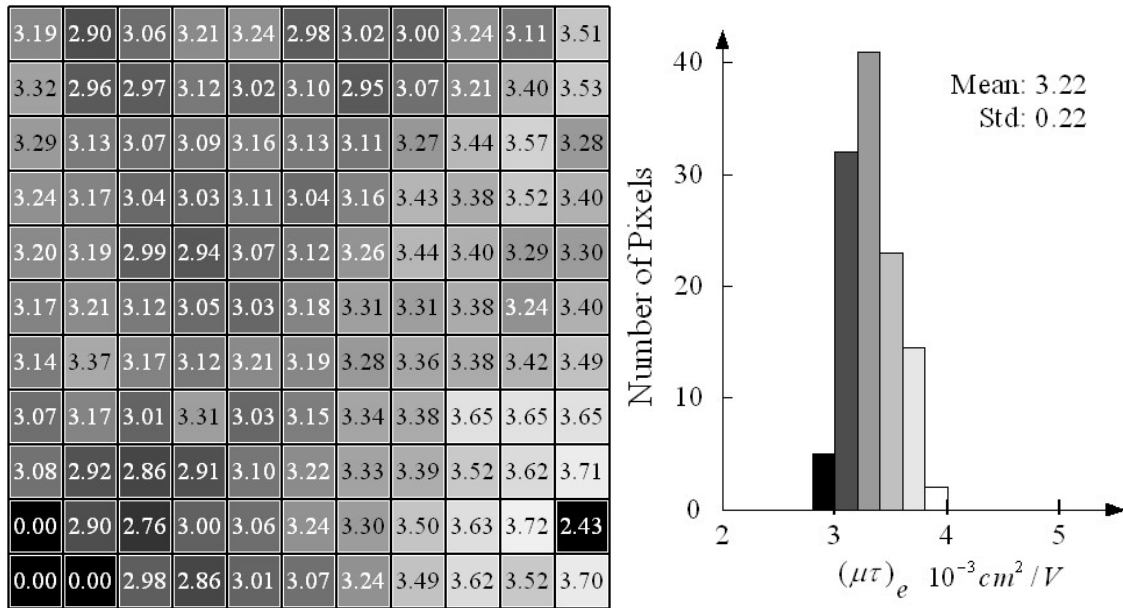
Figure 6.13. Experimental results of the electron mobility-lifetime product (10^{-3} cm^2/V) for all the pixels of detector #2.2. (a): Pixel map of the $(mt)_e$ value. Darker color corresponds to lower $(mt)_e$. (b): Histogram of the $(mt)_e$ distribution for all the pixels.

7.82	7.83	7.66	8.09	7.83	7.56	7.35	7.57	7.43	6.79	7.18
7.88	7.35	7.54	7.66	7.43	7.10	7.33	6.72	6.78	6.72	6.74
7.27	7.73	7.38	7.33	7.26	7.25	7.19	7.06	6.71	6.83	6.52
7.45	7.14	6.96	6.83	6.86	7.03	6.77	6.89	6.70	6.74	6.36
7.36	7.04	6.95	6.76	7.53	6.79	6.83	7.03	6.90	6.52	6.52
7.01	7.00	6.62	7.20	6.95	7.12	6.91	6.40	6.68	6.66	6.33
7.12	6.57	7.10	6.62	7.23	6.83	6.71	6.78	6.51	6.39	6.32
6.45	6.61	6.92	6.82	6.81	6.60	6.51	6.29	5.92	6.23	0.00
6.88	6.72	6.67	6.77	6.55	6.57	6.70	6.39	5.89	6.31	5.89
6.45	6.19	6.37	6.32	6.27	6.46	5.99	6.22	6.12	5.92	5.57
6.58	6.23	6.36	6.04	6.01	6.30	6.10	5.96	6.00	5.84	0.00

Figure 6.14. Experimental results of the electron mobility-lifetime product (10^{-3} cm^2/V) for all the pixels of detector #2.3. (a): Pixel map of the $(\mu\tau)_e$ value. Darker color corresponds to lower $(\mu\tau)_e$. (b): Histogram of the $(\mu\tau)_e$ distribution for all the pixels.

CHAPTER 7

FACTORS AFFACTING THE DETECTOR RESPONSE

With the help of the 3-D position sensitivity, spatial variations in the detector response and spectroscopic performance have been observed from both detectors. To study the spatial variations in the detector response, single-pixel events are collected from the whole detector volume and analyzed. Although both the C/A ratio and the electron drift time can be used for single-pixel events, due to limited timing resolution (~20 ns), the depth resolution using the electron drift time was estimated to be ~0.5 mm. The C/A ratio depth sensing method achieved ~0.25 mm depth resolution at 662 keV, and thus was chosen for this study. This 3-D position sensing technique divides the whole volume of the detector into $11 \times 11 \times 40$ voxels. Individual spectra from each voxel can be retrieved from these 3-D CdZnTe spectrometers. The effects on photopeak centroids, photopeak counts and energy resolution due to electron trapping, ionization energy and weighting potential can then be studied down to the limit of the position resolution. Such analysis of the 3-D detector response can be used to identify possible defects in the detector and to assess the quality of the crystal and the detector fabrication.

7.1 Electron Trapping

When a gamma ray interacts inside a CdZnTe detector, electron-hole pairs are generated. Since the cathode is biased at -2000 V and the anode pixels are at virtual ground, the electrons drift towards the anode, while the holes drift towards the cathode. Because of their poor mobility and lifetime, the holes don't contribute to the signals

during the 1 • s electron collection time. The signals on both the cathode and the anode pixel are only dependant on the movement and collection of the electrons. Due to the small pixel effect [27], the signal on the anode pixel is nearly independent of the interaction depth and only proportional to the number of electrons collected, while the signal on the cathode is dependent on the interaction depth. Thus, for single-pixel events, the ratio of the cathode signal to the anode signal can be used to determine the interaction depth. However, the C/A ratio depth can be affected by electron trapping.
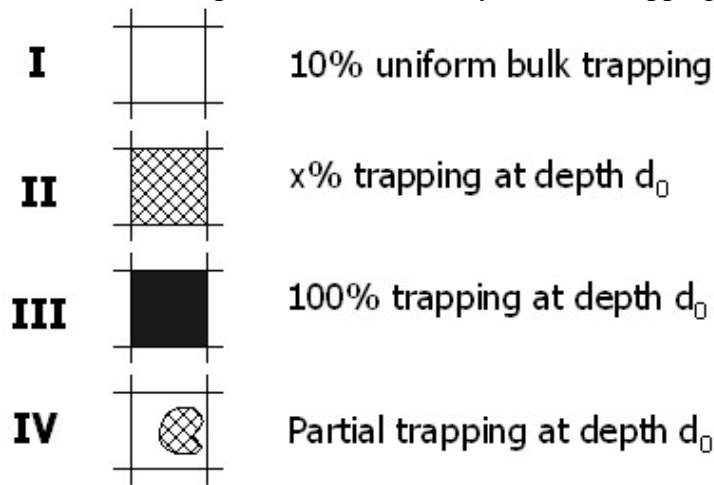
Figure 7.1. Four different cases of electron trapping discussed in this study.

Figure 7.1 shows an illustration of the four trapping cases considered in this study. Case I is a normal pixel with 10% uniform bulk electron trapping along the whole depth under this pixel. Case II is a pixel with an electron trapping defect at depth d_0 and all electrons under this pixel passing through this defect will be trapped by a certain percentage. Case III is a pixel with a severe electron trapping at depth d_0 that all electrons will be trapped. Case IV is a pixel with an electron-trapping defect smaller than the pixel size at depth d_0. The experimental results from typical pixels of these four different trapping cases are presented in Figure 7.2, Figure 7.5, Figure 7.6, and Figure 7.7 respectively, and discussed in the following subsections.

127

7.1.1 Case I: 10% uniform bulk trapping

In case I, because of the bulk electron trapping the electrons will contribute to the cathode signal before they are trapped, while these trapped electrons won't contribute to the anode signal. Therefore, the C/A ratio will have a certain systematic shift over most of the interaction depth as discussed in [71]. However, the relation between the C/A ratio and the true depth should be linear over most of the interaction depth.
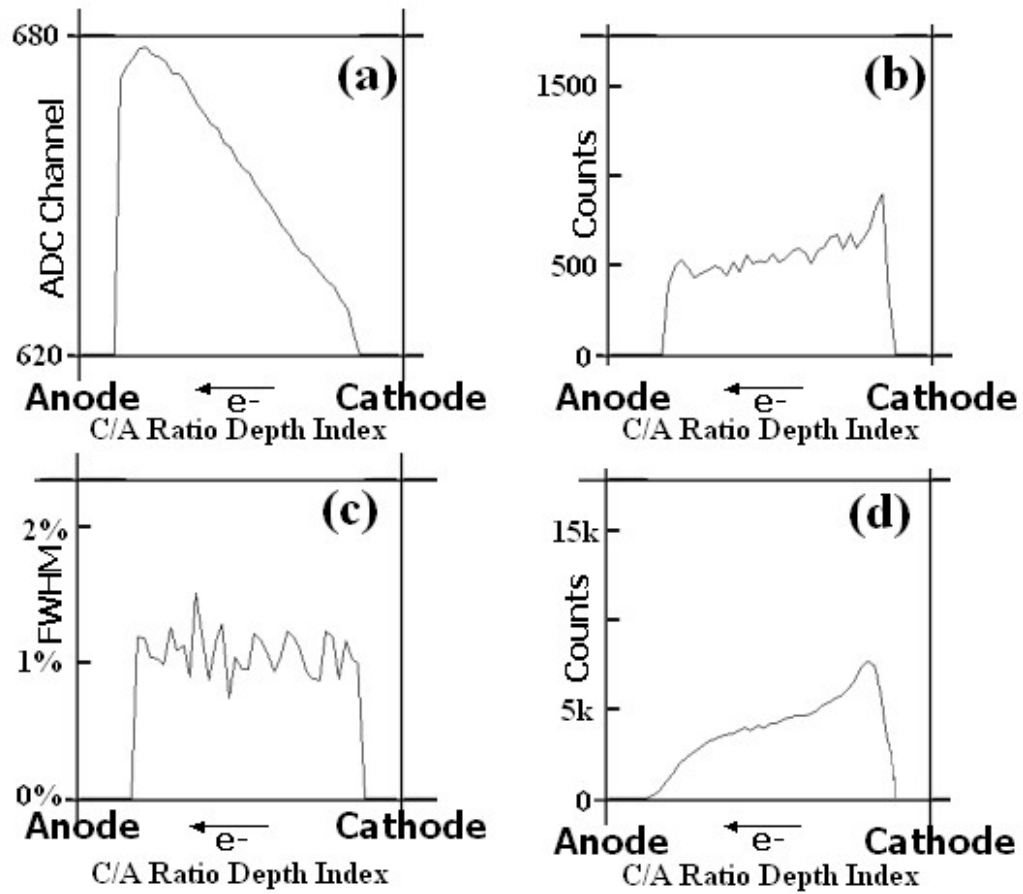
Figure 7.2. Experimental results from one normal pixel, case I of Figure 7.1. (a): Anode spectra photopeak centroid vs. C/A ratio depth, please note that the y-axis is offset from 0 and the actual change in the photopeak centroids is only ~6%; (b): Photopeak counts vs. C/A ratio depth; (c): Anode spectra FWHM at 662 keV vs. C/A ratio depth; (d): Total counts vs. C/A ratio depth.

To observe the changes in the photopeak centroids, in the photopeak counts and in the total counts for different pixels and different interaction depths, an uncollimated 10 •Ci ^{137}Cs source was placed 5 cm from the cathode surface. Sorted by the pixel location and the interaction depth derived from the C/A ratio, the collected single-pixel events were recorded in ~4800 energy spectra for each voxel corresponding to a volume of 1.27 mm × 1.27 mm × 0.25 mm within each detector. Since most voxel spectra have very sharp photopeaks (~1.0% FWHM at 662 keV), the 662 keV photopeak can be easily located, and the photopeak centroid, the energy resolution, the photopeak count and the total count are measured for each voxel spectrum.

As can be seen from Figure 7.2(a), for normal pixels having no defects but only bulk electron trapping, the photopeak centroid decreases smoothly from the anode to the cathode due to uniform electron trapping. In Figure 7.2(b) and Figure 7.2(d), the decrease in the counts from the cathode side to the anode side is expected, because the detector was irradiated from the cathode side. The FWHM from all depths remains nearly unchanged despite some statistical fluctuation, as shown in Figure 7.2(c).

7.1.2 Case II: a x% trapping defect at depth d_0

In case II, there is a trapping center at depth d_0 which traps x% of the electrons passing through it. Let us simplify the situation by not considering the bulk electron trapping and assuming ideal weighting potential that the weighting potential remains zero from the cathode surface (d = 1) to the anode (d = 0), then rises from zero to 1 on the anode surface. Then,

for $d < d_0$,
$$\frac{C}{A} = \frac{d \times N_0 e}{N_0 e} = d \tag{7.1}$$

for $d \geq d_0$,
$$\frac{C}{A} = \frac{(d - d_0) \times N_0 e + (1 - x\%) \times N_0 e \times d_0}{(1 - x\%) \times N_0 e}$$

$$= \frac{d - d_0}{1 - x\%} + d_0 = \frac{1}{1 - x\%} \times d - \frac{x\%}{1 - x\%} \times d_0 \tag{7.2}$$

where N_0 is the original number of electron-hole pairs created by the gamma-ray interaction, and d is the interaction depth.

As a result of Equation 7.2, the C/A ratio between depth d_0 and the cathode will be larger than normal because the cathode signal is larger than the corresponding anode signal due to the electron-trapping defect at depth d_0, and those events close to the cathode will have a calculated C/A ratio even larger than 1.0, as we can see from Figure 7.3. This change in the C/A ratio depth relation with the actual depth will affect the photopeak centroid and photopeak count as a function of the C/A ratio depth.
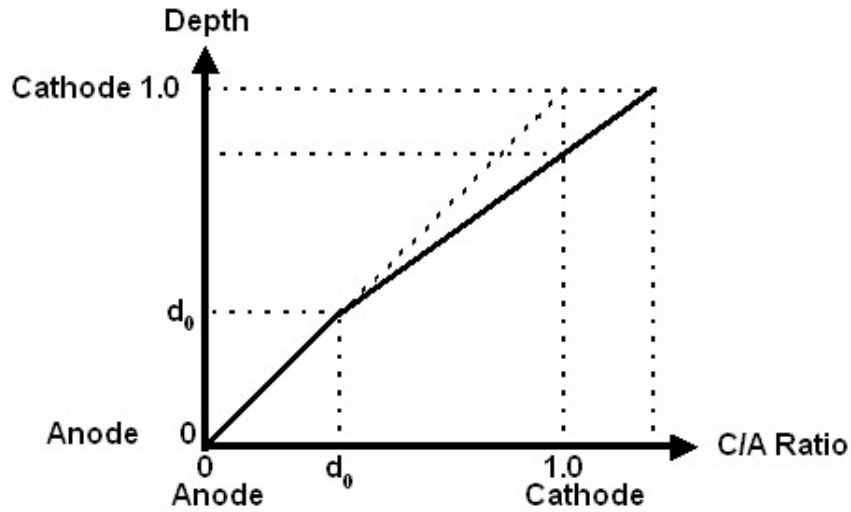
Figure 7.3. Illustration of the relation between the true depth and the C/A ratio when there is a trapping defect.

As shown in Figure 7.4(a), the relation between the normalized photopeak centroid as a function of the C/A ratio depth will have an abrupt change at the defect depth d_0. In the real data, this change may be smoothed out by other factors such as finite depth resolution. But the change of slope in the relation is still present. If one still takes C/A ratio = 1.0 as the cathode and only selects the events with C/A ratio values varying from 0 to 1.0 for the electron trapping analysis, the events from near the real cathode side

130

$(1.0 - 1.x)$ are discarded. This results in underestimation in the calculated electron trapping.
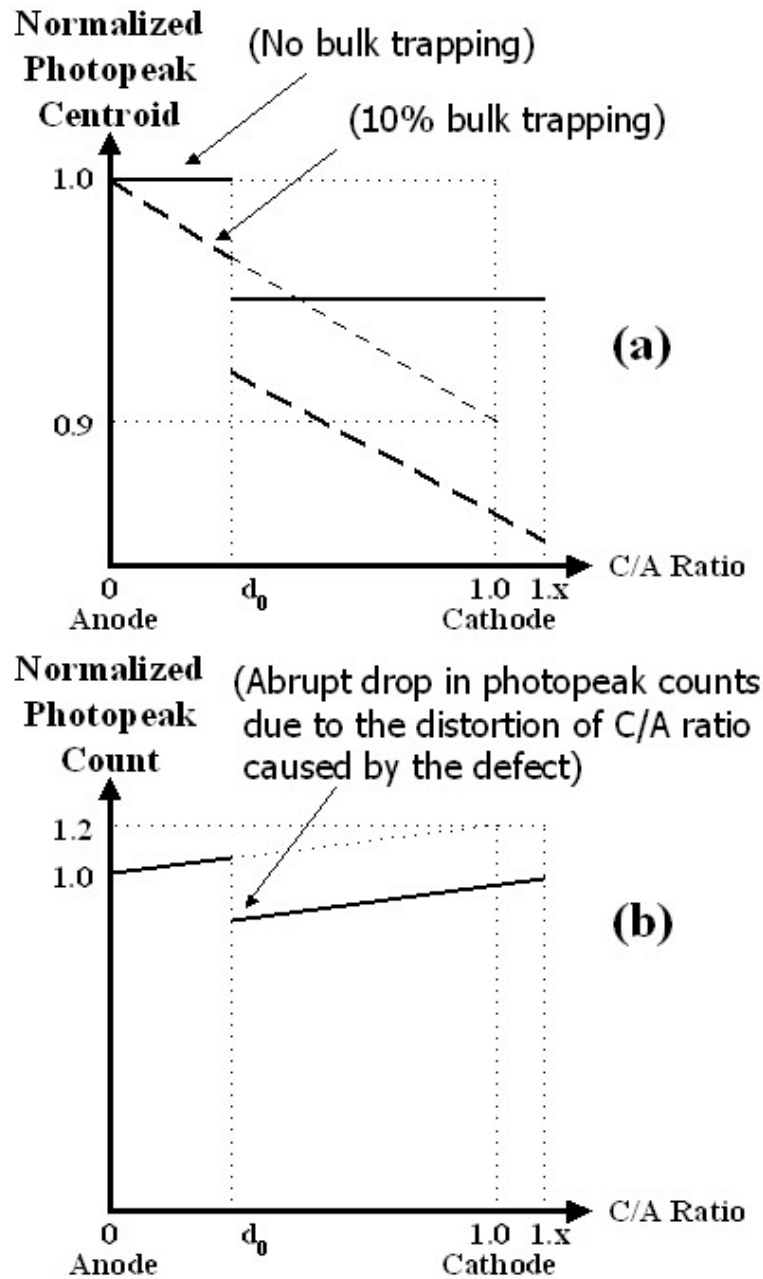
Figure 7.4. If there is a trapping defect at depth d_0, (a): The relation between the normalized photopeak centroid and the C/A ratio; (b): The relation between the normalized photopeak counts and the C/A ratio.

Figure 7.4(b) shows that the relation between the normalized photopeak counts versus the C/A ratio depth has an abrupt change and the photopeak counts between the cathode and the defect depth d_0 will be lower than what would be observed without the defect, because the thickness of the region between depth d_0 and the cathode derived from the C/A ratio ($d_0 - 1.0$) is thinner than the thickness of the real depth region ($d_0 - 1.x$).
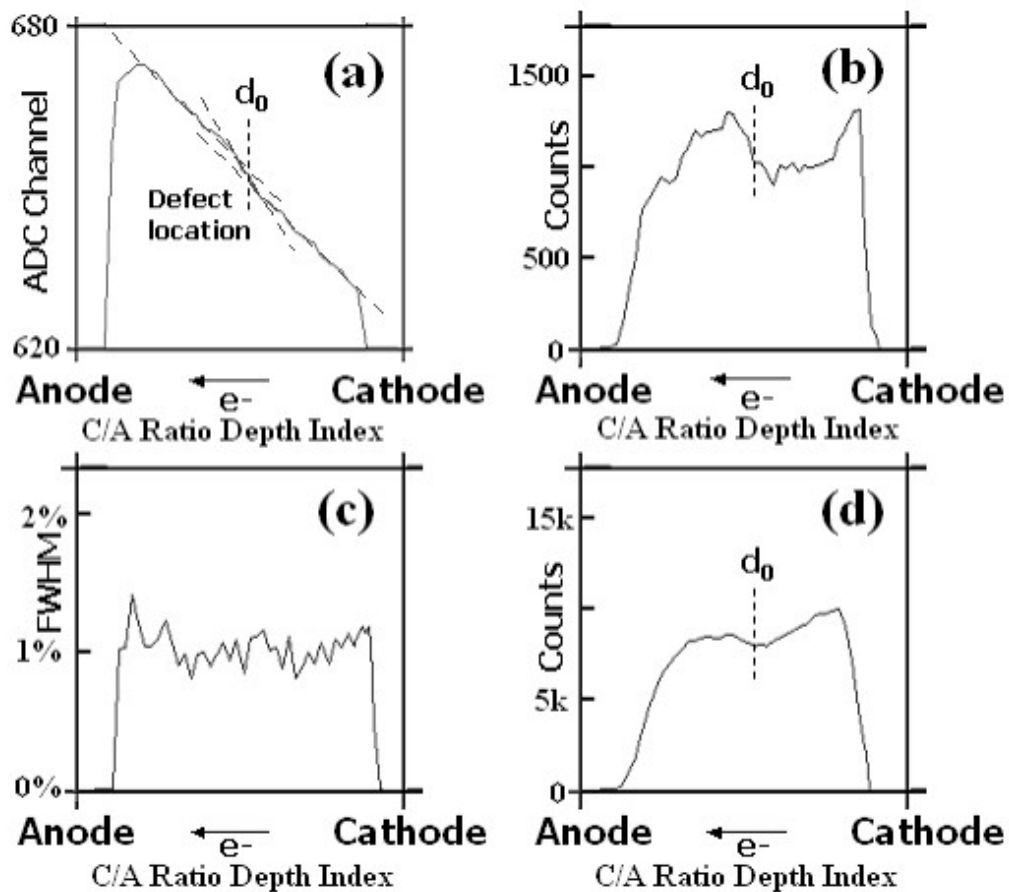
Figure 7.5. Experimental results from one pixel with electron trapping defect, case II of Figure 7.1. (a): Anode spectra photopeak centroid vs. C/A ratio depth; (b): Photopeak counts vs. C/A ratio depth; (c): Anode spectra FWHM at 662 keV vs. C/A ratio depth; (d): Total counts vs. C/A ratio depth.

Figure 7.5 shows a pixel observed with such an electron trapping defect at a certain depth. The change of slopes in the photopeak centroid vs. the C/A ratio depth is not very prominent but still visible. The decreases in the photopeak counts, and in the total counts are quite clear. However, no significant degradation in the energy resolution can be observed.
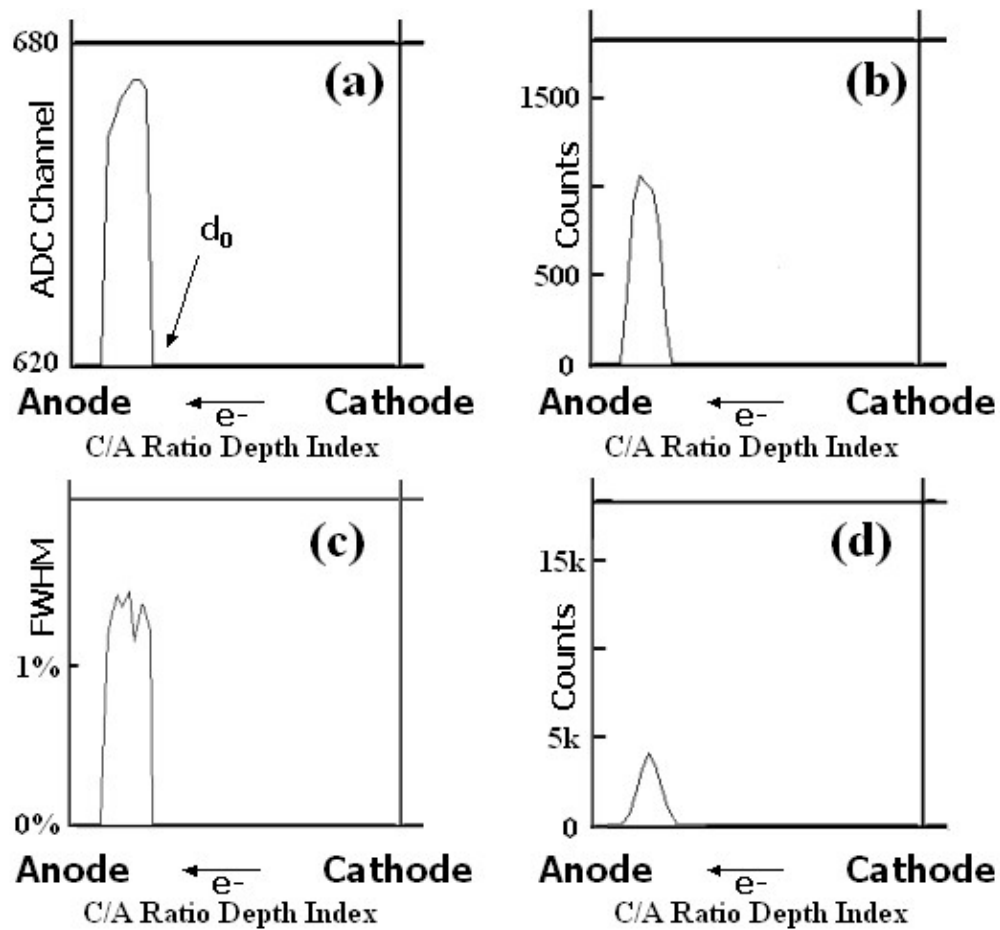
Figure 7.6. Experimental results from one pixel with defect that electrons cannot pass through, case III of Figure 7.1. (a): Anode spectra photopeak centroid vs. C/A ratio depth; (b): Photopeak counts vs. C/A ratio depth; (c): Anode spectra FWHM at 662 keV vs. C/A ratio depth; (d): Total counts vs. C/A ratio depth.

7.1.3 Case III: a 100% trapping defect at depth d_0

In case III, if there is a severe electron trapping defect at a certain depth under the pixel, all events that occur between this defect and the cathode cannot be recorded by the system. A pixel with such a defect is also observed and the photopeak centroids, the photopeak counts, the FWHM and the total counts are shown in Figure 7.6.

7.1.4 Case IV: a trapping defect smaller than the pixel size at depth d0

In case IV, if there is an electron trapping defect smaller than the pixel size at depth d_0, only part of the events occurring between depth d_0 and the cathode are affected by this defect. The change in the C/A ratio should be somewhat between case I and case II, and the change in the photopeak centroids and the photopeak counts will not be as evident as in case II. However, the photopeaks between depth d_0 and the cathode will be broadened because some events will have electron trapping and some will not. As a result, the energy resolution will degrade after depth d_0, as shown in Figure 7.7(c). Such a small electron trapping defect can significantly degrade the energy resolution of the corresponding pixel. However, with 3-D position sensing, those events affected by such a defect can be discarded.

Overall for both detectors, we observed quite smooth and consistent relationship between the photopeak centroid and the C/A ratio depth, and the relationship between the electron drift time and the C/A ratio depth for most of the pixels. This result indicates that both detectors have quite good material uniformity.
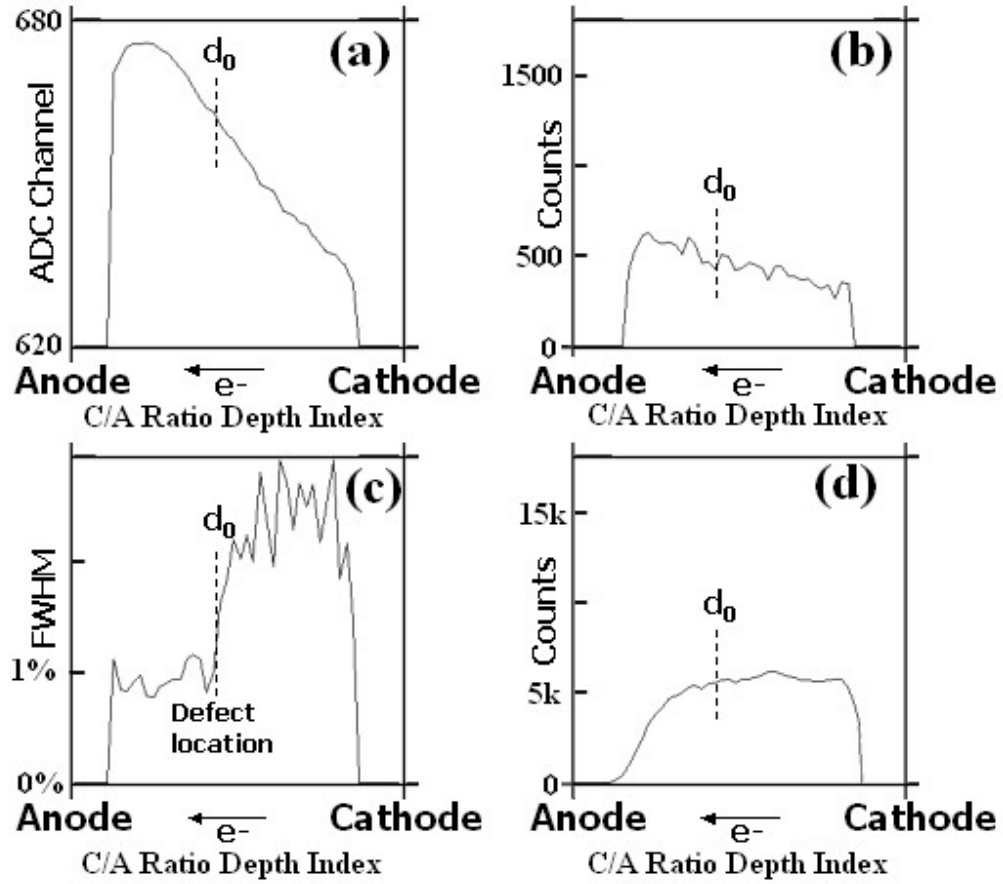
Figure 7.7. Experimental results from one pixel with a small size electron trapping defect, case IV of Figure 7.1. (a): Anode spectra photopeak centroid vs. C/A ratio depth; (b): Photopeak counts vs. C/A ratio depth; (c): Anode spectra FWHM at 662 keV vs. C/A ratio depth; (d): Total counts vs. C/A ratio depth.

7.2 Variation of Ionization Energy

As we showed in Equation 7.1-7.2 in the previous section, the C/A ratio is independent of the number of electrons generated, and thus independent of the variation of ionization energy. If the ionization energy changes along the depth underneath one pixel, the C/A ratio will not be affected and thus the photopeak counts will not be affected. However, if the ionization energy varies at different locations within the crystal, the number of electrons generated by the deposited energy will vary, and the photopeak

centroid may have non-smooth shape if the ionization energy changes in a scale comparable to or larger than the scale of the depth resolution, as shown in Figure 7.8(a). No such non-smooth shape in the photopeak centroid plots was observed in either detector. If the ionization energy changes in a scale smaller than the depth resolution, we may observe worse energy resolution at certain depths, as shown in Figure 7.8(b). Similarly, in the lateral direction, if the ionization energy changes in a scale comparable to or larger than the pixel size, we should observe large variations in the photopeak centroids among the pixels. If the ionization energy changes in a scale smaller than the pixel size, we should see worse energy resolution from the pixel.

However, if there is a surface defect underneath the pixel anode, which affects the collection of electrons onto the pixel anode, the signal from all depths will be affected and have worse energy resolution at all depths as shown in Figure 7.9. We cannot tell whether this degradation in energy resolution for all depths is due to the surface defect or due to the small-scale variation in ionization energy throughout all depths underneath this pixel as discussed in the previous paragraph and Figure 7.8(b).

Such defects were observed in detector #2.3 (except Figure 7.10, all other results in this Chapter are obtained from detector #2.2). As shown in Figure 7.10(a), all pixels have smooth relation between the photopeak centroid and the C/A ratio depth, no abrupt change in the curve. This indicates there is no large-scale variation in ionization energy. However, the pixel in the center have bad energy resolution for nearly all the depths, as can be seen in Figure 7.10(b). This is either due to surface defect or small-scale variation in ionization energy throughout all the depths under these pixels. Such performance degradation cannot be corrected even with 3-D position sensing. However, by discarding the events coming from the bad regions in the data processing and thus sacrificing the

active detector volume, the good energy resolution of the good regions can still be retained.
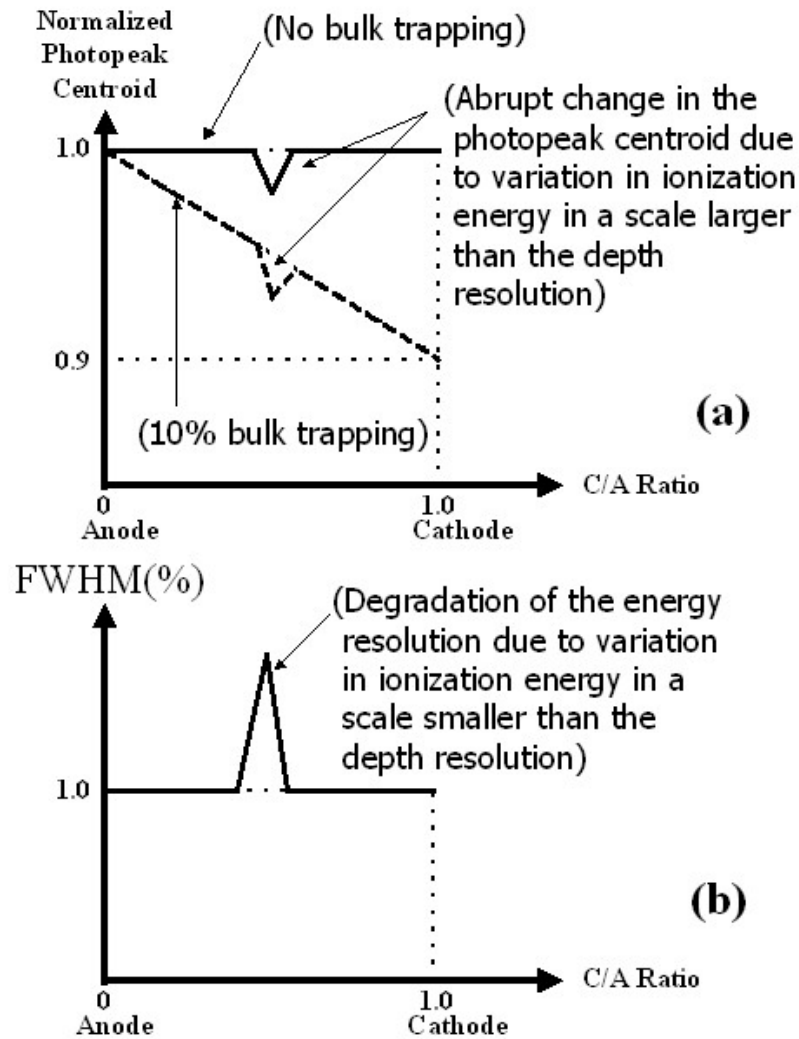
Figure 7.8. Illustration of the effect of variation in ionization energy. (a): The scale of variation is comparable to the depth resolution; (b): The scale of variation is much smaller than the depth resolution.
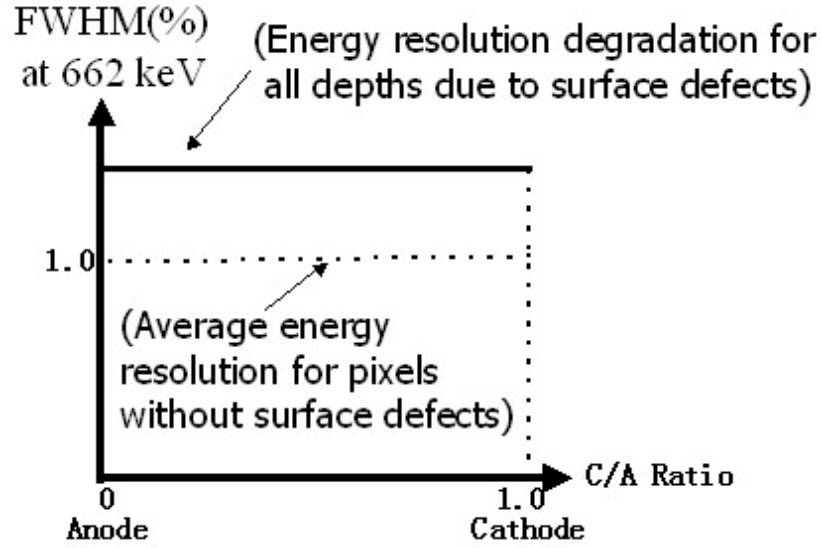
Figure 7.9. Illustration of the degradation in energy resolution for all depths due to surface defect.

For good pixels, the energy resolutions are around 1% for all the depths and the fluctuation of the FWHM is due to statistical variation. This shows that the bulk electron trapping/detrapping does not significantly degrade the energy resolution. Otherwise, the energy resolution should be worse on the cathode side because the electrons coming from the cathode side undergo more trapping/detrapping processes.

For VAS2/TAT2 systems, since the electronic noise is around 6 keV FWHM and the energy resolutions for good pixels are around 7 keV FWHM for all depths, we can also draw a conclusion that the small scale variation in the ionization energy, if any, should not exceed 0.5% FWHM for those good pixels - $\sqrt{7^2 - 6^2}/662 \cong 0.5\%$.
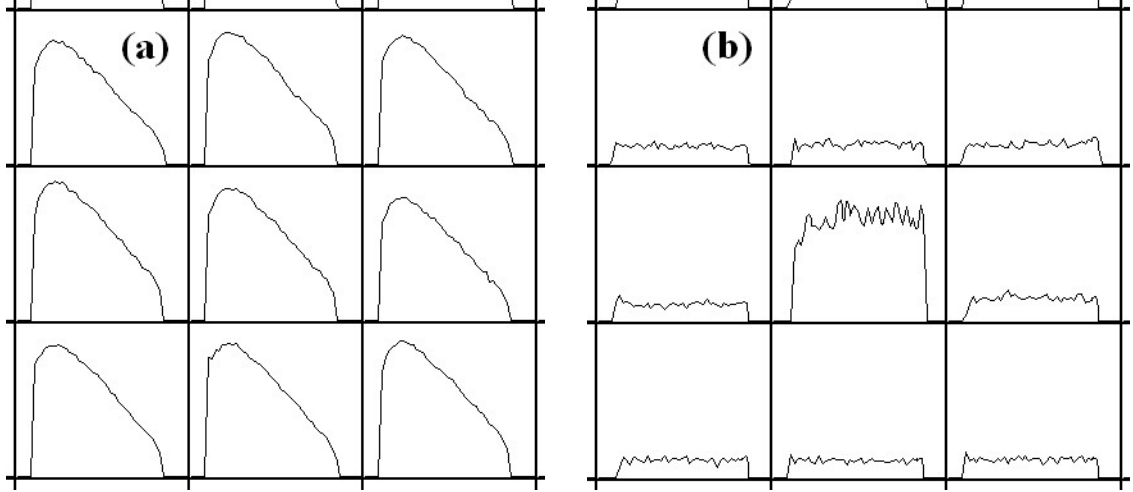
Figure 7.10. Experimental results for pixels in a region on detector #2.3. For each pixel, the x-axis is the C/A ratio depth index. (a): The relation between the anode photopeak centroid and the C/A ratio depth. For each pixel, the y-axis is photopeak centroid measured in ADC channel (origin not at 0); (b): The relation between the anode FWHM (%) and the C/A ratio depth. For each pixel, the y-axis is the energy resolution FWHM at 662 keV in units of percentage with a minimum at 0% and a maximum at 8%.

7.3 Weighting Potential

For pixels on the periphery and at corners of the anode surface, weighting potential is an important factor for the detector response. Due to the change in weighting potential for the pixels near the edge, the events coming from the anode side will have smaller signal than for central pixels, while the events coming from the cathode side remain the same, as can be seen in Figure 7.11(a). As a result, the photopeak centroids shown in Figure 7.11(b) seem to have smaller change from the anode to the cathode because the larger change in weighting potential (from the anode side to the cathode side) compensates the signal loss due to the electron trapping.

139
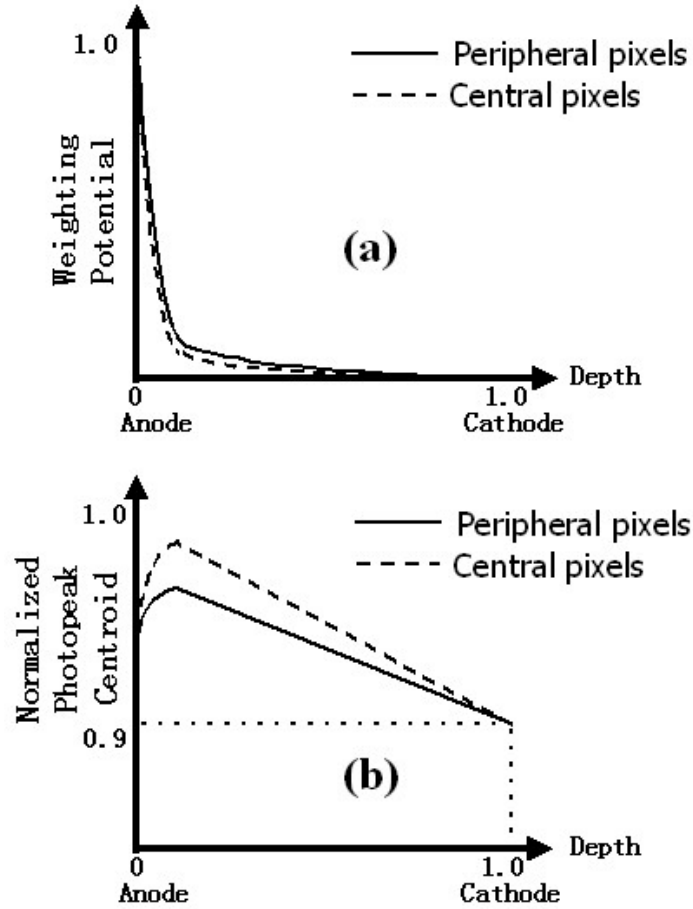
Figure 7.11. Simulation results of the effect of weighting potential on edge pixels. (a): The relation between the normalized weighting potential and the normalized depth; (b): The relation between the normalized anode photopeak centroid and the normalized depth.

Since the decrease in the photopeak centroid from the anode side to the cathode side reflects the increase in the electron trapping due to longer drift distances, the smaller change in the photopeak centroid on peripheral pixels makes the electron trapping seem to be smaller than it actually is. If the exponential relation of the electron trapping (Equation 2.14) from the cathode to the anode side (excluding the region very close to the anode) is used to calculate the electron mobility-lifetime product [80] in a pixellated detector, the $(\mu\tau)_e$ will be overestimated for the peripheral pixels.

The imbalance in the weighting potential of the two coplanar grids in the peripheral region is a problem degrading the energy resolution of coplanar grid detectors [81, 82]. With the help of the 3-D position sensitivity, the non-uniformity in the weighting potential at the peripheral is mitigated to the scale of the position resolution.

7.4 Variation in $(mt)_e$ and Energy Resolution

The lateral distributions and statistical results of $(mt)_e$ are shown in Figure 6.13 and 6.14 for detector #2.2 and #2.3 respectively. Variations in $(mt)_e$ have been observed in both detectors.

Because the whole detector thickness is divided into ~40 C/A ratio indexes and the events occurring in the depth layer near the cathode is selected using C/A ratio for the $(mt)_e$ measurement, the uncertainty in the electron drift length could have 2.5% round-off error from discretization, resulting in up to 2.5% systematic error in the measured $(mt)_e$. However, the relative standard deviation from the different pixels is ~7%, significantly larger than the measurement error (up to 2.5%). Therefore, the variation in the measured $(mt)_e$ from different pixels is likely due to the non-uniform electron trapping in the lateral dimension. Even with single polarity charge sensing techniques and methods to compensate for electron trapping, such as relative gain and depth sensing, the variations in $(mt)_e$ will result in variations in electron trapping and thus a broadening of the photopeak for events occurring at the same depths but under pixels spread in the lateral direction. However, by doing 3-D correction of electron trapping, this variation can be mitigated down to the position resolution.

7.5 Summary

Variations in photopeak centroid, electron mobility-lifetime product, electron drift time, energy resolution, photopeak efficiency and total efficiency in 3-dimensions have been observed. Possible effects of various electron trapping defects, the variation in ionization energy, any surface defects, and the variation in weighting potential have been discussed. The 3-D detector response can be used to identify possible defects in the detector. The experimental results show that large lateral size electron trapping defects do not significantly degrade the energy resolution of the corresponding pixels, but small ones do. However, with 3-D position sensing, the events coming from the bad region can be discarded. It has also been discussed that the small-scale variation in the ionization energy, if any, should not exceed 0.5% FWHM for most pixels.

CHAPTER 8

SUMMARY AND FUTURE WORK

8.1 Modeling Results

The system modeling has covered three different topics. First, the energy deposition by gamma ray interactions in 3-D CdZnTe detectors was simulated using Geant4. The mean diameter of the initial electron cloud created by the energetic ionizing electron was found to be ~220 μm for 662 keV and increases rapidly with higher energies. It was shown that diffusion during drifting was also a non-negligible factor contributing to the size of the electron cloud arriving at the anode. Given the 1.27 mm pixel pitch, large fraction of charge sharing events is unavoidable especially at high gamma ray energies. For larger pixel pitch, the fraction of charge sharing events will decrease but the fraction of those events in which multiple interactions occur under the same pixel will increase. It is hard to tell whether smaller pixel pitch or larger pixel pitch is better for energy resolution. The simulation also suggested that a 20-30 keV anode-triggering threshold is necessary to correctly identify 90% of the multiple-pixel events. Second, the weighting potential of the anode pixel and the cathode was calculated using Maxwell. The cathode to anode signal ratio was then calculated as a function of the interaction depth, showing a linear relation between the C/A ratio and the true interaction depth. It has been recognized that the weighting potential cross-talk on neighboring pixels can be as high as 8% depending on the lateral position of the electron cloud. Therefore, a calibration of weighting potential cross-talk must be carried out in order to

correctly reconstruct multiple-pixel events. Third, the 75-ns-shaping-time fast shaper output of the timing channel was simulated using the Simulink toolbox of Matlab. Both the anode signal and the cathode signal have timing-amplitude-walk, which needs to be calibrated in order to use electron drift time depth sensing for multiple-pixel events. The timing resolution was found to be mainly limited by the cathode signal. A depth resolution of 0.36 mm FWHM could be achieved at 662 keV using electron drift time depth sensing.

8.2 Detector Systems

Two 3-D CdZnTe detectors were studied in this research, each consisting of an 11×11 pixellated anode and a single cathode on a $1.5 \times 1.5 \times 1.0$ cm^3 CdZnTe crystal fabricated by eV-PRODUCTS. The pixel pitch is 1.27 mm. There is a common grid between pixel anodes biased at negative voltage to focus the electrons to the pixel anodes. The trace width of the grid electrode is 100 µm with a 200 µm gap between the grid and the pixel. The CZT crystal is mounted on a ceramic plate. The conducting traces within the multi-layer ceramic plate connect every pixel anode to a corresponding metal pad on the periphery of the plate. A short wire-bond connects each pad on the ceramic plate to the input of each ASIC channel on the front-end board.

Three iterations of readout electronic system (ASIC, front-end board and controller board) have been developed, namely VAS2/TAT2, VAS3/TAT3 and VAS3.1/TAT3. The VAS2/TAT2 system had several serious problems. Firstly, due to improper wiring on the front-end board, the pickup noise on the cathode from digital clocks was too large causing retriggering and high threshold problems. It was believed that the common mode noise observed among most channels was also due to this cross-talk problem. Secondly, both the baseline and the gain were very sensitive to temperature

144

change, which could further degrade the energy resolution. Thirdly, there was significant non-linearity in the system response, limiting the achievable spectroscopic performance of multiple-pixel events. Despite all these difficulties, after intensive investigation, special hardware modifications and comprehensive calibration and events reconstruction algorithms were successfully implemented in the VAS2/TAT2 system. Promising results were obtained, especially for multiple-pixel events, reaffirming our confidence in the 3-D CdZnTe system. The VAS3/TAT3 system was developed by collaboration between Ideas ASA and our group to address the problems discovered in the VAS2/TAT2 system. Most of the goals were achieved, such as lower cross-talk noise, lower gain drift, higher dynamic range, better linearity and adjustable triggering threshold for each channel. However, due to a design fault of Ideas ASA, the shaper output of the ASIC was unstable and had strange ripple shape. As a consequence, the energy resolution was even worse than that of the VAS2/TAT2 system. The redesigned system, VAS3.1/TAT3, showed significant performance improvements over the previous two systems with all problems solved. Based upon the success of the VAS3.1/TAT3 system, we have begun to develop the 3-D CdZnTe array system.

8.3 Calibrations and Events Reconstruction

Because of the variations and non-uniformity in both the detector response and the electronics, various calibration procedures must be carried out to convert the raw output signals into energies and 3-D coordinates of gamma-ray interactions. The baseline of each channel needs to be detected and subtracted from the output signal. For the VAS2/TAT2 system, it is necessary to correct the common mode noise. Although greatly reduced, the gain-temperature variation still exists in the VAS3.1/TAT3 system and hence needs to be calibrated as in the VAS2/TAT2 system. Significant non-linearity was

observed in the VAS2/TAT2 system and calibration was done using multiple gamma-ray energies. The linearity of the VAS3.1/TAT3 system is good enough but the baseline offset still needs to be corrected using a simpler two-point calibration. In order to correct the photopeak broadening due to the non-uniform response among pixels and at different depths, the whole detector volume is conceptually divided into thousands of small voxels, each representing a small volume under a pixel and in a certain depth range. Gamma ray interaction events collected from a ^{137}Cs source is used as the calibration data. Every single-pixel event is binned into the corresponding subspectrum according to the pixel location and the interaction depth derived from the cathode to anode signal ratio. By finding out the photopeak centroid and applying a correction coefficient accordingly to each subspectrum, all subspectra can be aligned to form a total spectrum with a sharp photopeak.

The reconstruction of multiple-pixel events is not as straightforward as for single-pixel events. Because of the better depth resolution derived from the cathode to anode signal ratio, the depth correction coefficients obtained from the C/A ratio are still used in the depth correction for multiple-pixel events. However, the interaction depths for multiple-events have to be derived from the electron drift times. Therefore, a calibration is needed to convert the electron drift time to the corresponding C/A ratio. As shown in the system modeling, timing-amplitude-walk is quite significant in the timing signal and must be corrected to get the true electron drift time. Separate timing-amplitude-walk calibration methods are designed for the anode and the cathode timing signal and the results are in line with the modeling prediction. Although the cathode energy signal cannot be directly used to derive the interaction depths for multiple-pixel events, this residual information can be used to improve the depth information obtained from the electron drift time by comparing the calculated cathode signal to the measured cathode

146

signal. The last important calibration for multiple-pixel events is the weighting potential cross-talk. The correction coefficients for weighting potential cross-talk are calculated by grouping all two-pixel events into subspectra according to the distance between and the centroid depth of the two interactions and measuring the photopeak centroids of these subspectra.

8.4 Experimental Results

The experiments were performed on two $1.5 \times 1.5 \times 1.0$ cm^3 3-D CdZnTe detectors read out by the VAS2/TAT2 system and the VAS3.1/TAT3 system. The experiments included the energy resolutions for single-pixel events and multiple-pixel events, the analysis of factors degrading the energy resolution for multiple-pixel events, the spectrum for multiple gamma-ray energies, the spectrum for a uranium ore, the measurement of $(mt)_e$ and the analysis of factors affecting the detector response.

8.4.1 Spectroscopic performance

The electronic noise of the VAS2/TAT2 system was estimated to be ~6 keV. After all the calibrations discussed in Chapter 5, the energy resolution was measured to be 1.11% FWHM and 1.14% FWHM at 662 keV for single-pixel events, 1.57% FWHM and 1.64% FWHM at 662 keV for two-pixel events, and 2.13% FWHM and 2.28% FWHM at 662 keV for three-pixel events, for the two detectors respectively. The depth resolution of the C/A ratio method was estimated to be ~0.25 mm at 662 keV, while that of the electron drift time method was only ~0.8 mm due to poor timing resolution. Energy spectra from multiple gamma ray sources clearly demonstrated the spectroscopic ability and good energy resolution of the 3-D CdZnTe spectrometer.

Thanks to the improvements in the VAS3.1/TAT3 readout electronics, the electronic noise was reduced to less than ~4.5 keV. This resulted in a dramatic improvement in the energy resolution for single-pixel events. Unprecedented energy resolution values of 0.93% FWHM and 0.78% FWHM at 662 keV have been achieved for single-pixel events collected from the two detectors respectively, making an remarkable milestone of breaking the 1% resolution barrier. However, the resolutions for two-pixel events were worse than expected - 1.46% FWHM and 1.24% FWHM at 662 keV for the two detectors respectively. Analysis showed that charge sharing and non-linearity were unlikely to be the reason for energy resolution degradation of multiple-pixel events. The spectrum obtained from a sample of uranium ore demonstrated the ability of the 3-D CdZnTe spectrometer to do spectroscopy at high gamma ray energy up to a few MeV, with the reconstruction of multiple-pixel events. However, the problem of energy resolution degradation with increasing pixel number and increasing energy remaines to be solved.

8.4.2 Measurement of $(\mu\tau)_e$

By irradiating the cathode with an [241]Am source and collecting spectra from all anode pixels under two different cathode biases, the $(\mu\tau)_e$ value of the CdZnTe material underneath each anode pixel was individually estimated using the relation between the photopeak centroid and the cathode bias. Detector #2.2 has a measured mean $(\mu\tau)_e$ of ~3.22×10^{-3} cm^2/V with a standard deviation of ~0.22×10^{-3} cm^2/V. Detector #2.3 has a measured mean $(\mu\tau)_e$ of ~6.79×10^{-3} cm^2/V with a standard deviation of ~0.51×10^{-3} cm^2/V. Variations in the $(\mu\tau)_e$ from different pixels indicates the material non-uniformity in the lateral dimension across the detector, which can cause variations in the

148

collected electrons even for the same energy deposited at the same interaction depth but underneath different pixels. Only a 3-D correction can solve this problem.

8.4.3 Analysis of detector response

The detector response can be analyzed in three dimensions using 3-D position-sensitive CdZnTe spectrometers. Variation in photopeak centroid, electron mobility-lifetime product, electron drift time, energy resolution, photopeak efficiency and total efficiency in 3-dimensions have been observed. Possible effects of various electron trapping defects, the variation in ionization energy, any surface defects, and the variation in weighting potential have been discussed. The 3-D detector response can be used to identify possible defects in the detector. The experimental results show that large lateral size electron trapping defects do not significantly degrade the energy resolution of the corresponding pixels, but small ones do. However, with 3-D position sensing, the events coming from the bad region can be discarded. It has also been discussed that the small-scale variation in the ionization energy, if any, should not exceed 0.5% FWHM for most pixels.

8.5 Suggestions for Future Work

The 3-D position sensitive CdZnTe gamma ray spectrometer is fully functional at room temperature and has achieved excellent energy resolution for single-pixel events and significantly improved energy resolution for multiple-pixel events. More work is needed for it to be used in practical gamma ray spectroscopy.

The detectors used in this research were fabricated by eV-PRODUCTS three years ago and have the dimension of $1.5 \times 1.5 \times 1.0$ cm^3. Today, larger CdZnTe single crystals with better uniformity and higher $(\mu\tau)_e$ are available from both eV-PRODUCTS

and Yinnel Tech. Since large sensitive volume is always desired to promote gamma ray detection efficiency, it would be interesting to see how the system works with larger CdZnTe detectors, such as $2.0 \times 2.0 \times 1.5$ cm^3 detectors with 1.82 mm pixel pitch. In order to achieve even higher sensitivity, it is necessary to modularize the current 3-D CdZnTe system into standard compact package, which can be plugged into a motherboard to form a 3-D CdZnTe array system. Better spectroscopic performance can be expected due to the lower electronic noise and the lower triggering threshold in such a compact design. Extensive collaboration between Ideas ASA and our group has been deployed to design such an array system. The evolution from a single detector into an array system will be quite a challenging work.

The 3-D CdZnTe system has achieved excellent energy resolution for single-pixel events and significantly improved energy resolution for multiple-pixel events. But the resolutions for multiple-pixel events are still worse than expected. Charge sharing and non-linearity didn't seem to be the reason. Small charge leakage to neighboring pixels below the system low energy threshold might be a direction worth investigating. If two 3-D CdZnTe systems can be operated in coincidence mode, the coincident single-pixel events from both detectors may provide some clues to the energy resolution degradation in two-pixel events. Anyway, more effort needs to be devoted to find out the reasons for the energy resolution degradation of multiple-pixel events.

A comprehensive data acquisition, calibration and processing program has been developed for the 3-D CdZnTe system. Although the program can accomplish most of the calibrations and data processing automatically for detectors with very few bad pixels, manual adjustments and inputs are still necessary and painstaking for pixels with unexpected response. Improved algorithms for automatic calibration and better data visualization for easy diagnosis are necessary if the 3-D CdZnTe spectrometers are to be

operated by non-expert users. In addition, studies of temperature dependence and long term stability must also be carried out before 3-D CdZnTe spectrometers can be used in field gamma ray spectroscopy.

BIBLIOGRAPHY

1. Sangsingkeow, P., et al., *Advances in germanium detector technology.* Nuclear Instruments & Methods A, 2003. **505**: p. 183-186.

2. Heerden, P.J.V., *The Crystal Counter.* 1945, Utrcht Dissertation.

3. Price, W.J., *Nuclear Radiation Detection.* 2nd ed. 1964, New York: McGraw-Hill.

4. Willig, W.R., *Mercury iodide as a gamma spectrometer.* Nuclear Instruments & Methods, 1971. **96**(4): p. 615-616.

5. Willig, W.R., *Large bandgap mercury and lead compounds for nuclear particle detection.* Nuclear Instruments & Methods, 1972. **101**(1): p. 23-24.

6. Swierkowski, S.P., G.A. Armantrout, and R. Wichner, *High-resolution HgI$_2$ x-ray spectrometers.* Applied Physics Letters, 1973. **23**: p. 281-282.

7. Hull, K., et al., *Recent developments in thick mercuric iodide spectrometers.* IEEE Transactions on Nuclear Science, 1983. **30**: p. 402-404.

8. Knoll, G.F., *Radiation Detection and Measurement.* 3rd ed. 2000, New York: John Wiley & Sons, Inc.

9. Mohammed-Brahim, T., Friant, and J. Mellet, *Structure mis effects on polarization of HgI$_2$ crystals used for gamma-ray detection.* IEEE Transactions on Nuclear Science, 1985. **32**(1): p. 581.

10. Akutagawa, W., K. Zanio, and J.W. Mayer, *CdTe as a gamma detector.* Nuclear Instruments & Methods, 1967. **55**: p. 383-385.

11. Cuzin, M., *Some new developments in the field of high atomic number materials.* Nuclear Instruments & Methods in Physics Research A, 1987. **253**: p. 407-417.

12. Vavilov, V.S., et al., Sov. Atomic Energy, 1970. **28**: p. 641.

13. Cornet, A., et al., Applied Physics Letters, 1970. **17**: p. 432.

14. Siffert, P., et al., *Polarization in cadmium telluride nuclear radiation detectors.* IEEE Transactions on Nuclear Science, 1976. **23**(1): p. 159-170.

15. Bell, R.O., G. Entine, and H.B. Serreze, *Time-dependent polarization of CdTe gamma-ray detectors.* Nuclear Instruments & Methods in Physics Research, 1974. **117**: p. 267-271.

16. Butler, J.F., C.L. Lingren, and F.P. Doty, *Cd$_{1-x}$Zn$_x$Te gamma-ray detectors.* IEEE Transactions on Nuclear Science, 1992. **39**: p. 605-609.

17.   Toney, J.E., et al., *Uniformity of $Cd_{1-x}Zn_xTe$ grown by high-pressure bridgman.* Nuclear Instruments & Methods in Physics Research A, 1996. **380**: p. 132-135.

18.   Eisen, Y., *Current state-of-the art industrial and research application using room-temperature CdTe and CdZnTe solid state detectors.* Nuclear Instruments & Methods in Physics Research A, 1996. **380**: p. 431-439.

19.   Chibani, L., M. Hage-Ali, and P. Siffert, *Electrically active defects in detector-grade CdTe:Cl and CdZnTe materials grown by THM and HPBM.* Journal of Crystal Growth, 1996. **161**: p. 153-158.

20.   Olmos, P., G. Garcia-Belmonte, and J.M. Perez, *Large volume HgI_2 counters: a novel technique for pulse dicrimination.* Nuclear Instruments & Methods in Physics Research A, 1992. **322**: p. 557-561.

21.   Gerrish, V.M., D.J. Williams, and A.G. Beyerle, *Pulse filtering for thick mercuric iodide detectors.* IEEE Transactions on Nuclear Science, 1987. **34**: p. 85-90.

22.   Beyerle, A., V. Gerrish, and K. Hull, *Parallel pulse processing for mercuric iodide gamma-ray detectors.* Nuclear Instruments & Methods in Physics Research A, 1986. **242**: p. 443-449.

23.   Jones, L.T. and P.B. Woollam, *Resolution improvement in CdTe gamma detectors using pulse-shape discrimination.* Nuclear Instruments & Methods in Physics Research, 1975. **124**: p. 591-595.

24.   Frisch, O., *British Atomic Energy Report.* 1944.

25.   Luke, P.N., *Unipolar Charge Sensing with Coplanar Electrodes -- Application to Semiconductor Detectors.* IEEE Transactions on Nuclear Science, 1995. **42**(4): p. 207-213.

26.   Luke, P.N., *Single-polarity charge sensing in ionization detectors using coplanar electrodes.* Applied Physics Letters, 1994. **65**(22): p. 2884-2886.

27.   Barrett, H.H., J. D. Eskin, and H. B. Barber, *Charge Transport in Arrays of Semiconductor Gamma-Ray Detectors.* Physical Review Letters, 1995. **75**(1): p. 156-159.

28.   Marks, D.G., et al., *A 48x48 CdZnTe array with multiplexer readout.* IEEE Transactions on Nuclear Science, 1996. **43**(3): p. 1253-1259.

29.   Apotovsky, B., et al., *Semiconductor radiation detector with enhanced charge collection.* 1996: US Patent 5677539.

30. Barber, H.B., et al., *Progress in developing focal-plane-multiplexer readout for large CdZnTe arrays for nuclear medicine applications.* Nuclear Instruments & Methods in Physics Research A, 1996. **380**: p. 262-265.

31. Hage-Ali, M., et al., *Cadmium telluride small probes for gamma-ray spectrometry.* Nuclear Instruments & Methods in Physics Research A, 1996. **380**: p. 427-430.

32. McGregor, D.S., et al., *Geometrically weighted semiconductor Frisch grid radiation spectrometers.* Nuclear Instruments & Methods in Physics Research A, 1999. **422**: p. 164-168.

33. McGregor, D.S., et al., *CdZnTe semiconductor parallel strip Frisch grid radiation detectors.* IEEE Transactions on Nuclear Science, 1998. **45**(3): p. 443-449.

34. Lee, E.Y. and e. al., *Device simulation of a unipolar gamma-ray detector.* Proceedings of MRS, 1998. **487**(537).

35. Butler, J.F., *Novel electrode design for single-carrier charge collection in semiconductor nuclear radiation detectors.* Nuclear Instruments & Methods in Physics Research A, 1997. **396**: p. 427-430.

36. Montemont, G., et al., *A capacitive Frisch grid structure for CdZnTe detectors.* IEEE Transactions on Nuclear Science, 2001. **48**(3): p. 278-281.

37. He, Z., *Review of the Shockley-Ramo theorem and its application in semiconductor gamma-ray detectors.* Nuclear Instruments & Methods A, 2001. **463**(1-2): p. 250-267.

38. Shor, A., Y. Eisen, and I. Mardor, *Spectroscopy with pixelated CdZnTe gamma detectors - experiment versus theory.* Nuclear Instruments & Methods in Physics Research A, 2001. **458**: p. 47-54.

39. He, Z., et al., *1-D position sensitive single carrier semiconductor detectors.* Nuclear Instruments & Methods A, 1996. **380**(1-2): p. 228-231.

40. Li, W., et al., *Spatial Variation of Energy Resolution in 3-D Position Sensitive CZT Gamma-Ray Spectrometers.* IEEE Transactions on Nuclear Science, 1999. **46**(3): p. 187-192.

41. He, Z., et al., *Position-sensitive single carrier CdZnTe detectors.* Nuclear Instruments & Methods A, 1997. **388**(1-2): p. 180-185.

42. Loef, E.V.D.v., et al., *High-energy-resolution scintillator: Ce^{3+} activated $LaBr_3$.* Applied Physics Letters, 2001. **79**: p. 1573.

43.   Loef, E.V.D.v., et al., *Scintillation properties of LaBr3 :Ce3+ crystals: fast, efficient and high-energy-resolution scintillators.* Nuclear Instruments & Methods A, 2002. **486**: p. 254-258.

44.   Loef, E.V.D.v., et al., *High-energy-resolution scintillator:Ce^{3+} activated $LaCl_3$.* Applied Physics Letters, 2000. **77**: p. 1467.

45.   Guillot-Noel, O., et al., *Scintillation properties of $RbGd_2Br_7$:Ce advantages and limitations.* IEEE Transactions on Nuclear Science, 1999. **46**: p. 1274.

46.   Shah, K.S., et al. *High Energy Resolution Scintillation Spectrometers.* in *IEEE Nuclear Science Symposium and Medical Imaging Conference.* 2003. Portland, OR: IEEE.

47.   Shah, K.S., et al., *Scintillators for High Energy Resolution Gamma-Ray Spectroscopy.* 2003: Portland, OR.

48.   Bolotnikov, A. and B. Ramsey, *Improving the energy resolution of high-pressure Xe cylindrical ionization chambers.* IEEE Transactions on Nuclear Science, 1997. **44**(3): p. 1006-1010.

49.   Ottini-Hustache, S., et al., *HPXe ionization chambers for gamma ray spectrometry at room temperature.* Nuclear Instruments & Methods in Physics Research B, 2004. **213**: p. 279-283.

50.   Zhang, F., et al., *Improved Resolution for 3D Position Sensitive CdZnTe Spectrometers.* IEEE Transactions on Nuclear Science, 2004. **51**(5): p. 2427-2431.

51.   Zhang, F. and Z. He, *3D position sensitive CdZnTe gamma-ray spectrometers - improved performance with new ASICs.* Proceedings of SPIE, 2005.

52.   Li, W., *Three-Dimensional Position Sensitive CdZnTe Gamma Ray Spectrometers.* 2001, University of Michigan.

53.   Zhang, F., Z. He, and D. Xu, *Analysis of Detector Response using 3-D Position Sensitive CZT Gamma-Ray Spectrometers.* IEEE Transactions on Nuclear Science, 2004. **51**(6): p. 3295-3299.

54.   Lehner, C.E., Z. He, and G.F. Knoll, *Intelligent gamma-ray spectroscopy using 3-D position-sensitive detectors.* IEEE Transactions on Nuclear Science, 2003. **50**(4): p. 1090-1097.

55.   Du, Y.F., et al., *Evaluation of a Compton scattering camera using 3-D position sensitive CdZnTe detectors.* Nuclear Instruments & Methods A, 2001. **457**: p. 203-211.

56. He, Z., et al., *Hand-Held Gamma-Ray Imaging Sensors Using Room-Temperature 3-Dimensional Position-Sensitive Semiconductor Spectrometers.* AIP Conference Proceedings, 2002. **632**(1): p. 209-215.

57. Lehner, C.E., Z. He, and F. Zhang, *4p Compton Imaging Using a 3-D Position-Sensitive CdZnTe Detector via Weighted List-Mode Maximum Likelihood.* IEEE Transactions on Nuclear Science, to be published, 2004. **51**(4): p. 1618-1624.

58. Xu, D., et al., *4-pi Compton imaging with single 3D position sensitive CdZnTe detector.* Presented at SPIE in Denver, 2004.

59. Mayer, M., et al., *Signal formation in a CdZnTe imaging detector with coplanar pixel and control electrodes.* Nuclear Instruments & Methods A, 1999. **422**: p. 190-194.

60. McConnell, M.L., et al., *Three-dimensional imaging and detection efficiency performance of orthogonal coplanar CZT strip detectors.* Proceedings of SPIE, 2000. **4141**: p. 157-167.

61. Hamel, L.A. and e. al., *An imaging CdZnTe detector with coplanar orthogonal anode strips.* Proceedings of MRS, 1998. **487**: p. 211.

62. Luke, P.N., et al., *Coplanar grid CdZnTe detectors with three-dimensional position sensitivity.* Nuclear Instruments & Methods A, 2000. **439**: p. 611-618.

63. Li, W., et al., *A Data Acquisition and Processing System for 3-D Position Sensitive CZT Gamma-ray Spectrometers.* IEEE Transactions on Nuclear Science, 1999. **46**(6): p. 1989-1994.

64. CERN, *Geant4*. 2003: Geneva, Switzerland.

65. Ansoft_Inc.: 225 West Station Square Drive, Suite 200, Pittsburgh, PA 15219, USA.

66. The_MathWorks_Inc.: 3 Apple Hill Drive, Natick, MA 01760-2098, USA.

67. Ramo, S., *Currents induced by electron motion.* Proceedings of the I.R.E., September 1939: p. 584.

68. Shockley, W., *Currents to conductors induced by a moving point charge.* Journal of Applied Physics, 1938. **9**: p. 635-636.

69. Jen, C.K., *On the induced current and energy balance in electronics.* Proceedings of the I.R.E., June 1941: p. 345.

70. Cavalleri, G. and e. al., *Extension of Ramo's theorem as applied to induced charge in semiconductor detectors.* Nuclear Instruments & Methods, 1971. **92**: p. 137.

71. Li, W., et al., *A Modeling Method to Calibrate the Interaction Depth in 3-D Position Sensitive CdZnTe Gamma-Ray Spectrometers.* IEEE Transactions on Nuclear Science, 2000. **47**(3): p. 890-894.

72. Hecht, K., *Zum mechanismus des lichtelektrischen primarstromes in isolierenden kristallen.* Z. Phys., 1932. **77**: p. 235.

73. He, Z., G.F. Knoll, and D.K. Wehe, *Direct measurement of product of the electron mobility and mean free drift time of CdZnTe semiconductors using position sensitive single polarity charge sensing detectors.* Journal of Applied Physics, 1998. **84**(10): p. 5566-5569.

74. Agostinelli, S., et al., *Geant4 - a simulation toolkit.* Nuclear Instruments & Methods A, 2003. **506**: p. 250-303.

75. Ideas-ASA, *The Xa 1.6 docmentation v1.01.* 2003.

76. Amptek_Inc.: 6 De Angelo Drive, Bedford, Massachusetts 01730, USA.

77. National_Instruments_Corporation: 11500 North Mopac Expressway, Austin, Texas 78759, USA.

78. Ideas-ASA, *Docmentation for the VAS3.1 ASIC.* 2004.

79. Knoll, G.F., *Radiation Detection and Measurement, p.117.* 3rd ed. 2000, New York: John Wiley & Sons, Inc.

80. He, Z., et al., *Measurement of material uniformity using 3-D position sensitive CdZnTe gamma-ray spectrometers.* Nuclear Instruments & Methods A, 2000. **441**: p. 459-467.

81. Luke, P.N., et al., *Electrode Design for Coplanar-Grid Detectors.* IEEE Transactions on Nuclear Science, 1997. **44**(3): p. 713-720.

82. He, Z., et al., *Coplanar grid patterns and their effect on energy resolution of CdZnTe detectors.* Nuclear Instruments & Methods A, 1998. **411**(1): p. 107-113.